論文 / 著書情報
Article / Book Information

題目(和文)	フッ化物籠目格子反強磁性体における新奇基底状態
Title(English)	Unusual Ground State Observed in a Fluoride Family of Kagome Lattice Antiferromagnets
著者(和文)	片山和哉
Author(English)	Kazuya Katayama
出典(和文)	学位:博士(理学), 学位授与機関:東京工業大学, 報告番号:甲第10059号, 授与年月日:2016年3月26日, 学位の種別:課程博士, 審査員:田中 秀数,吉野 淳二,江間 健司,笹本 智弘,髭本 亘
Citation(English)	Degree:Doctor (Science), Conferring organization: Tokyo Institute of Technology, Report number:甲第10059号, Conferred date:2016/3/26, Degree Type:Course doctor, Examiner:,,,,
学位種別(和文)	博士論文
Type(English)	Doctoral Thesis

Unusual Ground State Observed in a Fluoride Family of Kagome Lattice Antiferromagnets

Kazuya Katayama

Department of Physics
Graduate School of Science and Engineering
Tokyo Institute of Technology

February, 2016

Abstract

From the viewpoint of geometrical frustration, the kagome lattice antiferromagnet (KLAF) is one of the most fascinating systems. It is theoretically known that small spin KLAFs show exotic quantum effects such as spin liquid ground state and magnetization plateaus caused by the interplay of frustration and quantum effects. Thus, the spin-1/2 KLAF is the frontier of quantum magnetism. However, the experimental studies on the spin-1/2 KLAFs have difficulty in capturing the essential magnetic properties because of the lattice disorder, impurities and difficulty in preparing single crystal. Spin-1/2 KLAFs $Rb_2Cu_3SnF_{12}$ and $Cs_2Cu_3SnF_{12}$ are almost free from these problems. $Cs_2Cu_3SnF_{12}$ has uniform kagome lattice at room temperature. $Cs_2Cu_3SnF_{12}$ undergoes a structural phase transition at $T_t = 185$ K and an antiferromagnetic long-range order at $T_N = 20$ K. The magnetic ordering is described by the $q = 0$ spin structure. $Rb_2Cu_3SnF_{12}$ has a $2a \times 2a$ enlarged chemical unit cell, which leads to four kinds of nearest-neighbor exchange interaction. The magnetic ground state of $Rb_2Cu_3SnF_{12}$ a singlet with an excitation gap.

In this thesis, I investigated the variation of the exchange parameters and the ground state in $(Rb_{1-x}Cs_x)_2Cu_3SnF_{12}$, using single crystals. The analysis of magnetic susceptibilities shows that with increasing the cesium concentration x, the exchange parameters increase with the tendency to be uniform. It was found that the ground state is disordered for $x < 0.53$ and ordered for $x > 0.53$. Néel temperature for $x > 0.53$ approach zero at $x_c \simeq 0.53$. This indicates that quantum phase transition from the disordered state to the ordered state occurs at x_c. These results were also confirmed by μSR measurements for $x_c = 0.53$. In the disordered state for $x < x_c$, the magnetic susceptibility is finite, nevertheless the long-range magnetic ordering is absent. This nature is characteristic of the valence-bond-glass (VBG) state, which was recently predicted as a ground state for exchange-disordered frus-

trated quantum antiferromagnets. The VBG state is an unusual ground state, in which spins form singlets randomly not only with the nearest-neighbor spins but also with the second-, third-neighbors and farther spins due to exchange randomness. This work gives the clear evidence of the VBG state in the KLAFs.

I also report the results of magnetization, specific heat and neutron powder diffraction measurements on spin-2 KLAF $Cs_2LiMn_3F_{12}$. The three-dimensional magnetic ordering was observed at $T_N \simeq 2.0$ K. The low-temperature specific heat is proportional to T^2, which indicates that $Cs_2LiMn_3F_{12}$ has a good two-dimensionality. From neutron powder diffraction, it was found that the spin structure in the ordered phase is characterized by a propagation vector $\boldsymbol{q} = (1/3, 0, 0)$. This unusual magnetic ordering that is neither $q = 0$ structure nor $\sqrt{3} \times \sqrt{3}$ structure is the first observation in KLAFs.

Contents

1 Introduction **5**

1.1 Quantum Effects 6

1.2 Geometrical Frustration and Kagome Lattice Antiferromagnets . . . 8

1.2.1 Geometrical Frustration 8

1.2.2 Kagome Lattice Antiferromagnets 10

1.3 Previous Studies of Fluoride Kagome Family 25

1.3.1 $Cs_2Cu_3SnF_{12}$ and $Rb_2Cu_3SnF_{12}$ 25

1.3.2 $Cs_2LiMn_3F_{12}$ 32

1.3.3 Motivation and Outline of This Study 35

2 Experimental Detail **37**

2.1 Sample Preparation 37

2.1.1 $A_2Cu_3SnF_{12}$ (A = Rb, Cs) 37

2.1.2 $Cs_2LiMn_3F_{12}$ 40

2.2 Magnetization measurement 40

2.3 Heat Capacity Measurement 42

2.4 Neutron Scattering Measurement 45

2.4.1 Elastic Neutron Diffraction 45

2.5 Muon Spin Relaxation 48

3 Quantum Phase Transition in $(Rb_{1-x}Cs_x)_2Cu_3SnF_{12}$ **51**

3.1 Magnetic and Thermodynamic Properties 51

3.1.1 Systematic Change in Exchange Parameters 51

3.1.2 Quantum Phase Transition 58

3.2 μSR Measurement on Sample with $x_c = 0.53$ 63

3.3 Discussion 69

4 Magnetic Properties of $Cs_2LiMn_3F_{12}$ **72**

4.1 Magnetic and Thermodynamic Properties 72

4.1.1 Specific Heat 73

4.1.2 Magnetic Susceptibility and Magnetization 74

4.2 Neutron Diffraction 80

5 Conclusion and Outlook **83**

Acknowledgement **87**

Reference **88**

Chapter 1

Introduction

Generally, ubiquitous magnetic properties in conventional magnets are well described by spin vector model. The model is given by

$$\mathcal{H} = \sum_{i,\ j} J_{ij} \boldsymbol{S}_i \cdot \boldsymbol{S}_j, \tag{1.1}$$

where the spins are labelled as i and j, and the sum runs over all of the nearest neighbor pairs $i,\ j$. The simple model has been revealed a variety of physical properties, for instance, magnetic susceptibilities of ferromagnetic or antiferromagnetic order and spin-wave excitations, and the list goes on and on.

Recently, it has been recognized that the quantum effect plays a significant role for magnetic ground states and excitations in low-dimensional quantum magnets. It is known that the one- and two-dimensional antiferromagnets that are expressed by XY and Heisenberg models preclude a magnetic order with breaking translational symmetry at finite temperature.

Besides, geometrically frustrated antiferromagnets have attracted growing attention owing to the potential realization of exotic ground states. One of the simplest and the most intriguing frustrated magnets is a Heisenberg antiferromagnet on the kagome lattice (KLAF), which is composed of corner-sharing triangles. For small spins, theoretical studies revealed that a synergetic effect of frustration and quantum fluctuation can lead to a disordered ground state, while for large spins, the system undergoes a magnetic order. Motivated by these fascinating theoretical predictions, many model compounds of KLAF have recently been synthesized and their magnetic properties have been actively investigated. These experimental studies also

stimulated new theoretical studies. In this thesis, I report a promising fluoride family of new model compounds of KLAF.

1.1 Quantum Effects

The Hamiltonian of the Heisenberg model is expressed as

$$\mathcal{H} = J\sum_{i,j} \boldsymbol{S}_i \cdot \boldsymbol{S}_j = J\sum_{i,j} \left\{ \frac{1}{2}\left(S_i^+ S_j^- + S_i^- S_j^+\right) + S_i^z S_j^z \right\} \tag{1.2}$$

where $\boldsymbol{S}_i$ is a spin operator on each site i, and $S_i^{\pm} = S_i^x \pm iS_i^y$. For a ferromagnetic linear chain with negative J, the ground state is given as

$$\cdots\uparrow\uparrow\uparrow\uparrow\uparrow\uparrow\uparrow\uparrow\uparrow\uparrow\cdots, \tag{1.3}$$

while for the antiferromagnetic chain with positive J, the Néel ordered state expressed as

$$\cdots\uparrow\downarrow\uparrow\downarrow\uparrow\downarrow\uparrow\downarrow\uparrow\downarrow\cdots, \tag{1.4}$$

is not the ground state, because this state has off-diagonal matrix elements for $\mathcal{H}$, and thus, this is not an eigenstate. The off-diagonal elements give rise to quantum fluctuation. Although the off-diagonal elements are smaller than the diagonal elements, in some cases, especially in frustrated magnets of interest in this thesis, the spin systems are enormously affected by the off-diagonal elements, so that the ground state becomes disordered. In large spin case, the effect of quantum fluctuation can be treated as the zero-point oscillation by a semi-classical spin-wave theory, which describes the antiferromagnet as an ensemble of harmonic oscillators.

Using the Néel ordered states, or spin-vector model, the energy of the ground state is expressed as

$$E_{\mathrm{N}} = -\frac{1}{2}zNJS^2, \tag{1.5}$$

where z and N are the number of the nearest neighbors and sites, respectively. The result is consistent with a molecular field theory. According to Bogolubov inequality,

the energy obtained by the molecular field theory is the upper limit of the lowest free energy [1]. The energy of the ground state using a spin-wave theory is described as [2–5]

$$E_{\mathrm{G}} = E_{\mathrm{cl}} + E_0 + \sum_l \sum_{\boldsymbol{\mu}} \hbar\omega_l(\boldsymbol{\mu}) \left\{ \alpha_l^\dagger(\boldsymbol{\mu})\alpha_l(\boldsymbol{\mu}) + \frac{1}{2} \right\}, \tag{1.6}$$

where E_{cl} is the classical energy, E_0 is the energy of quantum correction that is independent of spin states, l classifies the sublattices, and $\alpha_l^\dagger(\boldsymbol{\mu})$ and $\alpha_l(\boldsymbol{\mu})$ are creation and annihelation operators of magnons with momentum $\boldsymbol{\mu}$, respectively. $(1/2)\hbar\omega_l(\boldsymbol{\mu})$ in the third term is considered as the zero-point energy, which arises from the quantum fluctuation. For a uniform chain, two-dimensional square lattice and three-dimensional simple cubic lattice, the energy is expressed as

$$E_{\mathrm{G}} = -zNJS^2 \left[1 + \frac{1}{S} \left(1 - \frac{2}{N} \sum_{\boldsymbol{\mu}} \sqrt{1 - \gamma_{\boldsymbol{\mu}}^2} \right) \right], \tag{1.7}$$

where $\gamma_{\boldsymbol{\mu}} = \frac{1}{D} \sum_{i=1}^{D} \cos(\mu_i a)$, D is the dimensionality of the lattice. Thus, the energy is evaluated as $-zNJS(S+1) < E_{\mathrm{G}} < -zNJS^2$. Besides, the magnetic moment of a sublattice is shrunk by the quantum fluctuation. The magnetic moment of each sublattice is given by,

$$\langle S_{z,\mathrm{tot}} \rangle = \frac{NS}{2} \left[1 - \frac{1}{2S} \left(\frac{2}{N} \sum_{\boldsymbol{\mu}} \frac{1}{\sqrt{1 - \gamma_{\boldsymbol{\mu}}}} - 1 \right) \right]. \tag{1.8}$$

The second term comes from the quantum fluctuation. In the case of one-dimensional systems ($D = 1$), the second term diverges. This means that the quantum fluctuation is so significant to destroy the magnetic ordering. It was demonstrated that the ground state in low-dimensional antiferromagnets can be disordered and the magnetic moment becomes zero [2, 6–8].

1.2 Geometrical Frustration and Kagome Lattice Antiferromagnets

1.2.1 Geometrical Frustration

Geometrically frustrated quantum antiferromagnets, a research frontier in condensed matter physics, have been in the spotlight because of the potential realization of exotic ground states such as the spin-liquid state [9–13]. In this section, I explain a geometrically frustrated effect using the simplest model, which stems from the relative configuration of spins.

Figure 1.1(a) depicts the concept of frustration. Spins are situated on the corners of a single triangle connected by antiferromagnetic interactions of the same strength. For spins coupled by Ising Hamiltonian on a single triangle lattice, there is no spin configuration that satisfies the requirement of all the exchange bonds. In this case, the spins cannot be classified into two sublattices, which is refered to as a non bipartite lattice.

For classical spins coupled by Heisneberg Hemiltonian on a triangle lattice, the energy of the spins can be expressed as,

$$E = \frac{J}{2}(\boldsymbol{S}_1 + \boldsymbol{S}_2 + \boldsymbol{S}_3)^2 + \text{const}, \tag{1.9}$$

where the spins on three corners are labelled as $\boldsymbol{S}_1$, $\boldsymbol{S}_2$, $\boldsymbol{S}_3$. The energy is optimized by 120° spin structures, as shown in Fig. 1.1(b), instead of Néel spin structures. A new degree of freedom called a chirality is generated in this system. The vector chirality for a single triangle is defined as,

$$\boldsymbol{\kappa} = \frac{2}{3\sqrt{3}}(\boldsymbol{S}_1 \times \boldsymbol{S}_2 + \boldsymbol{S}_2 \times \boldsymbol{S}_3 + \boldsymbol{S}_3 \times \boldsymbol{S}_1). \tag{1.10}$$

For a coplanar arrangement of spins, the vector $\boldsymbol{\kappa}$ is normal to the spin plane with the amplitude of $+1$ or -1, which indicates anticlockwise and clockwise spin rotations along the side of the triangle.

Typical geometrically frustrated lattices are triangular and kagome lattices, as illustrated in Fig. 1.1(c) and (d), respectively. Since the first attractive hypothesis by Anderson in 1973 on resonating-valence-bond (RVB) ground state in the triangular lattice [14], the frustrated quantum magnets have been the center of attention in

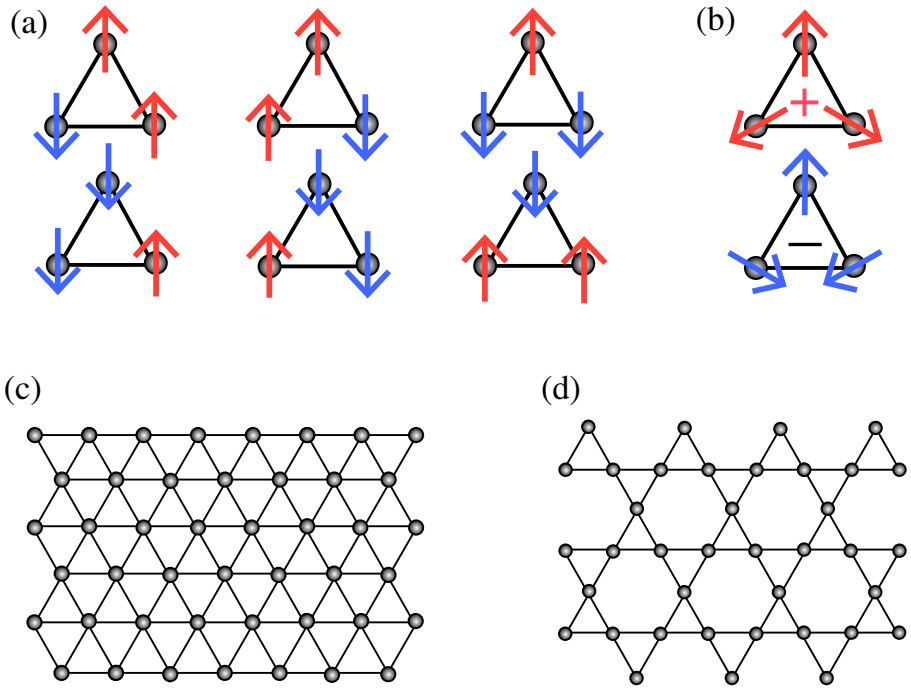

Figure 1.1: Illustration of frustration and frustrated lattices. (a) Ising spins coupled via antiferromagnetic exchange interaction on a triangle. Any spin configurations cannot be optimized with respect to Ising Hamiltonian. (b) XY or Heisenberg spins coupled via antiferromagnetic exchange interaction on a triangle. + and − indicate a vector chirality κ with the amplitude of $+1$ or -1. (c) Triangular lattice and (d) kagome lattice, which are typical geometrically frustrated lattices.

the field of the condensed matter physics. In the case of the vector spins on the triangular lattice, the ground state should be 120° spin structure, as mentioned above. Although from the Marshall-Lieb-Mattis theorem, it is uncertain whether the system undergoes a magnetic order, the spin-wave theory for $S = 1/2$ [15–17] demonstrates that the quantum fluctuation is insufficient to destroy the magnetic order with 120° spin structure, so that the sublattice has a finite magnetic moment. Recently, a numerical study shows that the ordered moment is estimated to be $\langle S \rangle = 0.205$ [18].

1.2.2 Kagome Lattice Antiferromagnets

One of the simplest and the most intriguing frustrated magnets is a Heisenberg antiferromagnet on the kagome lattice (KLAF) composed of corner-sharing triangles [19–22]. Kagome means a woven pattern of bamboo-basket, which Japanese people are using even now.

Theoretical Background

Order By Disorder

For the classical Heisenberg KLAF with the nearest-neighbor exchange interaction J, the ground state is infinitely degenerate owing to the local flexibility of the configuration of the 120° spin structure characteristic of the kagome lattice, as illustrated in Fig. 1.2. Since the degeneracy arises from an accidental degeneracy that is not related to the global symmetries, respective spin configurations differ in the energies of low lying excitations and quantum fluctuation. In the classical case, a specific state with the softest fluctuations tends to be mostly selected by the thermal fluctuations, because the Boltzmann factor of the state is the largest in all the spin configurations [23, 24]. This ordering mechanism is called *thermal order-by-disorder*, as shown in Fig. 1.3(a) [12]. The spin ordering owing to the order by disorder mechanism can be induced by the quantum fluctuation, in other words zero-point motion. The energy of the ground state in quantum antiferromagnets is given by Eq. (1.6) and the zero-point energy depends on the classical spin configuration. Therefore, the degeneracy can be lifted by the quantum fluctuation, as illustrated in Fig. 1.3(b) [10, 12, 25–28]. Consequently, A specific state with the lowest quantum fluctuation energy $E_{\rm qf}$ is selected as the ground state. This ordering mechanism is called *quantum order-by-disorder*.

Zero Energy Mode

In the case of a nonclassical Heisenberg model with a large spin-quantum number, it was predicted that the KLAF favors coplanar spin configurations [29] and the so-called $\sqrt{3} \times \sqrt{3}$ structure is stabilized by the quantum order-by-disorder mechanism on the basis of the spin-wave analysis [30–33]. Figures 1.4(a) and (b) show typical

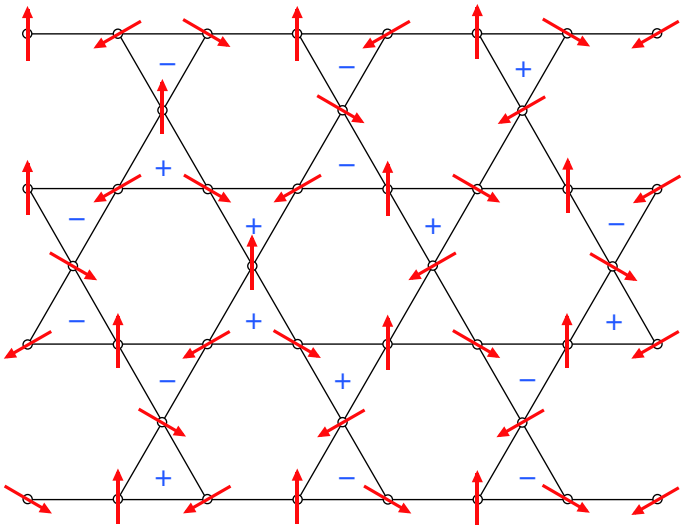

Figure 1.2: Illustration of the infinitely degenerate classical kagome lattice antiferromagnet with the nearest-neighbor coupling J. Notation "+" and "−" denote the chirality. Three spins on any triangle form the 120° spin structure. However, the arrangement of the chirality cannot be determined uniquely.

ground states of Heisenberg KLAF. The magnetic unit cell of $q = 0$ structure is the same as the chemical unit cell, whereas for $\sqrt{3} \times \sqrt{3}$ structure, the magnetic unit cell is enlarged to $\sqrt{3} \times \sqrt{3}$ with respect to the chemical unit cell. Non-planar states can be generated by continuous local rotation of a planar state without any energy cost [30, 31, 34], as illustrated in Figs. 1.4(c) and (d). This local excitation is called zero-energy mode. When there exists the easy-plane anisotropy or the Dzyaloshinskii-Moriya interaction of the form $\boldsymbol{D}_{i,j} \cdot [\boldsymbol{S}_i \times \boldsymbol{S}_j]$ with the $\boldsymbol{D}$ vector perpendicular to the lattice plane, the local excitation costs finite energy, so that the zero-energy mode is lifted [35].

Ground State in Quantum Kagome Lattice Antiferromagnet

The most intriguing case is spin-1/2 case, where a noteworthy synergistic effect of the geometric frustration, the local flexibility and the quantum fluctuation is expected. In this case, the accuracy of the spin-wave analysis should be deteriorating owing to enormous quantum effects. A long-standing theoretical debate

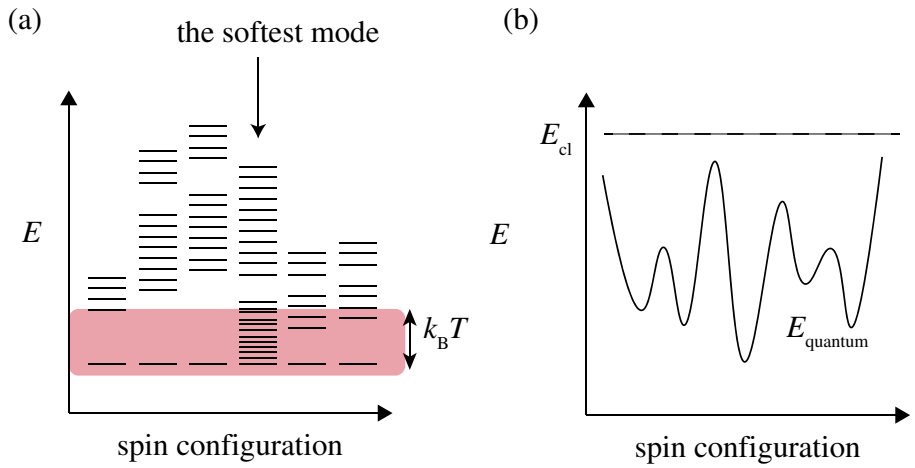

Figure 1.3: Schematic figure of energy level of KLAF with Heisenberg model. (a) Energy levels of excited states. Since a state with the softest mode has the largest Boltzmann factor, the state is stabilized in finite temperature T. (b) Energy level of ground state determined by quantum fluctuation. The dashed line represents the energy of classical ground state (E_{cl}), which is infinitely degenerate. Degeneracy within the classical energy can be lifted by the quantum fluctuation. A specific state with the lowest quantum-fluctuation energy ($E_{\rm qf}$) is stabilized.

has reached a consensus that the quantum-disordered state is more stable than any ordered state. However, the nature of the ground state has not been theoretically elucidated. Recent theory proposed nonmagnetic ground states, such as the valence-bond-solid (VBS) [36–40] and quantum spin-liquid states including resonating valence-bond (RVB) state [41–43], which are described by a static array of singlet dimers and the linear superposition of various configurations composed of singlet dimers, respectively, as illustrated in Figs. 1.5(a) and (b).

The nature of low-energy excitations also remains unsolved. The presence of a gap for the triplet excitation is still controversial [44, 45, 51–53]. Exact diagonarization calculations revealed that the singlet-triplet excitation gap exists, which is filled with continuous excitations with singlet states. This low-lying singlet excitations are attributable to the spin-liquid state and/or RVB state [44]. Density matrix renormalization group (DMRG) method supports the singlet-triplet gap [45, 52]. Meanwhile, projective wave function method indicates that the ground state has no magnetic order and finite susceptibility, which is characteristic of the spinon-Fermi

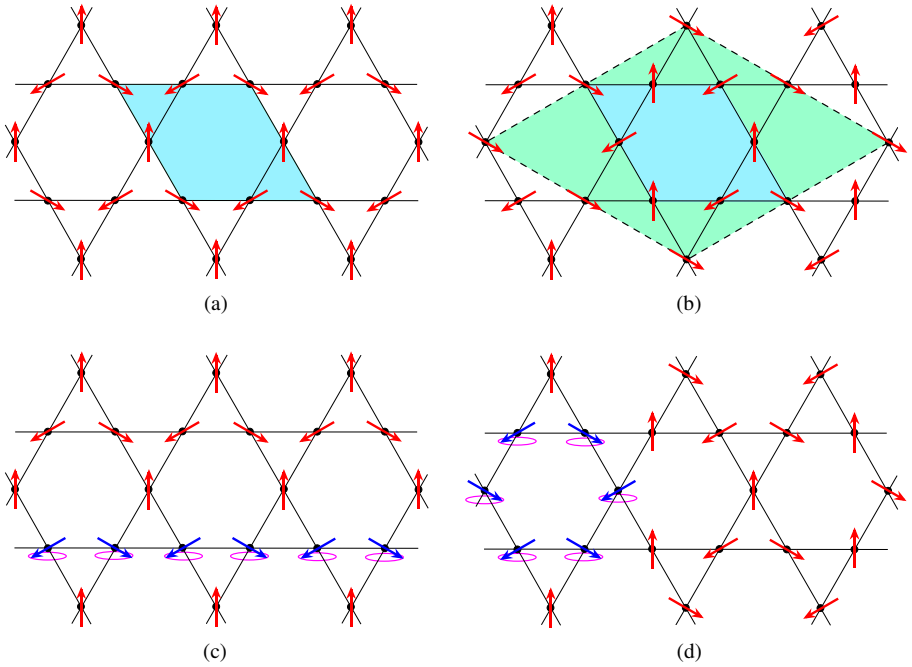

Figure 1.4: Typical ground states in the classical Heisenberg KLAFs. (a) $\boldsymbol{q} = 0$ structure, where the magnetic unit cell corresponds with the chemical one. (b) $\sqrt{3} \times \sqrt{3}$ spin structure, where the magnetic unit cell is enlarged to $\sqrt{3}a \times \sqrt{3}a$. (c) and (d) are illustrations of continuous local rotation of spins for $\boldsymbol{q} = 0$ and $\sqrt{3} \times \sqrt{3}$ structures, respectively, without any energy cost.

surface.

Effect of the Dzyaloshinskii-Moriya Interaction

In reality, owing to the lack of inversion symmetry at the middle point of neighboring lattice points in kagome lattice, an antisymmetric interaction of Dzyaloshinskii-Moriya (DM) type [46, 47] is inevitable. Dzyaloshinskii pointed out that in some crystal, an antisymmetric interaction can appear, which results in the weak ferromagnetic moment [46]. Moriya derived the antisymmetric interaction from a microscopic model [47]. The DM interaction is expressed by the vector product of

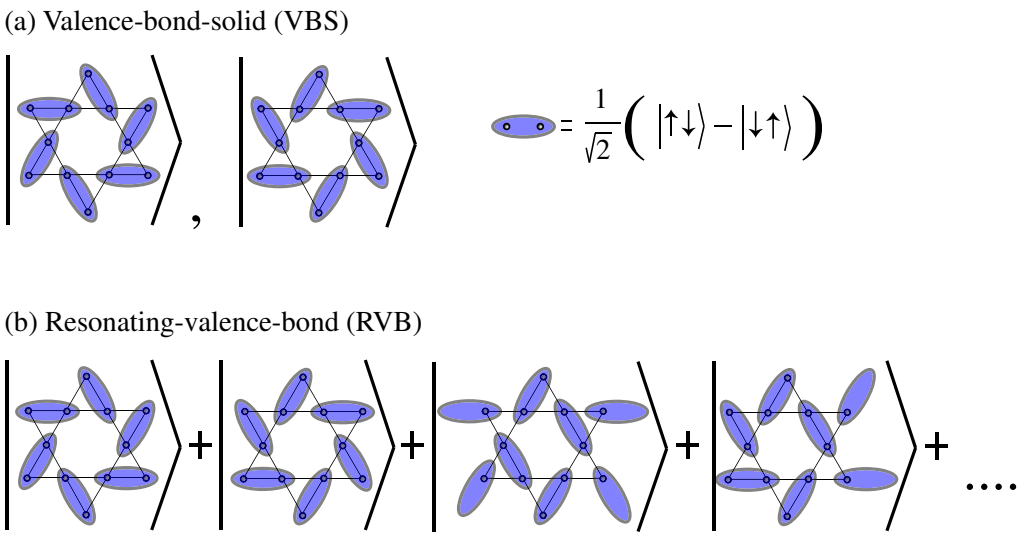

Figure 1.5: Predicted ground states of spin-1/2 quantum Heisenberg KLAF. (a) Valence-bond-solid (VBS) state, given by a static arrangement of spin-singlet state, which is two fold degenerate. (b) Resonating-valence-bond (RVB) state described by the linear superposition of various configurations composed of singlet dimers, where translational symmetry is not broken.

spins as

$$\mathcal{H}_{\rm DM} = \sum_{i,j} \boldsymbol{D}_{i,j} \cdot [\boldsymbol{S}_i \times \boldsymbol{S}_j] \,. \tag{1.11}$$

DM interaction greatly affects the ground state of KLAF to reduce the quantum fluctuation [48–50, 61]. Because the DM interaction mixes the singlet and triplet states, which have opposite parity with respect to permutation of the spins, the total spin is no longer a good quantum number. Therefore, the ground state has finite $S = 1$ components, which leads to non zero susceptibility.

A remarkable effect of the DM interaction in an $S = 1/2$ Heisenberg KLAF is that this interaction destroys the disordered ground state [50]. Using exact diagonalization, it was demonstrated that with increasing the z component $D^{\parallel}$ of the $\boldsymbol{D}$ vectors, which are arranged as shown in Fig. 1.6(a), the disordered ground state becomes unstable and quantum phase transition from a disordered state to an ordered state with the $\boldsymbol{q} = 0$ spin configuration takes place at $D^{\parallel} = 0.1J$ [50]. This is because the DM interaction with the $\boldsymbol{D}$ vectors arranged as shown in Fig. 1.6(a)

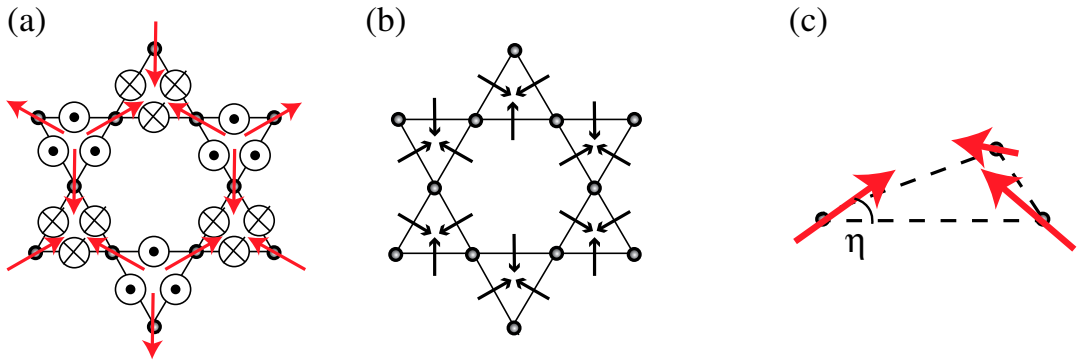

Figure 1.6: (a) and (b) Arrangements of the z ($D^{\parallel}$) and in-plane ($D^{\perp}$) components of the $\boldsymbol{D}$ vectors of Dzyaloshinskii-Moriya interaction in KLAF with mirror planes passing through each of the center between adjacent sites, respectively. The red and black arrows indicate spins and DM vectors of the in-plane components, respectively. The circled dots and circled crosses in (a) and the arrows in (b) represent the local positive directions of the parallel and perpendicular components $D^{\parallel}$ and $D^{\perp}$, respectively. $D^{\parallel}$ stabilizes the $\boldsymbol{q} = 0$ spin structure represented by red arrows. (c) Configuration of canted spins. η indicate the canted angle.

prefers the $\boldsymbol{q} = 0$ spin structure represented by red arrows. Moreover, the in-plane component $D^{\perp}$ of the $\boldsymbol{D}$ vectors (Fig. 1.6(b)) produces a canting of ordered moment, as shown in Fig. 1.6(c) [48]. The canted angle η is given by

$$\tan 2\eta = \frac{2D^{\perp}}{\sqrt{3}J + D^{\parallel}}. \tag{1.12}$$

Magnetization Process in Quantum KLAF

The magnetic properties of quantum KLAFs described above is the case of zero magnetic field. Remarkable quantum nature is observed in the magnetization process of quantum Heisenberg KLAFs. The magnetization process of a classical antiferromagnet is monotonical up to saturation, e.g., the magnetization is proportional to the applied magnetic fields and saturates. For a quantum triangular lattice antiferromagnet, successive phase transitions induced by quantum fluctuation occur in magnetic fields. A notable feature is that the *up-up-down* spin state is stabi-

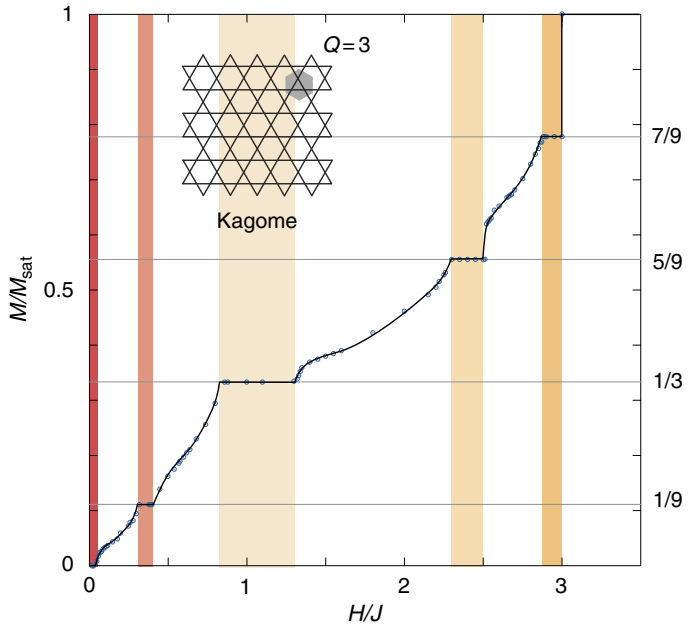

Figure 1.7: Magnetization as function of magnetic field in $S=1/2$ kagome lattice Heisenberg antiferromagnet [53].

lized in a finite field range, which leads to a magnetization plateau at one third of the saturation value [62–65]. The 1/3-magnetization plateau induced by the quantum order-by-disorder mechanism was also predicted theoretically. Various numerical studies confirmed that one-third magnetization plateau occurs for $S = 1/2$ Heisenberg KLAF [53, 66–69]. Surprisingly, it was demonstrated that the magnetization of $S=1/2$ Heisenberg KLAF is quantized at $m=0$ and $m=(2n-1)/9$ with $n=1,2,\cdots$, as shown in Fig. 1.7 [53, 54].

Effect of Exchange Randomness: Valence-Bond-Glass

In realistic materials of frustrated quantum magnets such as $ZnCu_3(OH)_6Cl_2$ with a spin-liquid-like ground state as shown below, there exists certain amount of lattice or charge disorder, which leads to exchange randomness. Motivated by this situation of realistic materials, the effect of exchange randomness on KLAF was

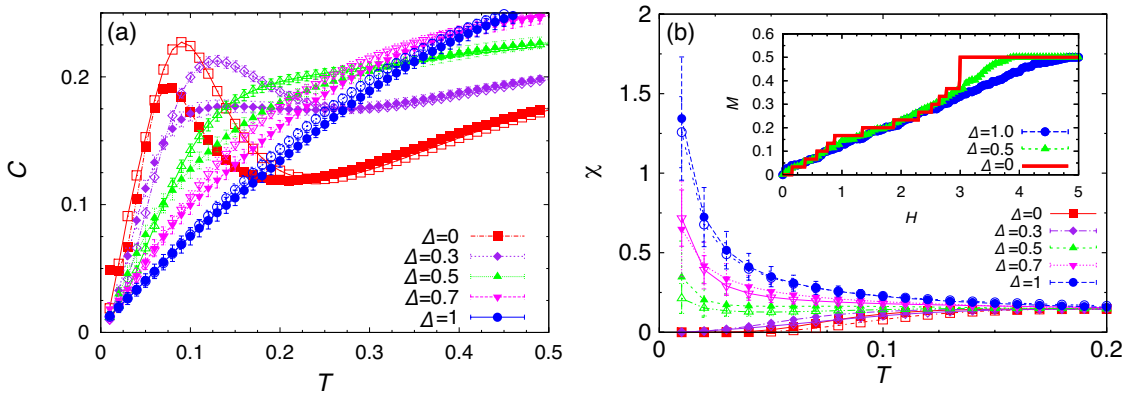

Figure 1.8: Temperature dependence of (a) specific heat and (b) magnetic susceptibility on the randomness parameter Δ [57]. The inset of (b) shows the Δ dependence of magnetization.

investigated theoretically [55–58]. It was demonstrated that a spin-liquid-like state called "random singlet" [59, 60] or "valence-bond-glass" [55, 70] is induced by the exchange randomness.

Kawamura and his coworkers [56–58] investigated $S = 1/2$ triangular and kagome lattice Heisenberg antiferromagnets with the random antiferromagnetic exchange bond J_{ij}, which is described as

$$\mathcal{H} = \sum_{i,j} J_{ij} \boldsymbol{S}_i \cdot \boldsymbol{S}_j, \tag{1.13}$$

where J_{ij} obeys the uniform distribution between $(1-\Delta)J$ and $(1+\Delta)J$ with the mean J. The parameter Δ is a index of randomness. $\Delta = 0$ corresponds to the uniform latiice, and $\Delta = 1$ is the most random case. They calculated the sublattice magnetization, thermodynamic properties and dynamical structure factor, using exact diagonalization for up to 30-site clusters [57, 58].

It was revealed that when the randomness parameter Δ exceeds a critical value of $\Delta_c \sim 0.4$, a disordered ground state changes to a gapless spin-liquid-like state. For the specific heat, the broad peak at $T = 0.1$ K characteristic of the uniform kagome lattice is suppressed with increasing Δ. Finally, specific heat shows a linear temperature dependence of T at low temperatures, as shown in Fig. 1.8(a). The low-temperature susceptibility for $\Delta = 0$ is almost zero. However, with increasing

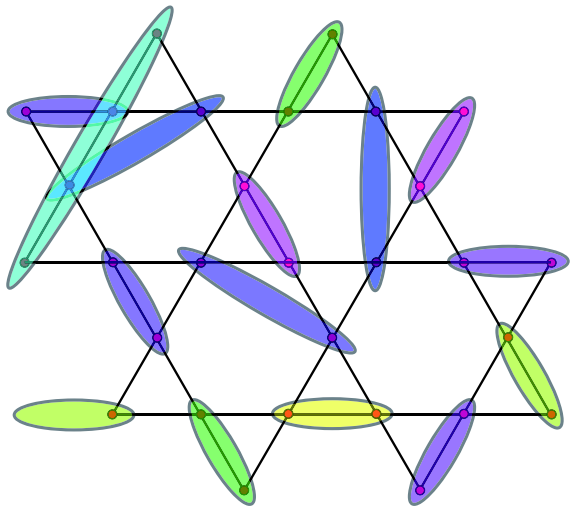

Figure 1.9: Illustration of a valence bond glass state. A ellipse represents a singlet bond, whose color corresponds to the strength of the bonds

Δ, the low-temperature susceptibility increases, as shown in Fig. 1.8(b). The 1/3-magnetization-plateau is smeared with increasing Δ. These results indicate that the ground state is gapless without magnetic ordering. They also show that dynamical structure factor has no sharp singularity due to characteristic excitations. These ground state properties are consistent with those observed in of $ZnCu_3(OH)_6Cl_2$ shown below. Another research group suggests that the ground state has a pseudo gap when the pure system has a gaped ground state [70].

A naive concept of the VBG state is such that tightly bound spin singlets are situated at stronger J_{ij} bonds, while loosely bound singlets at weaker J_{ij} bonds, as shown in Fig. 1.9 [55]. Because there are many loosely bound singlets, where the singlet-triplet excitations are gapless, the magnetic susceptibility becomes finite. Shimokawa *et al.* [58] argued that in the case of un-frustrated lattice, for instance square lattice with random antiferromagnetic bonds, the system does not exhibit the random singlets-state. Their results indicate that the frustration plays a significant role in the ground state when randomness is introduced.

Experimentally, there are some candidates for the VBG state in triangular lattice antiferromagnets such as $Cs_2Cu(Br_{1-x}Cl_x)_4$ [71, 72]. In $Cs_2Cu(Br_{1-x}Cl_x)_4$, The Néel temperature decreases drastically with increasing chlorine concentration x and

magnetic ordering is absent for $x > x_c = 0.17$. For $x > x_c$, low-temperature specific heat is linear in temperature, as predicted by theory [56]. However, for KLAFs there is no clear evidence of the VBG state.

Previous Experimental Studies on Some KLAFs

On the experimental side, considerable effort has been exerted to search for materials that closely approximate the $S = 1/2$ Heisenberg KLAF. The candidates include potassium iron jarosite $KFe_3(OH)_6(SO)_4$ [73], volborthite $Cu_3V_2O_7(OH)_2{\cdot}2H_2O$ [74], and herbertsmithite $ZnCu_3(OH)_6Cl_2$ [75]. However, the materials investigated, many of which are natural minerals, have individual problems such as spatial anisotropy of the exchange network [76, 77], exchange disorder due to ion substitution [78] and lattice distortion due to a structural phase transition [79]. For these reasons, there has been little clear experimental evidence demonstrating the nature of the ground state and the excitations for the $S = 1/2$ Heisenberg KLAF. I briefly review some experimental results on these systems.

(1) Potassium Iron Jarosite: $KFe_3(OH)_6(SO)_4$

In $KFe_3(OH)_6(SO)_4$, magnetic ions Fe^{3+} with spin $S = 5/2$ form uniform kagome lattice [73]. The antiferromagnetic ordering occurs at $T_N = 65$ K (see Fig. 1.10(a) and (b)), and from neutron diffraction experiments [80, 81], its ground state was found to be $\boldsymbol{q} = 0$ spin structure as depicted in Fig. 1.4(a). The exchange interaction J was estimated to be $J/k_B = 42$ K.

It is noted that the potassium iron jarosite is the first report on observing the rather flat mode, or zero-energy mode as shown in Fig. 1.10(c), which is characteristic of KLAFs, while the non-dispersive branch is shifted to approximately 8 meV due to the presence of the anisotropy interaction, say the DM interaction [35, 82]. A stepwise anomaly was observed in the high-field magnetization curves, which is caused by the spin reorientation, as shown in Fig. 1.10(d) [83, 84]. The results of dispersion relations, high-field magnetization measurements and ESR spectra of jarosite can be explained in terms of the DM interaction models [35, 82, 84].

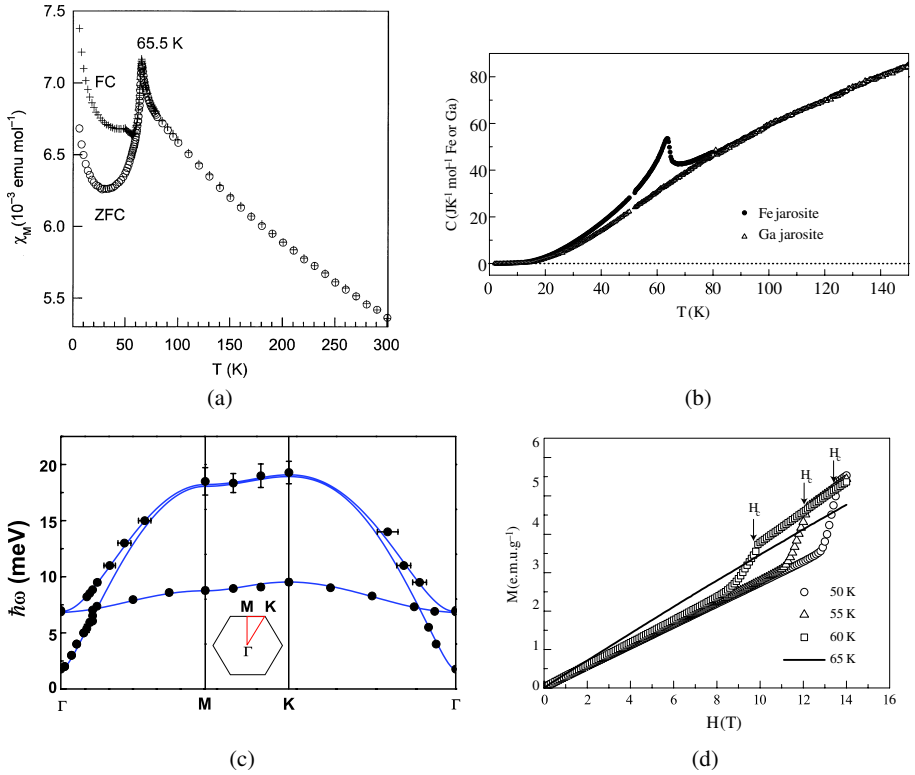

Figure 1.10: Physical properties of potassium iron jarosite, $KFe_3(OH)_6(SO)_4$. (a) Temperature dependence of magnetic susceptibilities measured at $H = 50$ Oe under zero field cool (ZFC) and field cool (FC) [81]. (b) Temperature dependences of specific heats for $KFe_3(OH)_6(SO)_4$ and nonmagnetic $KGa_3(OH)_6(SO)_4$ [83]. (c) Dispersion relation along the high-symmetry point measured at $T = 10$ K [82]. Blue solid lines indicate fits with the DM model. (d) Magnetization curves measured at several temperature for $H \parallel c$ [83].

(2) Volborthite: $Cu_3V_2O_7(OH)_2{\cdot}2H_2O$

The first report of synthesis of $S = 1/2$ KLAF was made on volborthite [74]. Magnetic ions Cu^{2+} with spin $S = 1/2$ of volborthite form a quasi-kagome lattice. Volborthite undergoes the antiferromagnetic ordering at $T = 2$ K, as shown in Fig. 1.11(a) and (b) [85, 86]. Quite recently, single crystals were synthesized using hydrothermal synthesis method [76]. Using the polycristalline and single-crystal samples, one-third magnetization plateau characteristic of Heisenberg KLAF was

observed in the wide magnetic field range, as shown in Fig. 1.11(c) [76,86–88]. However, the results of thermodynamic measurements obtained by single crystals are significantly different from those by the crystalline one. Besides, the exchange network is different from that of the uniform kagome lattice, the crystal structure is still disputed [76, 89], and the nearest-neighbor interaction turned out to be ferromagnetic [77]. Thus, a consensus on the spatially isotropic Hamiltonian in volborthite has yet to be reached.

(3) Herbertsmithite: $ZnCu_3(OH)_6Cl_2$

Herbertsmithite is named after a British mineralogist, G. F. Herbert Smith, who first discovered a mineral of paratacamite, $Zn_xCu_{4-x}(OH)_6Cl_2$. Herbertsmithite, a polymorph of kapellasite, is a doped member of the paratacamite family where one-quarter of the sites of a pyrochlore-like lattice are occupied by diamagnetic Zn^{2+}, and the remaining sites are occupied by Cu^{2+} with spin $S = 1/2$. Cu^{2+} ions to form a uniform kagome network; some say herbertsmithite forms a perfect kagome lattice [75]. From magnetic measurements, the Weiss temperature and nearest-neighbor exchange interaction were obtained as $\Theta_W = -314$ K and $J/k_B = 200$ K, respectively [75, 90]. It was reported that there is no magnetic order down to 30 mK and the non-dispersion excitation were observed shown in Fig. 1.12. NMR measurements revealed that the local magnetic susceptibility at lowest temperature has a finite value. These results are characteristics of a gapless spin-liquid state [78, 90–93].

However, there still exist controversial arguments about the ground state and the exited state. Some theories suggest that the gapless excitation is attributable to the so-called spinon-Fermi surface, while the nature of the gapless ground state is induced by Cu/Zn anti-site disorders, as mentioned above [94]. For experimental sides, because 15% of nonmagnetic Zn^{2+} sites, which are located between kagome layers, are occupied by magnetic Cu^{2+} ions [95, 96], the local structure resembles the end member clinoatacamite, $Cu_2(OH)_3Cl$. The Jahn-Teller active Cu^{2+} ions substituted for Zn^{2+} ions will disturb the perfect kagome lattice of herbertsmithite. The local magnetic impurities make it difficult to unveil the intrinsic low energy properties [95, 97]. Furthermore, quite recently, NMR measurements and inelastic

neutron diffraction revealed that the ground state has the singlet-triplet excitation gap [98, 99]. However, the nature of the ground state remains unsolved to date.

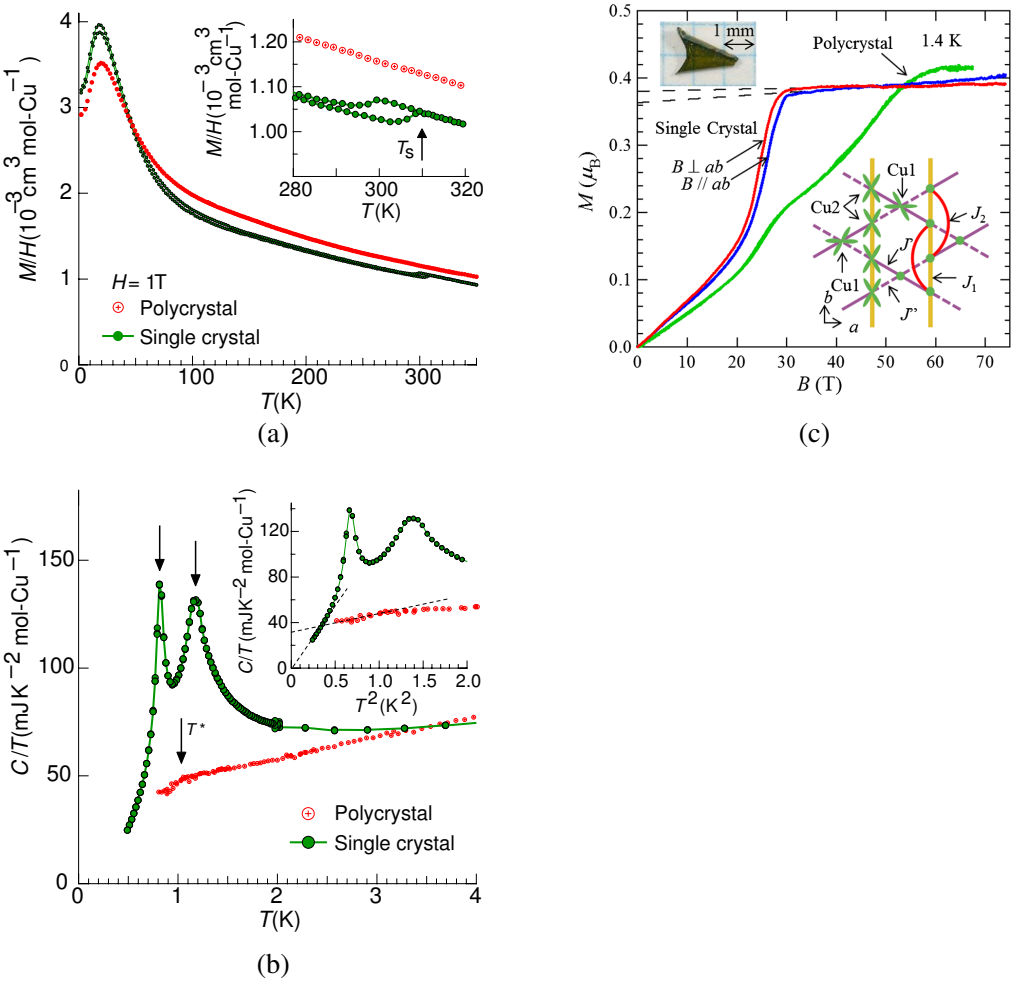

Figure 1.11: Physical properties of volborthite, $Cu_3V_2O_7(OH)_2{\cdot}2H_2O$. (a) Temperature dependence of magnetic susceptibilities measured at $H = 1$ T upon cooling and heating [76]. (b) Temperature dependence of specific heat divided by temperature [76]. Green and red circle represent single crystal and polycrystalline sample in (a) and (b), respectively. (c) Magnetization curves measured at 1.4 K on single crystals in magnetic fields perpendicular (red line) and parallel (blue line) to the *ab* plane, and on a polycrystalline sample (green line) [88].

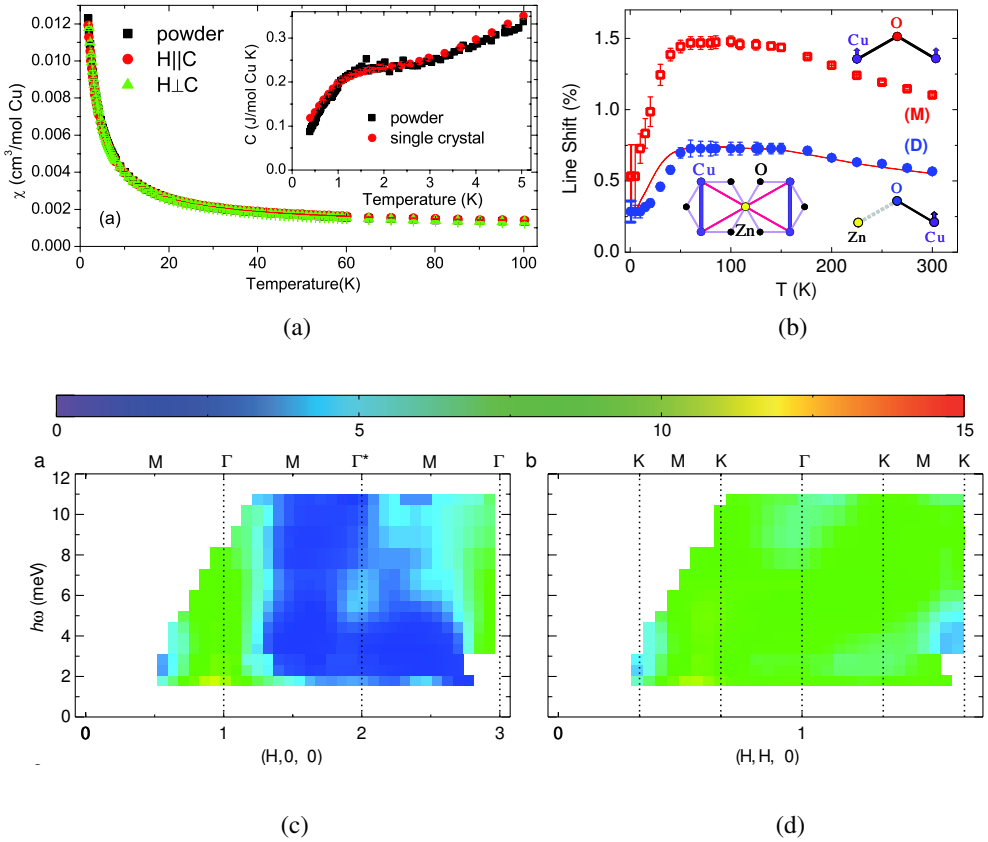

Figure 1.12: Physical properties of herbertsmithite, $ZnCu_3(OH)_6Cl_2$. (a) Temperature dependence of bulk magnetic susceptibilities of single crystal and powder sample [90]. Inset shows specific heat of single crystal and powder sample in the absence of applied fields. (b) Temperature dependence of NMR line shift [97]. (c) Dispersion relation along the high symmetry direction of $(H, 0, 0)$ and $(H, H, 0)$ measured at $T = 1.6$ K [92].

1.3 Previous Studies of Fluoride Kagome Family

1.3.1 $Cs_2Cu_3SnF_{12}$ and $Rb_2Cu_3SnF_{12}$

Crystal Structure of $Cs_2Cu_3SnF_{12}$ and $Rb_2Cu_3SnF_{12}$

The cupric fluoride kagome family $A_2Cu_3SnF_{12}$ (A = Rb and Cs), which has a rhombohedral structure, is a promising subject of comprehensive study on spin-1/2 KLAFs [100, 101]. I summarized the atomic coordinates and site symmetries of $Cs_2Cu_3SnF_{12}$ and $Rb_2Cu_3SnF_{12}$ in Table 1.1 and 1.2, respectively. Figures 1.13 and 1.14 show the crystal structures of $Cs_2Cu_3SnF_{12}$ and $Rb_2Cu_3SnF_{12}$ viewed along the [110]-axis and c axis. CuF_6 octahedra are linked by sharing their corners in the crystallographic ab plane. Magnetic Cu^{2+} ions with spin-1/2 form a kagome lattice in the ab plane. The octahedra are elongated along the principal axis owing to the Jahn-Teller effect, whose axis is approximately parallel to the c axis. Hence, the hole orbitals $d(x^2 - y^2)$ of Cu^{2+} lie in the kagome layer. This leads to a strong superexchange interaction in the kagome layer and a negligible superexchange interaction between the kagome layers.

At room temperature, $Rb_2Cu_3SnF_{12}$ has a $2a \times 2a$ enlarged chemical unit cell in the ab plane, as shown in Fig. 1.14(b); thus, the kagome lattice in $Rb_2Cu_3SnF_{12}$ is not uniform [100]. There are four sorts of nearest-neighbor exchange interactions as depicted in Fig. 1.15 [100]. $Cs_2Cu_3SnF_{12}$ has a uniform kagome lattice at room temperature [101], which is the same as that of $Cs_2Cu_3ZrF_{12}$ [102]. As the temperature decreases, $Cs_2Cu_3SnF_{12}$ undergoes a structural phase transition from the rhombohedral structure to a monoclinic structure at $T_t = 184$ K [103], which is closely related to the rhombohedral structure with a $2a \times 2a$ enlarged unit cell [101, 104].

Table 1.1: Atomic coordinates and site symmetries of $Cs_2Cu_3SnF_{12}$ whose space group has $R\overline{3}m$ (No. 166). Site symmetry in Hermann-Mauguin notation represents the crystal symmetry at the point where the atoms exist. Adapted from Ref. [101]

Atom	Site Symmetry	x	y	z
Cs	3 m	0.0	0.0	0.1060
Cu	. $2/m$	0.5	0.0	0.0
Sn	$-3m$	0.0	0.0	0.5
F(1)	. m	0.2042	-0.2042	0.9845
F(2)	. m	0.1312	-0.1312	0.4465

Table 1.2: Atomic coordinates ($\times 10^4$) and site symmetries of $Rb_2Cu_3SnF_{12}$ with space group $R\overline{3}$ (No. 148). Site symmetry in Hermann-Mauguin notation represents the crystal symmetry at the point where the atoms exist. Adapted from Ref. [100]

Atom	Site Symmetry	x	y	z
Rb(1)	3 .	6667	3333	-647
Rb(2)	1	3358	1650	641
Cu(1)	1	5946	1665	1682
Cu(2)	1	3516	-723	1769
Sn(1)	-1	5000	0	0
Sn(2)	-3 .	6667	3333	3333
F(1)	1	6495	651	1700
F(2)	1	7409	2773	1439
F(3)	1	4581	693	2105
F(4)	1	7853	4443	2780
F(5)	1	4464	872	-460
F(6A)	1	4501	310	835
F(7A)	1	6389	1378	95
F(6B)	1	3861	-250	629
F(7B)	1	6066	1320	470
F(8)	1	2465	-2156	1462

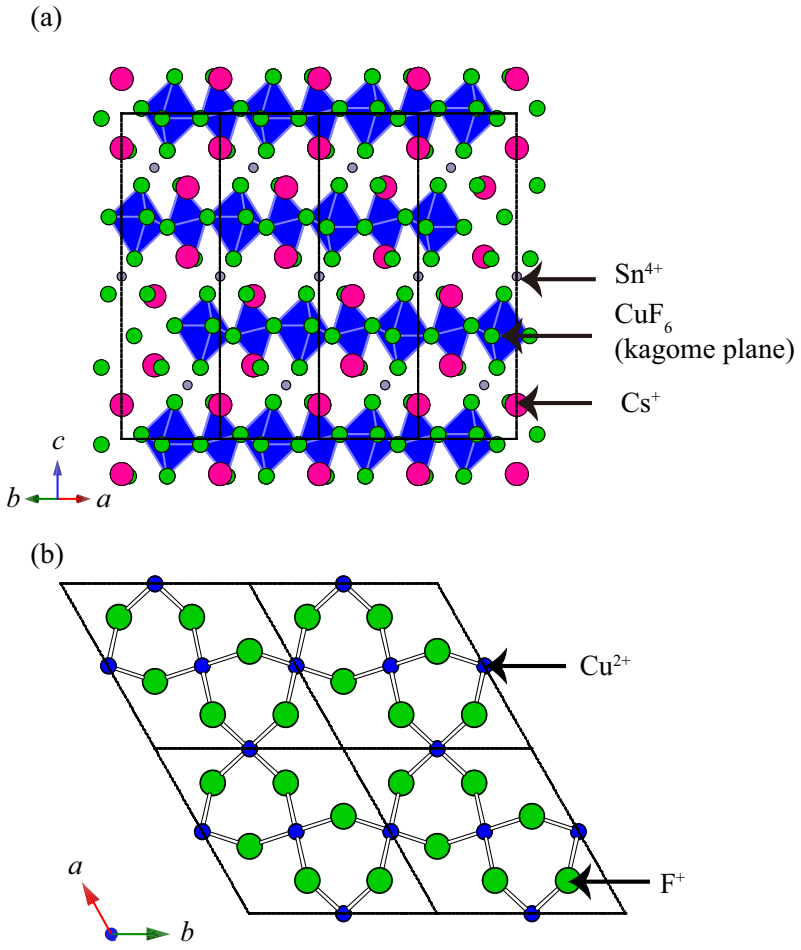

Figure 1.13: Crystal structure of $Cs_2Cu_3SnF_{12}$. (a) View along the [110]-axis. Octahedra colored blue represent CuF_6. The positions of the Cu^{2+} ions are located at the center of the octahedra. (b) View along c-axis, where F^- ions out of kagome-plane are deleted. Dotted lines denote the chemical unit cells.

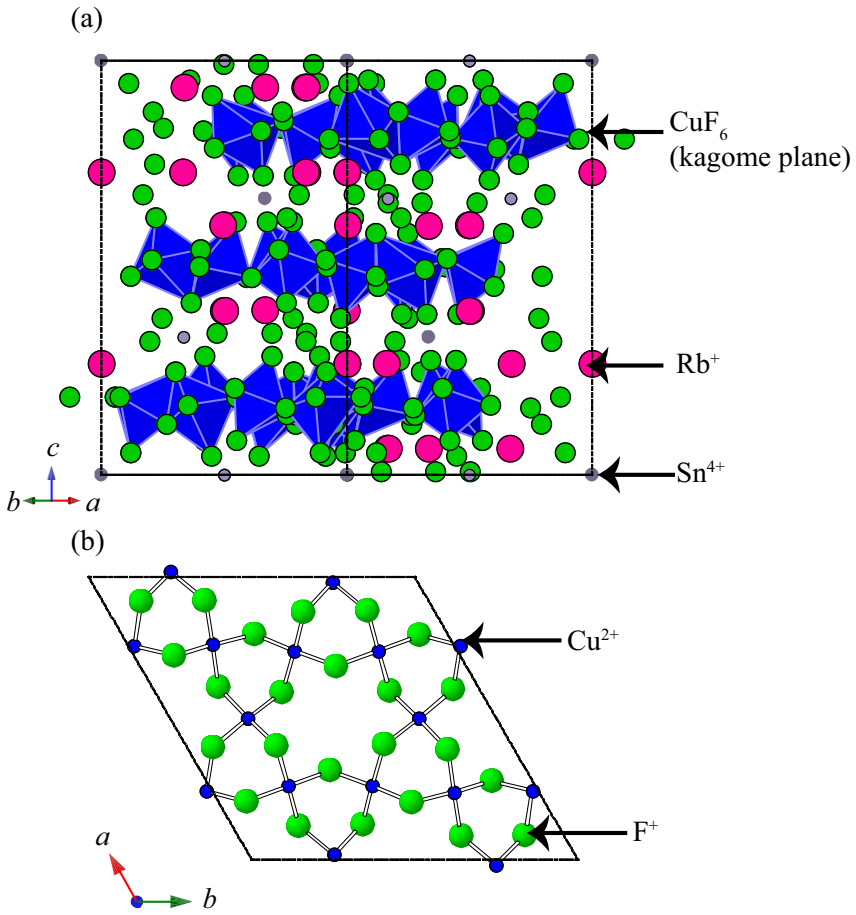

Figure 1.14: Crystal structure of $Rb_2Cu_3SnF_{12}$. (a) View along the [110]-axis. Octahedra colored blue represent CuF_6. The positions of the Cu^{2+} ions are located at the center of the octahedra. (b) View along c-axis, where F^- ions out of kagome-plane are deleted. Dotted lines denote the chemical unit cells.

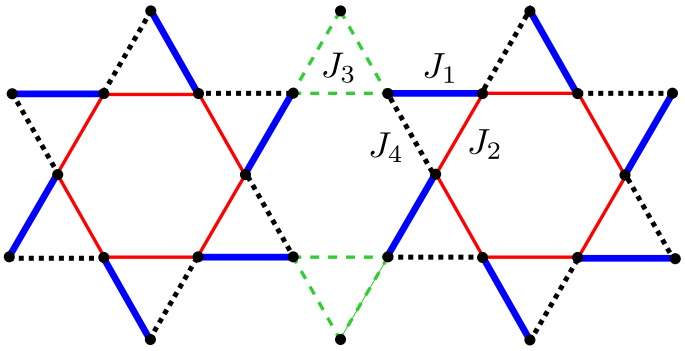

Figure 1.15: Exchange interactions J_i $(i = 1 - 4)$ for $Rb_2Cu_3SnF_{12}$.

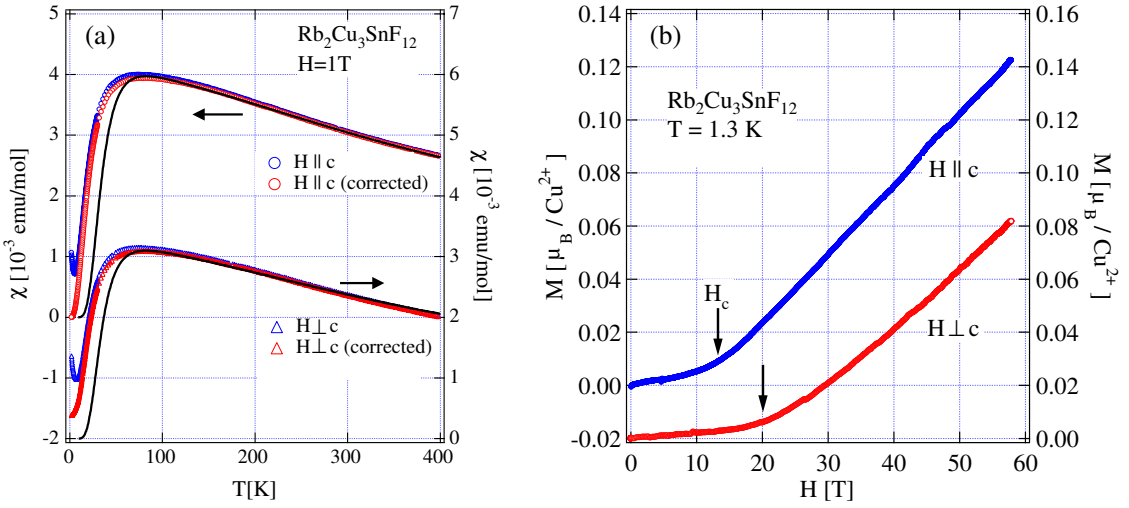

Figure 1.16: (a) Temperature dependence of the magnetic susceptibility of $Rb_2Cu_3SnF_{12}$ [100]. (b) Magnetization curves for $Rb_2Cu_3SnF_{12}$ measured at $T = 1.3$ K [100]. The arrows point the critical fields H_c.

Magnetic Properties of $Cs_2Cu_3SnF_{12}$ and $Rb_2Cu_3SnF_{12}$

Since high-purity and sizable single crystals are obtainable, the magnetic properties of these two compounds have been probed in detail by magnetic, neutron scattering and NMR measurements [104–106, 108].

Figure 1.16(a) shows temperature dependence of the magnetic susceptibility in $Rb_2Cu_3SnF_{12}$. With decreasing temperature, the susceptibility exhibits a broad maximum around 70 K and approaches exponentially toward zero, which is indicative of a spin-gapped ground state. As can be seen in Fig. 1.16(b), the magnetization is almost zero up to the critical fields $H_c \simeq 13$ T for $H \parallel c$ and 20 T for $H \perp c$, and increases rapidly.

The magnetic ground state of $Rb_2Cu_3SnF_{12}$ is a singlet state with an singlet-triplet excitation gap Δ/k_B of 27 K [100, 105, 106, 108]. The magnetic excitations in $Rb_2Cu_3SnF_{12}$ were investigated using inelastic neutron scattering [105,106]. Dispersion relations obtained are shown in Fig. 1.17. From the analysis of the dispersion relations, it was found that the ground state is the pinwheel valence-bond-solid (VBS) state, in which singlet dimers are situated on the strongest exchange interac-

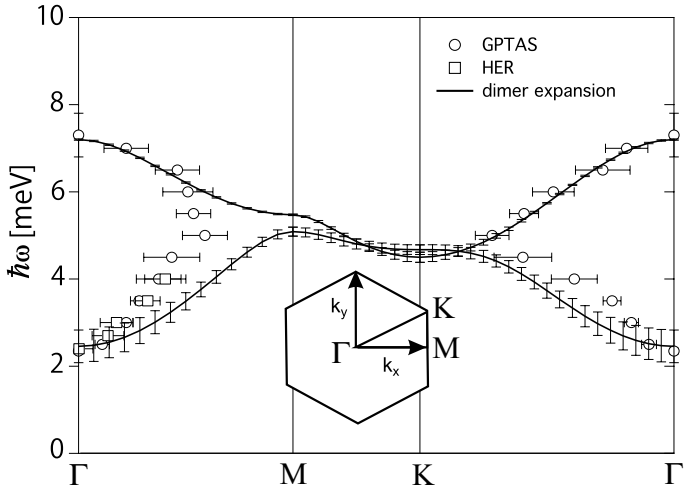

Figure 1.17: Dispersion relations of singlet-triplet excitations in $Rb_2Cu_3SnF_{12}$ measured at $T = 1.3$ K [105].

tion J_1 shown in Fig. 1.15 [105,106,109,110]. The upper and the lower branches are $S^z = 0$ and $S^z = \pm 1$ excitations. The splitting of these branches is attributed to the large DM interaction. Individual exchange constant and the magnitude of the DM interaction were obtained as $J_1/k_B = 216$ K, $J_2 = 0.95J_1$, $J_3 = 0.85J_1$, $J_4 = 0.55J_1$ and $D^z/J_1 = 0.18$. The gapped ground state in $Rb_2Cu_3SnF_{12}$ arises from the inequivalence of the exchange interactions.

On the other hand, $Cs_2Cu_3SnF_{12}$ exhibits a magnetic ordering at $T_N = 20.0$ K, as shown in Fig. 1.18(a) [101]. In the ordered phase, the so-called $q = 0$ spin structure is realized [104]. The configuration of the $\boldsymbol{D}$ vectors of the DM interaction in $Cs_2Cu_3SnF_{12}$ is shown in Fig. 1.6, which is approximately the same as that discussed by Cépas *et al.* [50]. As previously mentioned, Cépas *et al.* demonstrated that with increasing longitudinal component $D^{\parallel}$, the disordered state changes at $(D^{\parallel}/J)_c \approx 0.1$ to the ordered state with the $q = 0$ structure. The magnitude of the $\boldsymbol{D}$ vector in $Cs_2Cu_3SnF_{12}$ was evaluated to be $D^{\parallel}/J \simeq 1/4$ from the analyses of the dispersion relations shown in Fig. 1.18(b) [104]. Thus, the magnetic ordering observed in $Cs_2Cu_3SnF_{12}$ can be attributed to the large DM interaction.

Although the ground state of $Cs_2Cu_3SnF_{12}$ is ordered, a noteworthy quantum many-body effect on the spin-wave excitations was observed [104]. The excitation

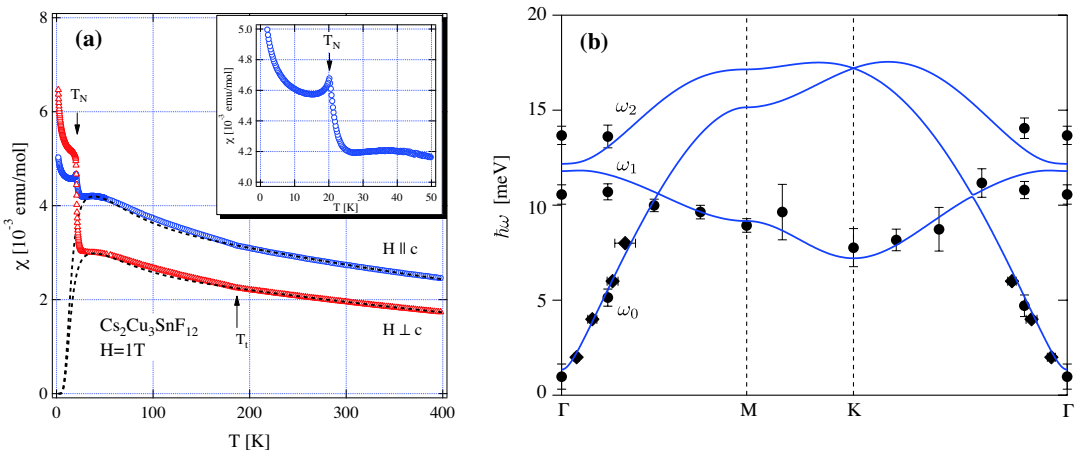

Figure 1.18: (a) Temperature dependence of the magnetic susceptibility of $Cs_2Cu_3SnF_{12}$. Arrows at 184 K and at 20 K indicate the structure and magnetic phase transition, respectively. Inset is a magnified view of the low temperature region below 50 K [101]. (b) The dispersion relations of the spin-wave excitations in $Cs_2Cu_3SnF_{12}$ [104, 107], which are expressed with respect to the unit cell at room temperature.

energies observed in $Cs_2Cu_3SnF_{12}$ are markedly renormalized downward as much as 40% with respect to the linear spin-wave result. In contrast, the excitation energies in the conventional quantum renormalization are renormalized upward [111–115].

1.3.2 $Cs_2LiMn_3F_{12}$

$Cs_2LiMn_3F_{12}$ crystallizes in a rhombohedral structure, $R\overline{3}$ [116], which is closely related to the structure of $Cs_2Cu_3ZrF_{12}$ [102]. Figure 1.19 shows the crystal structure of $Cs_2LiMn_3F_{12}$. I summarized the lattice parameter, and the atomic coordinates and site symmetries of $Cs_2LiMn_3F_{12}$ in Table 1.3 and 1.4, respectively. The magnetic Mn^{3+} ions are located at (0.5, 0, 0) in atomic coordination where the site symmetry is -1 in Hermann Mauguin notions, which leads to a kagome lattice with the regular triangle. Mn^{3+} has the high spin state that causes the Jahn-Teller effect. The elongated axis owing to the Jahn-Teller effect lie in *ab*-plane. Elongated and compressed axes in *ab* plane alternate, and the configuration of the elongated axes resembles a wind wheel, as shown in Fig 1.19(b). The nature of the nearest-neighbor exchange interaction is yet to be defined. Recent *ab-iniitio* calculation shows the nearest-neighbor exchange interaction to be ferromagnetic [117]. Magnetic Mn^{3+} ions with $S = 2$ form a uniform kagome layer parallel to the *ab*-plane, which are separated by a nonmagnetic layer consisting of the Cs_2Li. Therefore the interlayer exchange interaction is expected to be much smaller than the intralayer exchange interaction.

The magnetization measurements of $Cs_2LiMn_3F_{12}$ were conducted by Usui [118]. In temperature dependence of the magnetic susceptibility, no anomaly indicative of magnetic order was observed down to $T = 1.8$ K. Using the high-temperature expansion method [34], the exchange interaction was estimated to be $J/k_B = 4.4$ K. However, it was found that $Cs_2LiMn_3F_{12}$ undergoes the antiferromagnetic order at $T_N = 2$ K via the heat capacity measurements. Temperature dependence of the magnetic entropy S_{mag} approaches approximately $R \ln 5$ at 50 K. It was found that the polycrystalline sample of $Cs_2LiMn_3F_{12}$ contains a large number of ferromagnetic impurities, $CsMnF_4$ and Li_2MnF_5. Magnetic moment of the impurities hides the intrinsic magnetization of $Cs_2LiMn_3F_{12}$. Usui was not able to find the crystal orientation, because natural surfaces of crystal were difficult to obtain. Therefore, the high-quality single-crystal samples are necessary for more detailed measurements.

Finally, I mention the possible ground state of $Cs_2LiMn_3F_{12}$, proposed by Usui [118]. The powder elastic neutron scattering inferred that the magnetic structure of $Cs_2LiMn_3F_{12}$ is characterized by an ordering vector $\boldsymbol{q} = (1/3, 0, 0)$ [118]. To the best of my knowl-

edge, the spin structures reported to date for KLAF are the $\boldsymbol{q} = 0$ structures. Thus, $Cs_2LiMn_3F_{12}$ appears to exhibit an unusual magnetic ordered state.

Table 1.3: Lattice parameters of $Cs_2LiMn_3F_{12}$ with space symmetry $R\bar{3}$ (No. 148) as compared with those for $Cs_2Cu_3SnF_{12}$ and $Rb_2Cu_3SnF_{12}$.

	Space Group	a [Å]	c [Å]	Reference
$Cs_2Cu_3SnF_{12}$	$R\bar{3}m$	7.142(4)	20.381(14)	[101]
$Rb_2Cu_3SnF_{12}$	$R\bar{3}$	13.917(2)	20.356(3)	[100]
$Cs_2LiMn_3F_{12}$	$R\bar{3}$	7.44	17.267	[116]

Table 1.4: Atomic coordinates and site symmetries of $Cs_2LiMn_3F_{12}$ with space group has $R\bar{3}$ (No. 148). Site symmetry in Hermann-Mauguin notation represents the crystal symmetry at the point where the atoms exist. Adapted from Ref. [116]

Atom	Site Symmetry	x	y	z
Cs	3 .	0.0	0.0	0.12859
Mn	-1	0.5	0.0	0.0
F(1)	1	0.4561	0.5261	0.10126
F(2)	1	0.4103	0.1850	0.02408
Li	-3 .	0.0	0.0	0.5

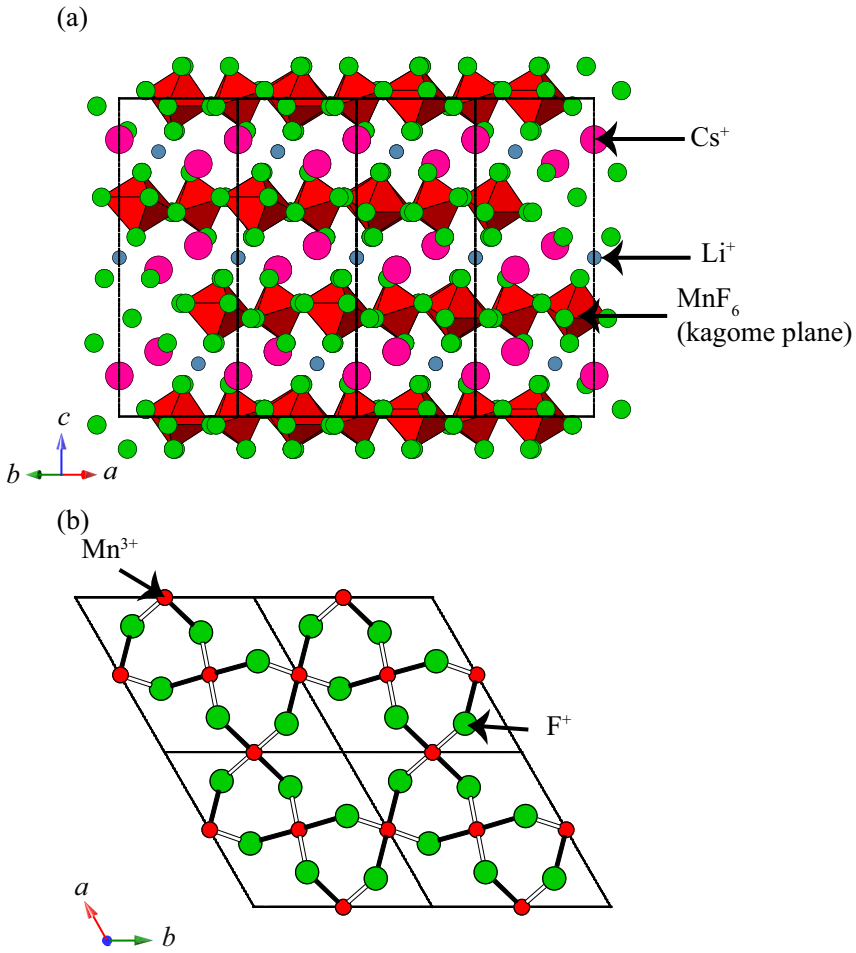

Figure 1.19: Crystal structure of $Cs_2LiMn_3F_{12}$. (a) View along the [110]-axis. Octahedra colored red represent MnF_6. The positions of the Mn^{3+} ions are located at the center of the octahedra. (b) View along c-axis, where F^- ions out of kagome-plane are deleted. Dotted lines denote the chemical unit cells. Thick black bonds denote elongated axes of MnF_6 octahedra.

1.3.3 Motivation and Outline of This Study

The kagome materials investigated, many of which are natural minerals as mentioned above, have their individual problems, which includes spatial anisotropy of the exchange network [76, 77], exchange disorder due to ion substitution [78] and lattice distortion due to a structural phase transition [79]. For these reasons, there has been little clear experimental evidence demonstrating the nature of the ground state and the excitations for the spin-1/2 Heisenberg KLAF.

In $Rb_2Cu_3SnF_{12}$, the lowest excitation is located at the Γ point, although the lowest excitation is expected to be located at the K point within the quantum Heisenberg model. This is because the large DM interaction splits the triply degenerate excitations in the triplet state into two levels, $S^z = 0$ and $S^z = \pm 1$ branches, and the energy of the $S^z = \pm 1$ branch is minimized at the Γ point with increasing the magnitude of $D^{\parallel}$ [105, 119]. If the inequivalence of the exchange interactions becomes small, it is expected that the excitation gap at the Γ point will decrease and a transition from the singlet ground state to the ordered ground state will occur. The exchange interactions in $Cs_2Cu_3SnF_{12}$ are similar to those in the uniform kagome lattice [104]. Thus, I can expect a quantum phase transition in mixed system $(Rb_{1-x}Cs_x)_2Cu_3SnF_{12}$ upon varying the cesium concentration x. I can also expect the experimental realization of the valence-bond-glass (VBG) state in $(Rb_{1-x}Cs_x)_2Cu_3SnF_{12}$, which is a spin-liquid-like ground state characteristic of frustrated quantum antiferromagnet with exchange randomness. What I mentioned above motivates me to investigate the magnetic properties of $(Rb_{1-x}Cs_x)_2Cu_3SnF_{12}$.

In $Cs_2LiMn_3F_{12}$ the crystal structure and the magnetic properties have been reported in Ref. [116, 118]. It is noteworthy that the magnetic ground state of $Cs_2LiMn_3F_{12}$ exhibits unusual $\boldsymbol{q} = (1/3, 0, 0)$ spin structure instead of $\boldsymbol{q} = 0$ structure. In the neutron scattering measurement a substantial number of intensities attributed to impurities were observed, indicating that the quality of the sample is rather poor [118]. In this thesis, I explore another way of synthesizing single crystal of $Cs_2LiMn_3F_{12}$.

The studies described in this thesis are intended to give some insights into the ground states of the KLAFs with quantum spins and classical spins. This thesis is organized as follows. In the next chapter, I will review experimental procedures that

includes preparation of the samples of a fluoride family and measurement principles, which includes magnetization measurement, specific heat measurement, elastic neutron scattering and muon spin relaxation experiments.

In Chapter 3, I show the experimental results of magnetization and thermodynamic measurements and muon spin relaxation experiments on $(Rb_{1-x}Cs_x)_2Cu_3SnF_{12}$, and discuss the nature of the ground state. I succeeded in growing high-quality single crystals of $(Rb_{1-x}Cs_x)_2Cu_3SnF_{12}$ using platinum tubes as crucibles. I performed the magnetic measurements for $H \parallel c$ and $H \perp c$ to clarify the magnetic ground states. It was found that the quantum phase transition occurs from a disordered state to a antiferromagnetic ordered state, when cesium concentration x exceeds $x_c = 0.53$. I performed muon spin relaxation for $H \parallel c$ to investigate fluctuating frequencies and values of internal magnetic fields, in the exotic magnetic ground state. Detailed analyses revealed that the VBG state, one of unusual ground states, is actually realized in $(Rb_{1-x}Cs_x)_2Cu_3SnF_{12}$.

Chapter 4 focuses on the thermal dynamics measurements and elastic neutron scattering measurements on $Cs_2LiMn_3F_{12}$ with spin-2. I succeeded in synthesizing highly purified and sizable single crystals of $Cs_2LiMn_3F_{12}$. I confirmed the crystallographic axis using x-ray diffractometer. I measured the magnetic measurements for $H \parallel c$ and $H \perp c$. It was found that $Cs_2LiMn_3F_{12}$ exhibits the antiferromagnetic order at 2 K. I analyzed experimental results using the high temperature expansion to evaluate the exchange interaction. I performed the specific heat for $H \parallel c$ and $H \perp c$ for understanding the thermodynamics. I verified that the low-temperature specific heat in the absence of the external fields is proportional to T^2, which is characteristic of the nature of two-dimensional antiferromagnets. From the powder neutron scattering with high-purity sample, I confirmed that the spin structure of the ground state is described by a propagation vector $\boldsymbol{q} = (1/3, 0, 0)$. Chapter 5 is devoted to conclusion.

Chapter 2

Experimental Detail

2.1 Sample Preparation

Fluorides have properties of hygroscopy and corrosion. On account of hygroscopy, raw materials of the compounds were dehydrated by heating in vacuum using a rotary pump before preparation. I ground the dehydrated raw materials using a mortar and pestle in a glove box. To synthesize the fluoride family, quartz ampoules and ceramic crucibles cannot be utilized owing to the corrosiveness. This is the reason why I use a platinum (Pt) tube of 9.6 mm inner diameter and 100 mm length as the crucibles as shown in Fig. 2.1(a). One end of the Pt tube was welded and another end was tightly folded with pliers and placed between nichrome plates as shown in Fig. 2.1(b). Because a rupture of the Pt tube often occurs during firing (Fig. 2.1(c)), I covered completely the whole of the Pt tube with two nichrome downspouts, which were fasten with nichrome wires in order to preclude the rupture as shown in Fig. 2.1(d).

2.1.1 $A_2Cu_3SnF_{12}$ (A = Rb, Cs)

I synthesized single crystals of $A_2Cu_3SnF_{12}$ from a melting method through the following chemical reaction: $2AF + 3CuF_2 + SnF_4 \rightarrow A_2Cu_3SnF_{12}$. Single crystals of $A_2Cu_3SnF_{12}$ (A = Cs, Rb) were grown by a similar procedure to that reported in [100,104–106,108]. AF and CuF_2 were dehydrated by heating in vacuum at about 100 °C. The dehydrated raw materials of AF, CuF_2 and SnF_4 were packed into the Pt tube in the ratio of 3 : 3 : 2. Single crystals were grown from the melting using

Figure 2.1: (a) Pt tube used for sample preparation, where one end is welded. (b) Pt tube with the other end folded and placed between nichrome plates. (c) Pt tube after rupture. (d) Pt tube covered with with two nichrome downspouts and fasten with nichrome wires.

the horizontal tube furnace manufactured by Yamada Denki Co., LTD. As depicted in Fig. 2.2, the temperature at the center of the tube furnace was lowered from $T_{\rm high}$ to $T_{\rm low}$ over 100 hours, for A = Cs (resp. A = Rb), $T_{\rm high}$ = 850 (800)°C and $T_{\rm low}$ = 750 (700)°C, respectively. After collecting the well-formed pieces of crystal, I repeated the same procedure to improve the quality of the single-crystal samples. As can be seen in Fig. 2.3, transparent light-green crystal of $Cs_2Cu_3SnF_{12}$ with a maximum size of 30 × 7 × 2 mm^3 were obtained.

After picking up the purified single crystals of $Cs_2Cu_3SnF_{12}$ and $Rb_2Cu_3SnF_{12}$, I synthesized the solid solution of $(Rb_{1-x}Cs_x)_2Cu_3SnF_{12}$ single crystals from a melt comprising a mixture of $Rb_2Cu_3SnF_{12}$ and $Cs_2Cu_3SnF_{12}$ in the ratio of $1-x$ to x. The single crystals of $(Rb_{1-x}Cs_x)_2Cu_3SnF_{12}$ were easily cleaved parallel to the c-axis.

The cesium concentration x was determined by inductively coupled plasma mass spectroscopy (ICP-MS) at the Center for Advanced Materials Analysis, Tokyo Institute of Technology.

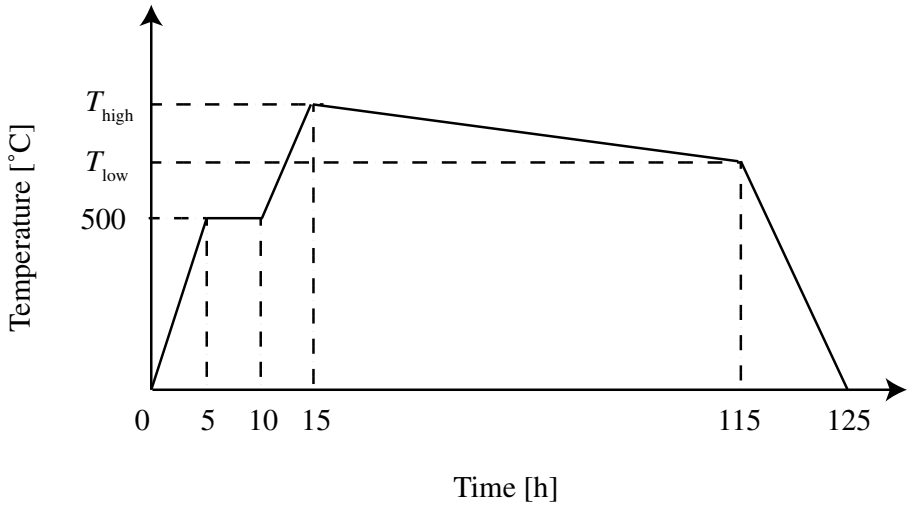

Figure 2.2: Time dependence of temperature at the center of horizontal furnace.

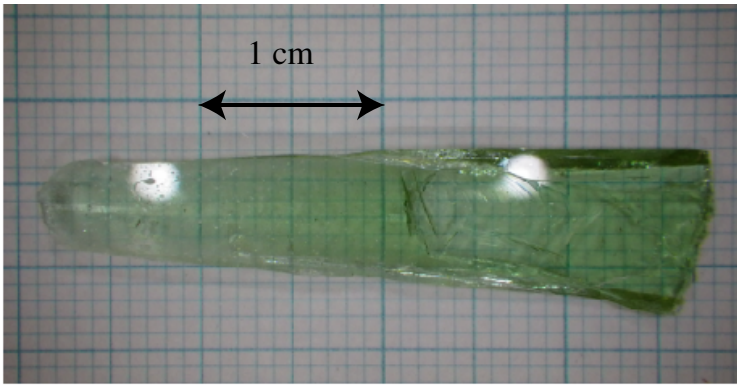

Figure 2.3: Photograph of $Cs_2Cu_3SnF_{12}$ single crystal.

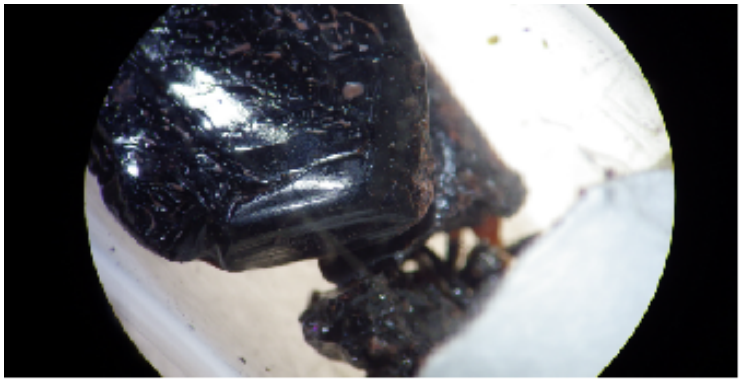

Figure 2.4: Photograph of a black single crystal of $Cs_2LiMn_3F_{12}$ through a microscope.

2.1.2 $Cs_2LiMn_3F_{12}$

I synthesized $Cs_2LiMn_3F_{12}$ single crystals from a melting method through the following chemical reaction $LiF + 2CsF + 3MnF_3 \rightarrow Cs_2LiMn_3F_{12}$.

CsF, MnF_3 and LiF were dehydrated by heating in vacuum at about 100 °C. First the materials were packed into the Pt tube in the ratio of $3:3:1$, as reported by Usui [118]. A synthetic breakthrough was made by changing the ratio to $2:4:1$. Sizable single crystals were grown from the melting method with this ratio.

The temperature of the furnace was lowered from 875 to 675 °C over 100 hours. After collecting the well-formed pieces of crystal, I repeated the same procedure. As can be seen in Fig. 2.4, the crystallographic axis and the cleavage plane were easily identified at a glance. I utilized a X-ray diffractometer, MiniFlexII manufactured by Rigaku Corp., to determine the c-plane of $Cs_2LiMn_3F_{12}$.

2.2 Magnetization measurement

Magnetic susceptibilities were measured in magnetic fields of up to 7 T in the temperature range $1.8 - 400$ K using a SQUID magnetometer (Quantum Design: MPMS XL). Magnetic fields were applied parallel and perpendicular to the c-axis.

The SQUID detection system in MPMS is composed of the SQUID sensing loops,

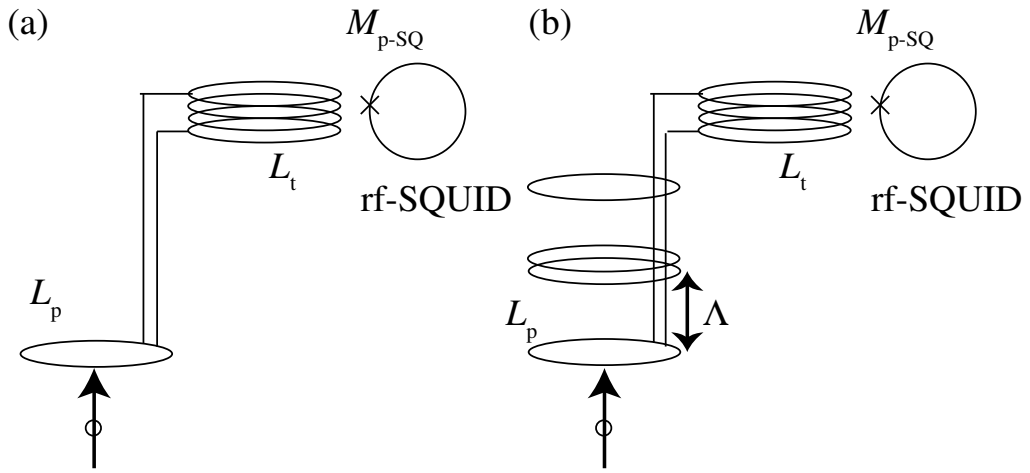

Figure 2.5: Schematic figure of superconducting transformer configurations (pick up coil) in MPMS. (a) Magnetometer configuration. (b) Second derivative gradiometer.

a superconducting transformer, SQUID sensor, and control electronics [120]. The SQUID sensing loops are separated by SQUID sensor and consists of a closed loop of superconducting wire.

When a magnetic flux $\delta\Phi_{\text{sample}}$ induced by a sample is applied to the pick-up coil, induced super-current $\delta i(\delta\Phi_{\text{sample}})$ emerges. The induced direct current produces magnetic flux $\delta\Phi_{\text{SQUID}}$ applied to the SQUID. Let the mutual inductance $M_{\text{p-SQ}}$ between the pick up coil and SQUID,

$$\delta i(\delta\Phi_{\text{sample}}) = -\frac{\delta\Phi_{\text{sample}}}{L_{\text{t}} + L_{\text{p}}}, \tag{2.1}$$

$$\delta\Phi_{\text{SQUID}} = \delta i(\delta\Phi_{\text{sample}}) M_{\text{p-SQ}}. \tag{2.2}$$

Thus, I am necessary to evaluate how much magnetic flux $\delta\Phi_{\text{sample}}$ transfer to the SQUID $\delta\Phi_{\text{SQUID}}$.

A radio frequency (RF) coil with flux locked loop and negative feedback are utilized [121, 122]. Once the feedback loop is closed, the SQUID is applied another magnetic flux $\delta\Phi_{\text{FB}}$ produced by the feedback current

$$\delta\Phi_{\text{FB}} = M_{\text{FB}}\delta I_{\text{FB}} = \frac{M_{\text{FB}}}{R_{\text{FB}}}\delta V_{\text{out}} = -\delta\Phi_{\text{SQUID}}, \tag{2.3}$$

where R_{FB} and M_{FB} are the resistivity of the feedback, and the mutual inductance between feedback coil and SQUID, respectively. This equation shows that the flux

$\delta\Phi_{\mathrm{SQUID}}$ is proportional to the output voltage δV_{out} and no flux are now applied to SQUID. The same voltage δV_{out} is simultaneously applied to a integrator in the parallel circuit. Thus, after the feedback, when the flux $\delta\Phi_{\mathrm{SQUID}}$ increments, the output voltage δV_{out} should remain proportional to $\delta\Phi_{\mathrm{SQUID}}$. The feedback system is called the flux locked loop. The integrator integrates δV_{out}, the amount of output voltage V_{out} should be linearized the sample flux Φ_{sample}. The SQUID response is shown in Fig. 2.6(a).

MPMS execute the fit for the output voltage [123]

$$\begin{aligned} V_{\mathrm{out}}(Z) =& X(1) + X(2)\cdot Z + X(3)\cdot\Big\{2\left[R^2+(Z+X(4))^2\right]^{-3/2} \\ &- \left[R^2+(\Lambda+Z+X(4))^2\right]^{-3/2} - \left[R^2+(-\Lambda+Z+X(4))^2\right]^{-3/2}\Big\} \end{aligned} \tag{2.4}$$

where, the parameter $X(1), X(2), X(3),$ and $X(4)$ are a constant offset voltage, a linear electronic drift, amplitude for the output voltage, the shift of the sample along the axis of the magnet, respectively. Figure 2.4(b) shows the output voltage given by Eq. (2.4). The magnetic moment M can be obtained from $X(3)$ by applying Eq. (2.4)

$$M = \alpha X(3), \tag{2.5}$$

where α is a coefficient.

2.3 Heat Capacity Measurement

Specific heat measurements were conducted by Physical Property Measurement System (PPMS, Quantum Design) with the relaxation method. Magnetic field up to 9 T was applied along c-axis and kagome plane. Sample temperature was lowered to 0.4 K using Helium-3 Refrigerator option developed by Quantum Design Inc.. The sample was mounted on the sample stage in a sample puck with a little grease as depicted in Fig. 2.7. Since the sample chamber is in high vacuum during measurement, the platform is thermally isolated.

The relaxation method, first explored by Bachmann *et al.* [124], is widely utilized in a field of the low temperature physics. The schematic diagram is depicted in

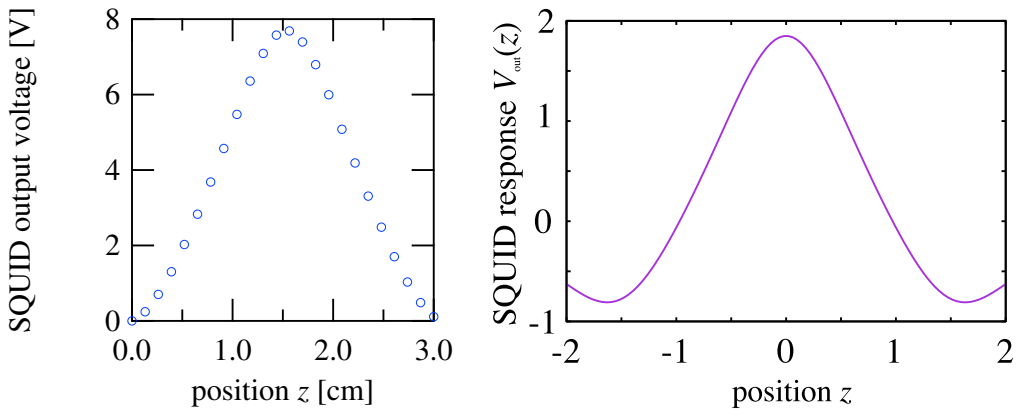

Figure 2.6: (a) Typical SQUID response as function of the sample position z and (b) response with Eq. 2.4, where the parameters $X(1) = X(2) = X(4) = 0, X(3) = 1, R = 0.97,$ and $\Lambda = 1.517$ are used.

Fig. 2.7. The system is composed of a sample, substrate including a heater and thermometer, thermal leak and heat reservoir. From $t = 0$, power is applied to the substrate through the heater, which is squirreled away in the internal energy of the sample and substrate, and dissipating into the heat reservoir via the thermal leak. The Fourier law shows that the dissipating heat should be proportional to temperature difference between the two. When the heater power is turned off at a time t_0, the temperature is being lowered down to the temperature of the reservoir, T_0. The energy balance could be described as

$$P(t) = C_{\rm tot}{\rm d}T/{\rm d}t + K(T - T_0), \tag{2.6}$$

where $C_{\rm tot}, T, K$ are heat capacity of the sample and substrate, temperature of the substrate, and heat conductance of the thermal leak, respectively. Using Laplace transformation, the solution for the temperature is given by

$$\begin{aligned} T(t) = T_0 + \frac{P_0}{K}(1 - {\rm e}^{-t/\tau})\{\Theta(t) - \Theta(t - t_0)\} \\ + \frac{P_0}{K}(1 - {\rm e}^{-t_0/\tau}){\rm e}^{-(t-t_0)/\tau}\{\Theta(t - t_0)\} \end{aligned} \tag{2.7}$$

where $\tau = C_{\rm tot}/K, \Theta(t)$ are the relaxation time, Heaviside step function, respectively. Figure 4.3 shows the time dependence of temperature given by Eq. (2.7)

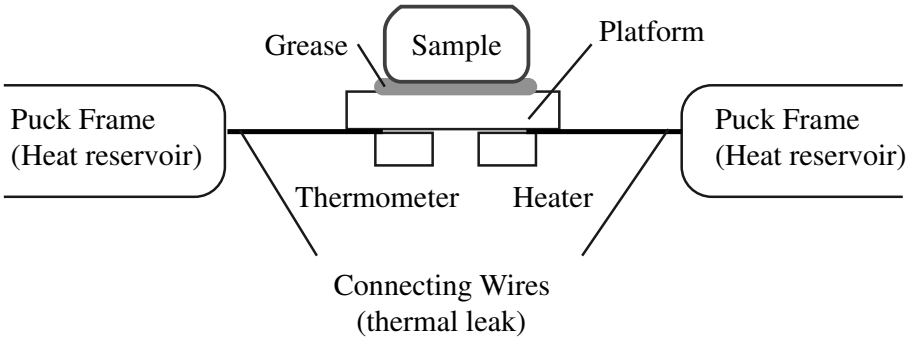

Figure 2.7: Schematic figure of heat capacity measurement with the relaxation method.

In reality, there exists thermal conductance between the sample and substrate due to sample preparation such as grease. In that case, different regions of the sample could be at different temperatures and the solution for the temperature is a sum of exponentials [124]. However, when the individual temperature of the sample and substrate are uniform and the thermal conductance is comparable to that between the substrate and heat reservoir, the only two components are dominant, which is referred to the lumped two-effect [125].

The equations for the energy balance are as follow

$$0 = C_{\mathrm{s}}\mathrm{d}T_{\mathrm{s}}/\mathrm{d}t + K_{\mathrm{sp}}(T_{\mathrm{s}} - T_{\mathrm{p}}) \tag{2.8}$$

$$P(t) = C_{\mathrm{p}}\mathrm{d}T_{\mathrm{p}}/\mathrm{d}t + K_{\mathrm{pb}}(T_{\mathrm{p}} - T_0) + K_{\mathrm{sp}}(T_{\mathrm{p}} - T_{\mathrm{s}}) \tag{2.9}$$

The first equation is for the sample, and the second equation for the substrate. Since the thermometer monitors the temperature of the substrate, I need to solve T_{p}. Using Laplace transformation, the solution is given by

$$\begin{aligned} T_{\mathrm{p}}(t) = T_0 + \frac{P_0}{K_{\mathrm{pb}}}\left(1 - \frac{\tau - \tau_2}{\tau_1 - \tau_2}\mathrm{e}^{-t/\tau_1} - \frac{\tau_1 - \tau}{\tau_1 - \tau_2}\mathrm{e}^{-t/\tau_2}\right)\{\Theta(t) - \Theta(t - t_0)\} \\ + \frac{P_0}{K_{\mathrm{pb}}}\left\{\frac{\tau_2 - \tau}{\tau_1 - \tau_2}\mathrm{e}^{-(t-t_0)/\tau_1}\left(\mathrm{e}^{-t_0/\tau_1} - 1\right) + \frac{\tau - \tau_1}{\tau_1 - \tau_2}\mathrm{e}^{-(t-t_0)/\tau_2}\left(\mathrm{e}^{-t_0/\tau_2} - 1\right)\right\}\Theta(t - t_0) \end{aligned} \tag{2.10}$$

A nonlinear, least square fitting was executed by PPMS to obtain $K_{\mathrm{pb}}, \tau, \tau_1,$ and τ_2.

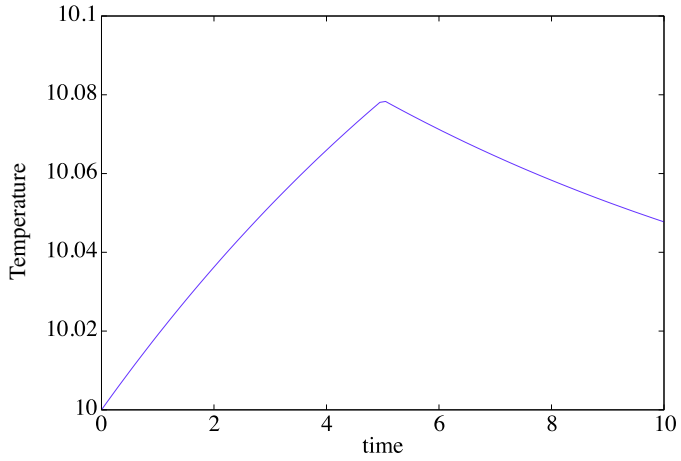

Figure 2.8: Time dependence of temperature given by one τ model with Eq. (2.7). The parameters, $T_0 = 10, P_0/K = 10 \times 0.02, t_0 = 5,$ and $\tau = 10$, are used.

2.4 Neutron Scattering Measurement

Neutron scattering is the most suitable to probe crystal and spin structure and excitation. Neutrons is scattered by the so-called strong interaction and the magnetic dipole of atoms. This indicates that the diffraction intensity, or scattering length, is independent of atomic numbers and magnetic spin structure can be determined. Thus, neutron scattering is available to determine the crystal structure with light elements and magnetic structure, instead of x-ray diffraction measurements [126–128].

2.4.1 Elastic Neutron Diffraction

The neutron powder diffraction experiments were performed using the high-resolution powder diffractometer Echidna installed at the OPAL reactor, ANSTO with a neutron wavelength of 2.4395 Å. Figure 2.9 shows the arrangement of the Echidna diffractometer. The sample was placed in a cylindrical vanadium can. The sample temperature was lowered down to 1.5 K.

Here, I summarize the elastic neutron scattering diffraction. The Bragg's law is described as,

$$2d \sin\theta = n\lambda, \tag{2.11}$$

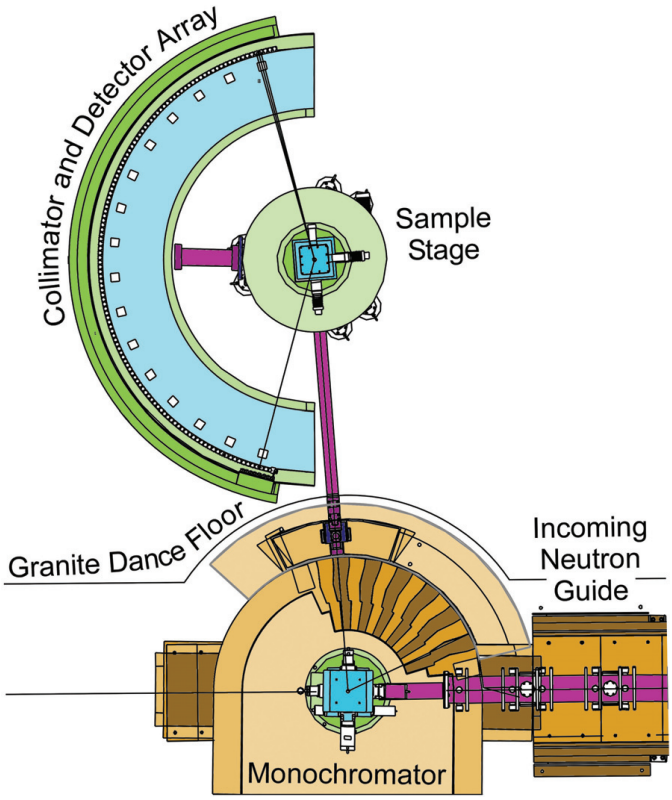

Figure 2.9: View of Echidna spectrometer at Australian Nuclear Science and Technology Organisation (ANSTO) reprinted from Ref. [129]. Echidna is a high resolution powder diffractometer.

where d, θ, n, and λ are the spacing between the adjacent layers of atoms, the angle between the incident rays and the layer, a integer, and the wave length, respectively.

Although the angle of the diffraction is determined from the Bragg's law, the intensity of diffraction cannot be obtained. The diffraction intensity is given by

$$A = \sum_n f_n \exp\left(-\mathrm{i}\boldsymbol{K}\cdot\boldsymbol{r}_n\right), \tag{2.12}$$

where f_n, $\boldsymbol{r}_n$, and $\boldsymbol{K}$ are the atomic form factor and the position at n-site atom and the scattering vector, respectively, and the sum runs the whole of the crystal. The scattering vector $\boldsymbol{K}$ is given by $\boldsymbol{K} = \boldsymbol{k}_i - \boldsymbol{k}_f$, where $\boldsymbol{k}_i$ and $\boldsymbol{k}_f$ are wave vectors of incident and scattered neutrons, respectively, as shown in Fig. 2.10. The cross section from scattering should be $4\pi\sum_n f_n^2$.

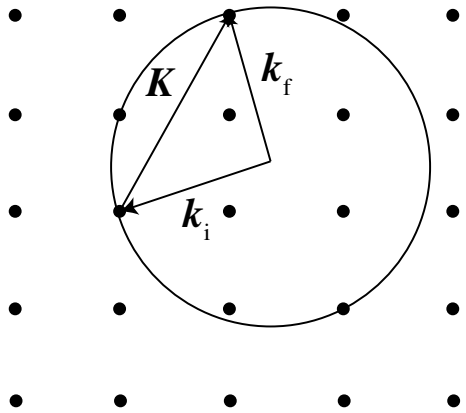

Figure 2.10: Definition of scattering vector $\boldsymbol{K}$ in the reciprocal lattice space. $\boldsymbol{k}_i$ and $\boldsymbol{k}_f$ are wave vectors of incident and scattered neutrons, respectively.

A reciprocal lattice vector $\boldsymbol{G}_{hkl}$ is given by

$$\boldsymbol{G}_{hkl} = h\boldsymbol{a}^* + k\boldsymbol{b}^* + l\boldsymbol{c}^*, \tag{2.13}$$

where $\boldsymbol{a}^*,\ \boldsymbol{b}^*,$ and $\boldsymbol{c}^*$ are three basis unit vector in reciprocal space, and $h,\ k,$ and l are integers. These vector can be satisfied with

$$\boldsymbol{G}_{hkl} \cdot \boldsymbol{a} = 2\pi h, \quad \boldsymbol{G}_{hkl} \cdot \boldsymbol{b} = 2\pi k, \quad \boldsymbol{G}_{hkl} \cdot \boldsymbol{c} = 2\pi l, \tag{2.14}$$

where $\boldsymbol{a}, \boldsymbol{b},$ and $\boldsymbol{c}$ are three basis unit vector in real space.

A crystal structure comprise Bravais lattice and basis structure. The position at n site can deduced as

$$\boldsymbol{r}_n = \boldsymbol{r}_l + \boldsymbol{r}_p, \tag{2.15}$$

where l and p are the number of the lattice and basis structure, respectively. Using Eq. (2.15), the diffraction intensity A can be given by,

$$A = \left\{ \sum_l \exp(-\mathrm{i}\boldsymbol{K} \cdot \boldsymbol{r}_l) \right\} \times \left\{ \sum_p f_p \exp\left(-\mathrm{i}\boldsymbol{K}\boldsymbol{r}_p\right) \right\}. \tag{2.16}$$

The first term is considered as the Bragg's raw. Once the scattering vector $\boldsymbol{K}$ is corresponded with the reciprocal lattice vector $\boldsymbol{G}_{hkl}$, the first term remains finite and the diffraction will be observed. Figure 2.10 shows the scattering vector in the

reciprocal space. The second term is called the structure factor, which determines the diffraction intensity.

The intensity of scattered neutrons from magnetic materials can be described using partial differential scattering cross section $\mathrm{d}\sigma^2/\mathrm{d}\Omega\mathrm{d}E$ [127]. The partial differential scattering cross section is defined as the number of neutrons scattered per second per unit incident flux into a range of solid angle $\mathrm{d}\Omega$ and with range of energies between E and $\mathrm{d}E$. In general, it is written by

$$\frac{\mathrm{d}\sigma^2}{\mathrm{d}\Omega\ \mathrm{d}E} = \frac{(\gamma r_0)^2}{2\pi\hbar}\ \frac{k_\mathrm{f}}{k_\mathrm{i}} \sum_{\alpha\beta} (\delta_{\alpha\beta} - \kappa_\alpha\kappa_\beta) \int \langle S_\alpha(-\boldsymbol{\kappa}, 0) S_\beta(\boldsymbol{\kappa}, t)\rangle \exp(-\mathrm{i}\omega t)\ \mathrm{d}t \quad (2.17)$$

where α and β are the matrix component, $\boldsymbol{k}_i$ and $\boldsymbol{k}_f$ are the wave vectors of incident and final neutrons. γ is a gyromagnetic ratio for neutrons, r_0 is the classical radius of the electron, $\langle ... \rangle$ is the thermal average at the temperature, $\boldsymbol{\kappa}$ is the scattering vector defined as $\boldsymbol{\kappa} = \boldsymbol{k}_f - \boldsymbol{k}_i$, and S is related to the magnetization operator M

$$S_\beta(\boldsymbol{\kappa}, t) = \exp(\mathrm{i}\mathcal{H}t/t)\ S_\beta(\boldsymbol{\kappa}) \exp(-\mathrm{i}\mathcal{H}t/t), \quad (2.18)$$

$$\boldsymbol{S}(\boldsymbol{\kappa}) = -\frac{1}{2\mu_\mathrm{B}} \sum_n \boldsymbol{M}(\boldsymbol{r}_n) \exp(\mathrm{i}\boldsymbol{\kappa}\cdot\boldsymbol{r}_n). \quad (2.19)$$

To obtain the elastic cross section, Eq. (2.17) replaces the matrix element by the values as $t \to \infty$. The correlation function $\langle S_\alpha(-\boldsymbol{\kappa}, 0) S_\beta(\boldsymbol{\kappa}, t)\rangle$ becomes independent of t. As can be seen in Eq. (2.16), let $\boldsymbol{G}_\mathrm{M}$ be a wave vector of the magnetic reciprocal lattice, $\langle \boldsymbol{S}(\boldsymbol{\kappa})\rangle$ can only be finite for $\boldsymbol{\kappa} = \boldsymbol{G}_\mathrm{M} = \boldsymbol{G}_{hkl} \pm \boldsymbol{q}$, where $\boldsymbol{q}$ is called an ordering vector. Thus, in the ordered states, the cross section is given by

$$\frac{\mathrm{d}\sigma}{\mathrm{d}\Omega} = \frac{(\gamma r_0)^2}{2\pi\hbar} \left| -\frac{1}{2\mu_\mathrm{B}} \sum_p \langle \boldsymbol{M}_\perp(\boldsymbol{r}_p)\rangle \exp(\mathrm{i}\boldsymbol{\kappa}\cdot\boldsymbol{r}_p) \right|^2 \delta(\boldsymbol{\kappa} - \boldsymbol{G}_\mathrm{M}). \quad (2.20)$$

$\boldsymbol{M}_\perp$ represents the component perpendicular to $\boldsymbol{\kappa}$ of a spin in the unit cell of the magnetic structure.

2.5 Muon Spin Relaxation

Muon spin relaxation μSR experiment is a powerful tool to investigate the static and dynamical nature of spins, which includes fluctuating frequencies and values

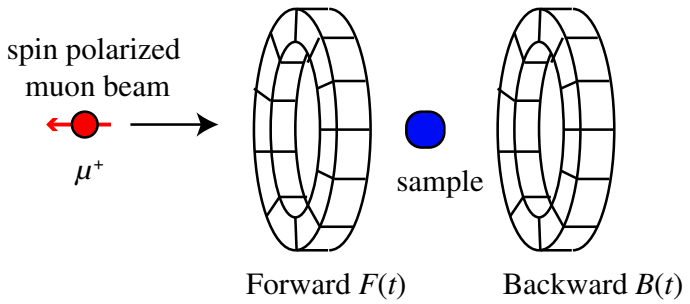

Figure 2.11: Schematic view of muon relaxation measurements. Positive muon μ^+ (red circle) is perfectly polarized opposite to the momenta. Decay of a μ^+ creates positron e^+, which can be detected by two circular detectors placed before and after the sample.

of internal magnetic fields, in the magnetic ground state. Decay of a positive pion produces a positive muon whose spin is perfectly polarized opposite to their momenta. When the polarized muons are implanted into a sample, it is possible to detect relaxation time of muon spin. Since the muon beam is already polarized before entering the sample, the magnetic properties of sample can be studied in the absence of the fields.

In this study, μSR measurements were carried out at the RIKEN-RAL Muon Facility in the U.K. using a spin-polarized double-pulsed positive surface-muon beam with an incident muon momentum of 27 MeV/c. Single crystals were mounted on a high-purity silver plate by an Apiezon N grease, and were covered tightly by a high-purity silver foil to ensure thermal contact between the samples and a silver plate which is connected directly with the cold- head of ^{3}He refrigerator. The incident muon-spin direction is perpendicular to the ab-plane corresponding to the kagome plane, and the direction of external longitudinal magnetic fields is parallel to the c-axis. Forward and backward counters were located on the upstream and downstream sides of the beam direction shown in Fig. 2.11, which was parallel to the initial muon-spin direction. The asymmetry $A(t)$ was defined as follows:

$$A(t) = \frac{F(t) - \alpha B(t)}{F(t) + \alpha B(t)} \tag{2.21}$$

Here, $F(t)$ and $B(t)$ were total muon events counted by the forward and backward counters at a time t respectively. The α is a calibration factor reflecting relative

counting efficiencies between the forward and backward counters, and is determined by the muon-spin-rotation in the transverse field of 20 G. The initial asymmetry is defined as $A(0)$. In this study, the calibration factor α and the background subtraction were taken into account for the data analysis. All μSR time spectra, except for Fig. 3.10, are plotted using the corrected asymmetry which is normalized by $A(0)$. The detail of the background is explained in the next section. Measured μSR time spectra were analyzed using the WiMDA computer program.

Chapter 3

Quantum Phase Transition in $(Rb_{1-x}Cs_x)_2Cu_3SnF_{12}$

As mentioned in Chapter 1, since the ground states in $Rb_2Cu_3SnF_{12}$ and $Cs_2Cu_3SnF_{12}$ are different, the solid solution of these two compounds is expected to exhibit the quantum phase transition from a disordered state to a ordered state. Besides, the ion substitutions between Rb and Cs will generate randomness of strength of interactions that can induce the exotic ground state of a valence bond glass (VBG), which has not been observed experimentally in KLAF. In this chapter, I present the results of magnetic and thermodynamic measurements conducted in $(Rb_{1-x}Cs_x)_2Cu_3SnF_{12}$ and discuss the results. As shown below, I observe the systematic change in the exchange parameters with cesium concentration x and clear quantum phase transition from a disordered state to a ordered state. The disordered phase is found to be VBG.

3.1 Magnetic and Thermodynamic Properties

3.1.1 Systematic Change in Exchange Parameters

Figure 3.1 shows X-ray powder diffraction pattern of $(Rb_{1-x}Cs_x)_2Cu_3SnF_{12}$ obtained using MiniFlexII (Rigaku), which indicates that the diffraction pattern changes systematically with x. I confirmed that the Bragg peaks are as sharp as those in pure cases with $x = 0$ and 1. This result is evidence of high homogeneity of the crystals. Figure 3.2 shows the temperature dependence of the heat capacity above 150 K

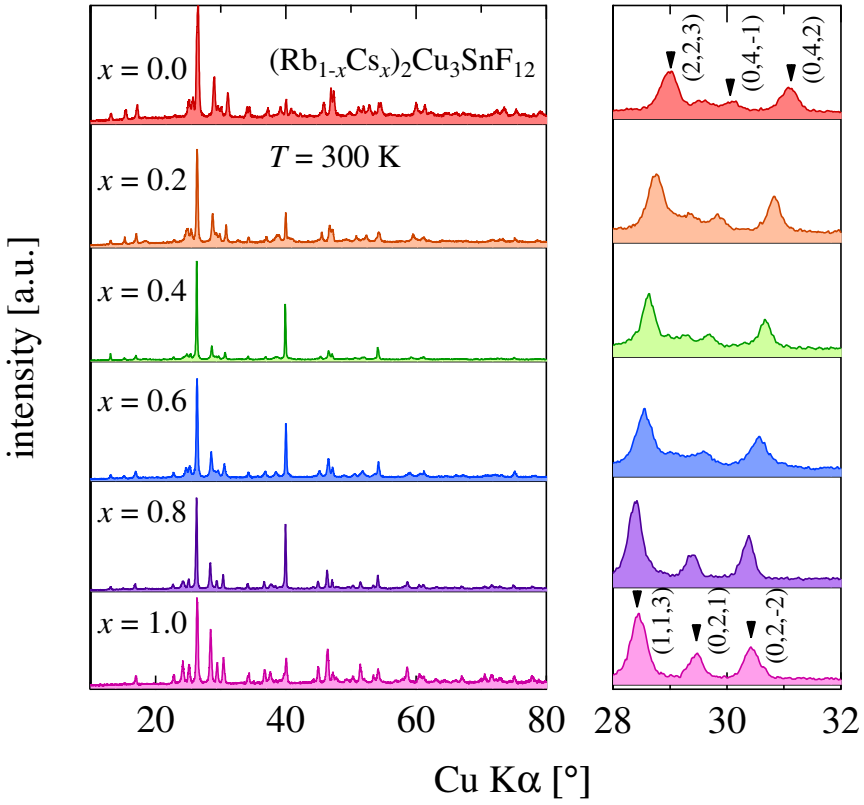

Figure 3.1: X-ray powder diffraction pattern in $(Rb_{1-x}Cs_x)_2Cu_3SnF_{12}$ measured at room temperature.

for $Rb_2Cu_3SnF_{12}$ and $Cs_2Cu_3SnF_{12}$. Anomalies indicative of structural phase transitions are observed at $T_{s1} = 278$ K and $T_{s2} = 215$ K for $Rb_2Cu_3SnF_{12}$ and $T_s = 180$ K for $Cs_2Cu_3SnF_{12}$. The structural phase transitions in $Rb_2Cu_3SnF_{12}$ were not detected by the magnetic susceptibility measurements [100], while for $Cs_2Cu_3SnF_{12}$, the structural phase transition was observed as small bend anomaly in the temperature dependence of magnetic susceptibility [101].

Figure 3.3 shows the temperature dependence of the magnetic susceptibility χ of $(Rb_{1-x}Cs_x)_2Cu_3SnF_{12}$ measured at $H = 1$ T for $H \parallel c$ for various x. The data for $x \leq 0.47$ are corrected for the Curie-Weiss term attributable to impurities and/or randomness in exchange interactions. With decreasing temperature, the suscep-

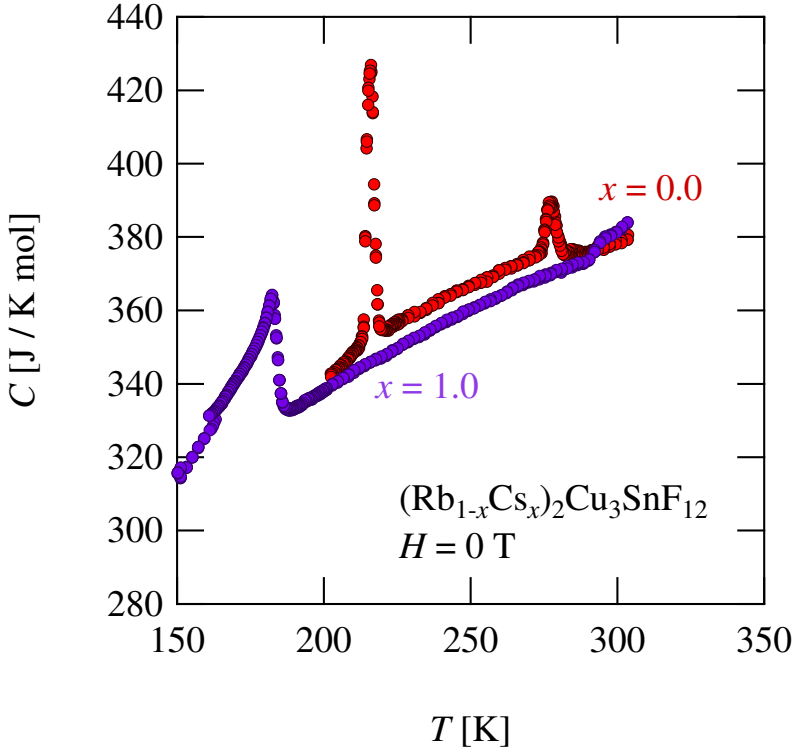

Figure 3.2: Temperature dependence of specific heat of $Rb_2Cu_3SnF_{12}$ and $Cs_2Cu_3SnF_{12}$ measured for $T \geq 150$ K. Anomalies indicative of structural phase transitions are observed at $T = 278$ K and 215 K for $Rb_2Cu_3SnF_{12}$ and $T = 180$ K for $Cs_2Cu_3SnF_{12}$.

tibility for $Rb_2Cu_3SnF_{12}$ ($x = 0$) exhibits a rounded maximum at approximately $T_{max} = 70$ K and decreases to zero, indicating a gapped singlet ground state. As the cesium concentration x is increased, T_{max} decreases and the magnetic susceptibility has a finite value at $T = 0$. With further increasing x, a kink anomaly indicating magnetic ordering is observed. Details of the low-temperature susceptibility will be discussed later. For $Cs_2Cu_3SnF_{12}$ ($x = 1.0$), the small bend anomaly shown by an arrow, indicating a structural phase transition, was observed at $T_t = 184$ K, as previously reported [101]. For $x = 0.81$, the bend anomaly due to the structural phase transition occurs at $T_t = 295$ K. This indicates that T_t increases with decreasing x. These results also indicates that the magnetic susceptibility is not given by the superposition of those for $Rb_2Cu_3SnF_{12}$ and $Cs_2Cu_3SnF_{12}$, which confirms the

homogeneity of crystals.

To investigate the systematic change in exchange parameters with cesium concentration x, I analyze the magnetic susceptibilities,using the exact diagonalization of a 12-site kagome cluster under a periodic boundary condition. Assuming that the configuration of the nearest-neighbor exchange interaction shown in Fig. 1.15 is common to all $(Rb_{1-x}Cs_x)_2Cu_3SnF_{12}$ on average, I evaluate the exchange parameters J_i $(i = 1 - 4)$. For $Cs_2Cu_3SnF_{12}$ $(x = 1)$ I assume a uniform kagome lattice for simplification as in Ref. [101].

The procedure of the exact diagonalization calculation is the same as that described in Ref. [100,101]. I executed the exact diagonalization for the 12-site kagome cluster under the periodic boundary condition. First, I calculated the uniform case, $J_1 = J_2 = J_3 = J_4 = 1$, to confirm the accuracy of our calculation. The result obtained is the same as that shown in Ref. [132], which was calculated by the exact diagonalization for the 12-site kagome cluster. The calculated results were also close to the results obtained from the exact diagonalization for the 24-site kagome cluster [133].

From the fitting to the high-temperature magnetic susceptibility for $T > 200$ K, I evaluate the average exchange interaction $J_{\rm avg} = (J_1 + J_2 + J_3 + J_4)/4$. For $Rb_2Cu_3SnF_{12}$ $(x = 0)$, I confirmed that the magnetic susceptibility above 60 K is satisfactorily reproduced using $J_1/k_{\rm B} = 216$ K, $J_2 = 0.95J_1$, $J_3 = 0.85J_1$ and $J_4 = 0.55J_1$ obtained from the analysis of the dispersion relations [105], as shown in Fig. 3.3. This confirms that individual values of J_i/J_1 can be estimated from the fitting to the low-temperature magnetic susceptibility for $T < 200$ K. For $0 < x < 1$, I found that the calculated susceptibility is less sensitive to J_3 for $0.5 \leq J_3/J_1 \leq 1.0$. Thus, J_3/J_1 cannot not be determined uniquely. Hence, I estimate only J_2/J_1 and J_4/J_1. I fit the calculated results to the susceptibility data for $H \parallel c$. The solid lines in Fig. 3.3(a) are fits with the parameters shown in Fig. 3.4. I also performed the same analysis on the susceptibility data for $H \perp c$, as shown by solid lines in Fig. 3.3(b). The exchange parameters shown in Fig. 3.4 are obtained by the fitting for both $H \parallel c$ and $H \perp c$. In the present analysis, I neglect the DM interaction because its effect on the susceptibility for $T > 60$ K is expected to be small [104].

As shown in Fig. 3.3, the calculated susceptibilities accurately reproduce the experimental susceptibilities for $T > 60$ K in all $(Rb_{1-x}Cs_x)_2Cu_3SnF_{12}$, while for

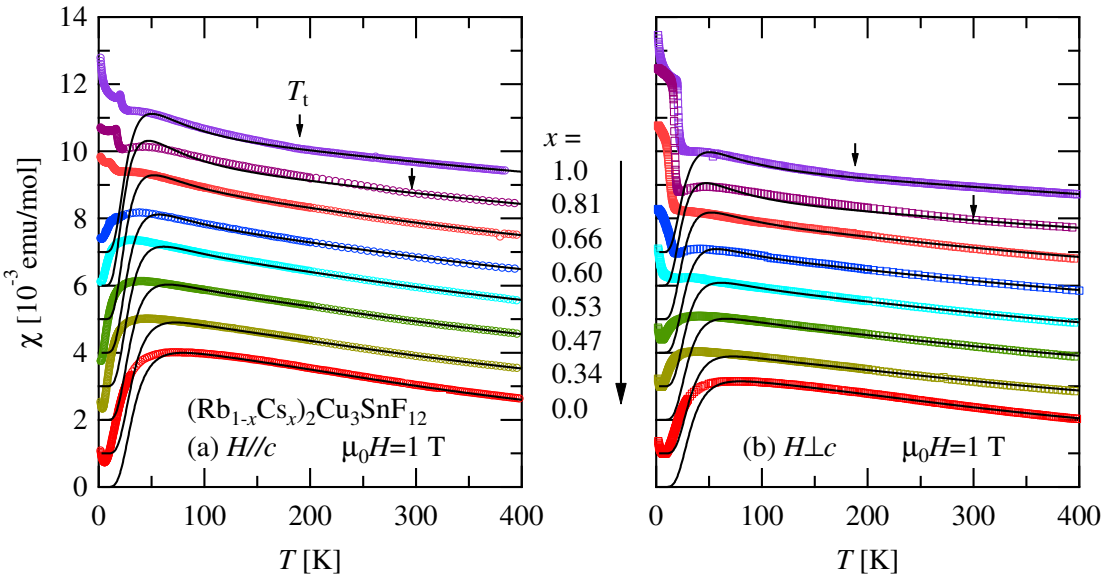

Figure 3.3: Temperature dependence of magnetic susceptibility of $(Rb_{1-x}Cs_x)_2Cu_3SnF_{12}$ measured at $H = 1$ T for $H \parallel c$ for various x. The susceptibility data are shifted upward by multiples of 2×10^{-3} emu/mol. The data for $x \leq 0.47$ are corrected for the Curie-Weiss term attributable to impurities and/or randomness in exchange interactions. Arrows indicate anomalies associated with structural phase transitions. Solid curves are fits using the theoretical susceptibilities obtained from the exact diagonalization of a 12-site kagome cluster (see text).

$T < 60$ K, the calculated susceptibility decreases more rapidly than the experimental susceptibility. This should be due to the finite-size effect. Figure 3.4 summarizes the x dependence of the magnetic parameters for $(Rb_{1-x}Cs_x)_2Cu_3SnF_{12}$ determined from the susceptibility analyses using the exact diagonalization calculations. $g_{\parallel}$ and $g_{\perp}$ denote the g factors for $H \parallel c$ and $H \perp c$, respectively. I incorporate the g factor into the fitting parameters because it is difficult to determine the g factor by the usual electron paramagnetic resonance because of the extremely large line-width arising from the large DM interaction. The g factors obtained with the present analysis are independent of x. The magnitude of the g factors, i.e., $g_{\parallel} = 2.4 - 2.5$ and $g_{\perp} = 2.1$, are consistent with those for K_2CuF_4 and Rb_2CuF_4 [134]. As shown Fig. 3.4(b), the average of the four sorts of exchange interactions $J_{\rm avg}$ increases

monotonically as $x \to 1$. J_4/J_1 increases rapidly with increasing x. The calculated susceptibility is insensitive to J_3 for $0.5 \leq J_3/J_1 \leq 1.0$, as mentioned above. Because the smallest J_4/J_1 increases with increasing x, I infer that all the exchange interactions approach a uniform value for $x \to 1$.

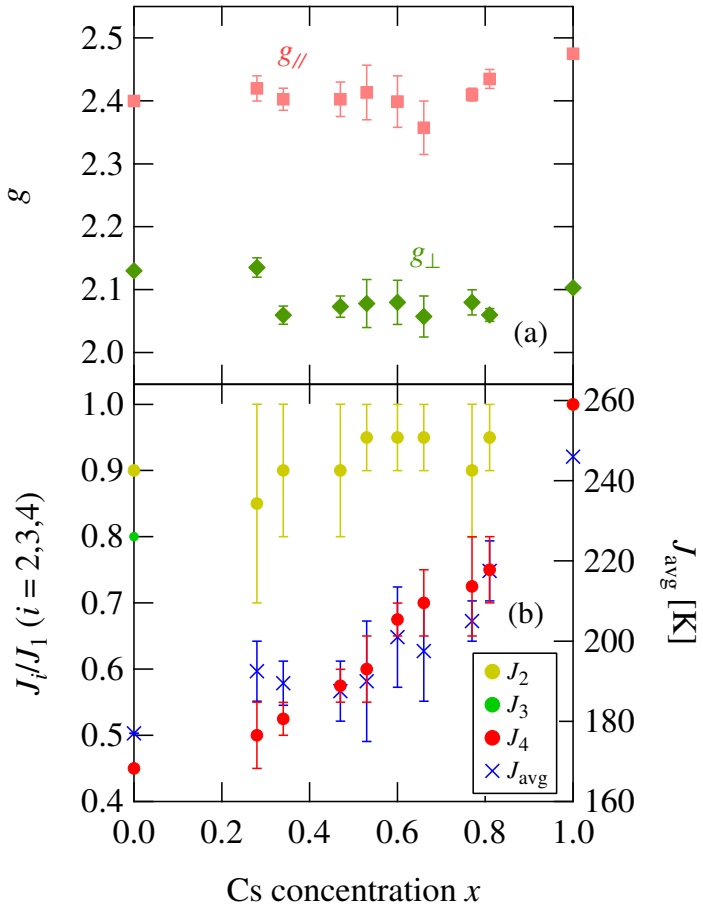

Figure 3.4: g-factors and exchange parameters as a function of the cesium concentration x in $(Rb_{1-x}Cs_x)_2Cu_3SnF_{12}$ evaluated from the analyses of magnetic susceptibilities. The upper panel shows $g_{\parallel}$ and $g_{\perp}$ for $H \parallel c$ and $H \perp c$, respectively. The lower panel shows the individual exchange parameters normalized by J_1 and the averaged exchange interaction J_{avg}.

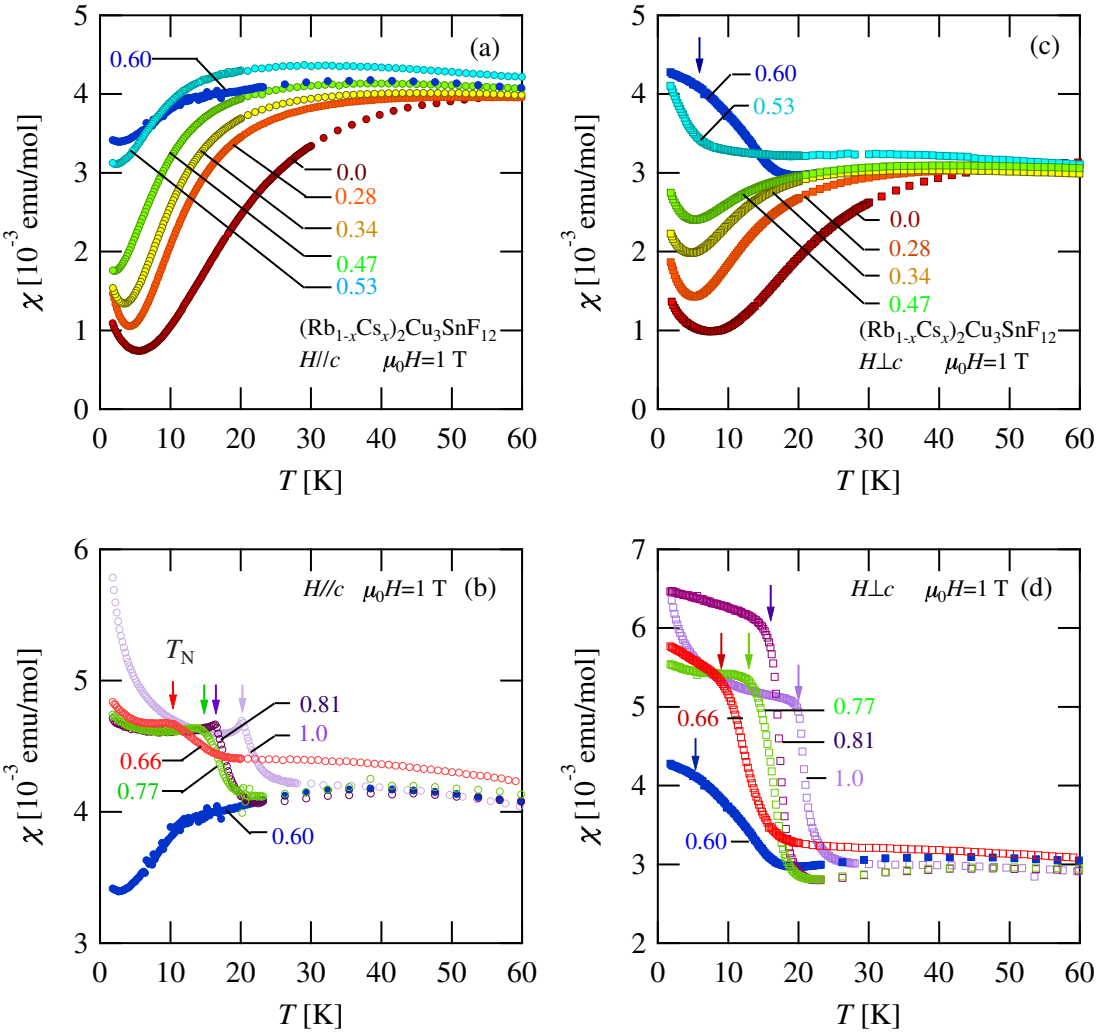

Figure 3.5: Low-temperature magnetic susceptibility of $(Rb_{1-x}Cs_x)_2Cu_3SnF_{12}$ for various x measured at $H = 1$ T (a) and (b) for $H \parallel c$, and (c) and (d) for $H \perp c$. (a) and (c) show the data for $0 \leq x \leq 0.60$, and (b) and (d) show the data for $0.60 \leq x \leq 1.0$. Arrows indicate the ordering temperature T_N.

3.1.2 Quantum Phase Transition

Next, I examine the low-temperature magnetic susceptibility of $(Rb_{1-x}Cs_x)_2Cu_3SnF_{12}$ to investigate the ground states. Figure 3.5 shows the magnetic susceptibilities below 60 K in $(Rb_{1-x}Cs_x)_2Cu_3SnF_{12}$ measured at $H = 1$ T for $H \parallel c$ and $H \perp c$ for various x. For $x \leq 0.47$, the susceptibility exhibits a small upturn below 7 K. This should be ascribed mainly to the impurity phase, because the small upturn is observed even in pure $Rb_2Cu_3SnF_{12}$. With increasing x, the temperature $T_{\max}$ giving the rounded maximum of susceptibility decreases. This behavior of susceptibility is considered to be related to the fact that the exchange interactions become uniform with increasing x. The low-temperature susceptibility for $x \leq 0.47$ corrected for the upturn below 7 K shows exponential temperature dependence indicative of the presence of an excitation gap. For $x \leq 0.53$, no anomaly indicative of magnetic ordering is observed. This shows that the ground state is disordered for $x \leq 0.53$. On the other hand, the susceptibility for $x \geq 0.60$ exhibits kink or bend anomalies, which are indicative of magnetic ordering. For $x = 0.60$, I assigned the temperature at which a small bend anomaly appears for $H \perp c$ as the ordering temperature T_N.

Figure 3.6 shows the temperature dependence of the specific heat for $Cs_2Cu_3SnF_{12}$. A tiny cusp anomaly owing to magnetic ordering is observed at $T_N = 20.0$ K. This ordering temperature coincides with T_N assigned from the anomaly in the susceptibility. The very small anomaly in the specific heat around T_N indicates that little entropy remains for magnetic ordering because of the well-developed short-range spin correlation caused by the large exchange interaction of $J/k_B \simeq 240$ K and good two-dimensionality. For $x \neq 1$, the specific heat anomaly is so small that it is difficult to detect the magnetic ordering.

The transition data obtained from the low-temperature susceptibilities are summarized in Fig. 3.7. With decreasing x from $x = 1$, the ordering temperature T_N decreases, and T_N reaches zero at $x_c \simeq 0.53$.

I analyze the low-temperature susceptibility for $x \leq 0.47$ using the following formula:

$$\chi(T) = \frac{C}{T - \Theta} + A \exp\left(-\frac{\Delta}{k_B T}\right) + \chi_0, \tag{3.1}$$

where the first term is the Curie-Weiss term, the second term represents the low-

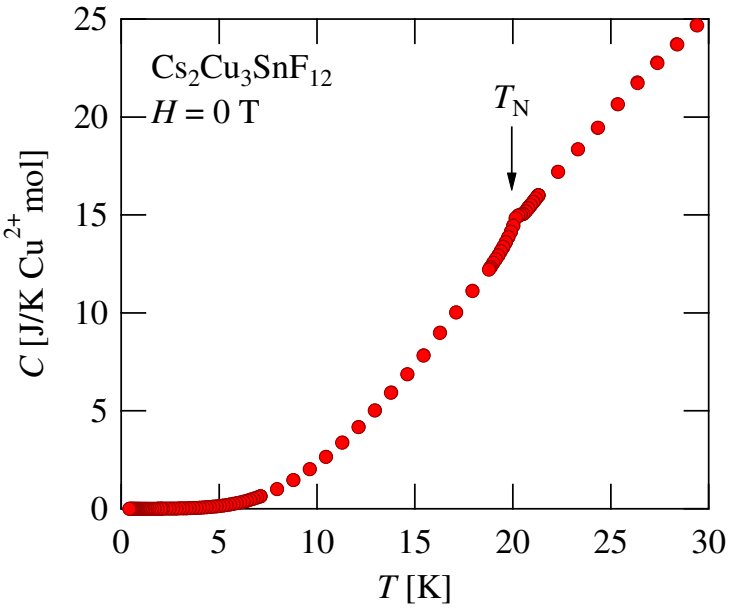

Figure 3.6: Specific heat of $Cs_2Cu_3SnF_{12}$ as a function of temperature measured at zero magnetic field. The arrow indicates the ordering temperature T_N.

temperature susceptibility for two-dimensional systems with an excitation gap Δ [135, 136], and the last constant term arises from the finite susceptibility component in the ground state. Here, the value of χ_0 was evaluated from the magnetization curves of $(Rb_{1-x}Cs_x)_2Cu_3SnF_{12}$ with $0 \leq x \leq 0.47$ for $H \parallel c$ at 1.8 K, which is shown in Fig. 3.8. The magnetization data have been corrected for impurity contributions, which are assumed to follow the Brillouin function. The impurity concentration were evaluated to be between 0.4 % and 0.7 %.

For $Rb_2Cu_3SnF_{12}$ ($x = 0$), the highest applied field of 7 T is smaller than the critical field $H_c = 13$ T, where the excitation gap closes [100, 101]. The magnetization slope below 2 T is very small but finite, from which the residual susceptibility χ_0 is estimated to be $\chi_0 \simeq 1 \times 10^{-4}$ emu/mol. The residual susceptibility χ_0 for $H \perp c$ is estimated as $\chi_0 \simeq 4 \times 10^{-4}$ emu/mol, which is four times larger than that for $H \parallel c$. The finite χ_0 is attributed to the small transverse component $D^{\perp}$ of the $\boldsymbol{D}$ vector for the DM interaction [137].

For $x \leq 0.47$, the magnetization below 2 T is proportional to magnetic field H, as shown in Fig. 3.8. For $x = 0.47$, magnetization increases rapidly up to $H_c \sim 6.2$

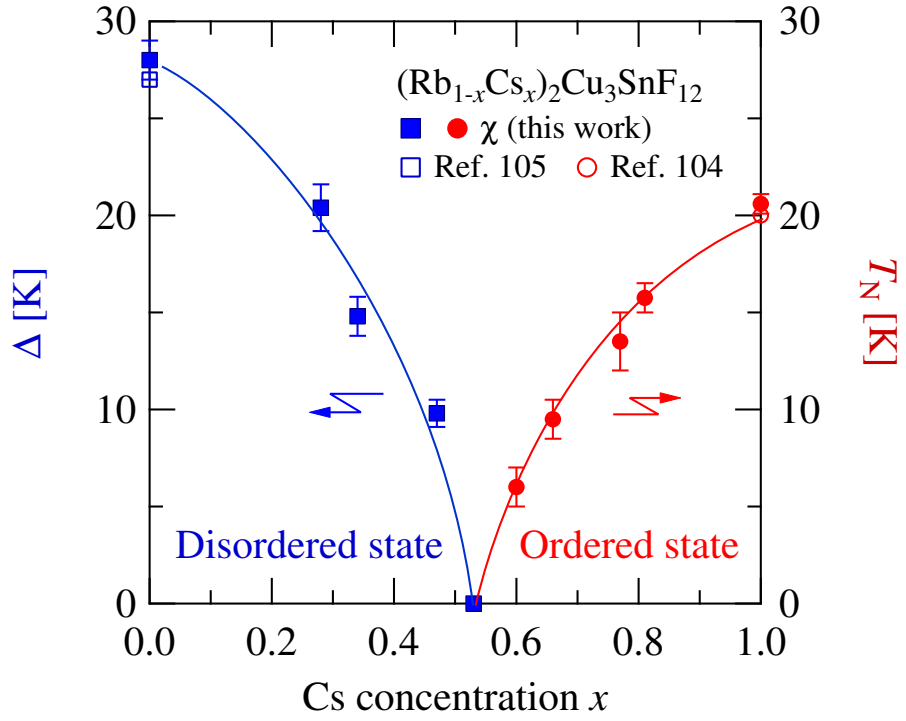

Figure 3.7: Phase diagram of the spin gap Δ and Néel temperature T_N for $(Rb_{1-x}Cs_x)_2Cu_3SnF_{12}$, determined via magnetic measurements with $H \parallel c$. Δ is estimated by fitting the susceptibility data using eq. (3.1). Results obtained in other measurements [104, 105] are also shown for comparison.

T and increases linearly with increasing magnetic field. The magnitude of the gap ($\Delta/k_B \simeq 9.8\,K$) for $x = 0.47$ is consistent with that obtained from the low-temperature susceptibility using Eq. (3.1), as shown below. Figure 3.9 summarizes the residual susceptibility χ_0 for $x \leq 0.47$ estimated from the magnetization slope. The residual susceptibility χ_0 is finite for $H \parallel c$ even in the disordered ground state and exhibits a rapid increase with increasing x. The ground state for $x \leq 0.47$ is unusual, because the magnetic susceptibility is finite, nevertheless the magnetic ordering is absent.

Fitting Eq. (3.1) to the low-temperature susceptibility of $Rb_2Cu_3SnF_{12}$ for $H \parallel c$ with $\chi_0 \simeq 1 \times 10^{-4}$ emu/mol, I obtain $\Delta/k_B = 28$ K, which is consistent with $\Delta/k_B = 27$ K observed by neutron inelastic scattering [105,106]. This guarantees the validity of

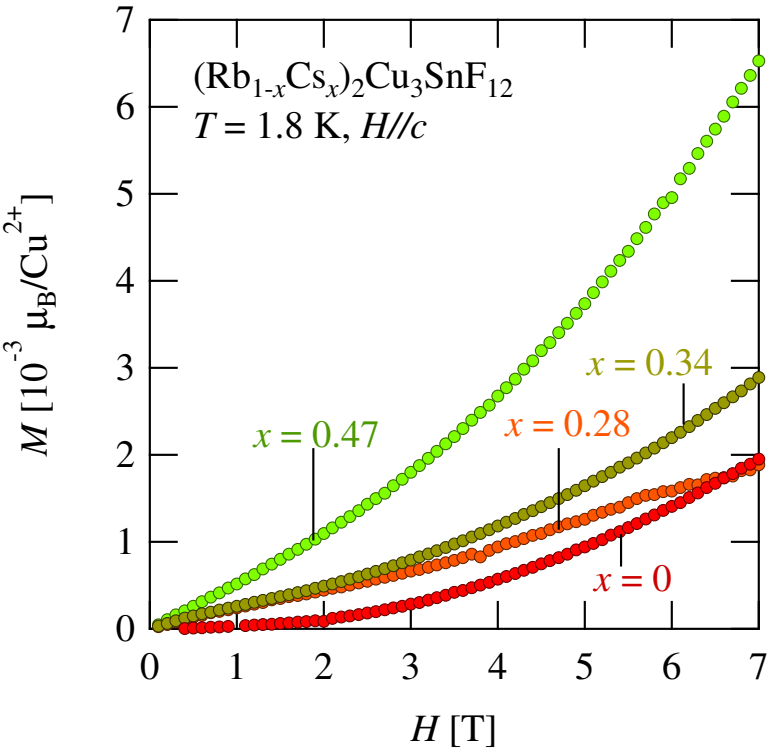

Figure 3.8: Magnetization curves of $(Rb_{1-x}Cs_x)_2Cu_3SnF_{12}$ measured for $H \parallel c$ at $T = 1.8$ K. The data were corrected for impurity contributions represented by the Brillouin function.

the present analysis. The x dependence of the excitation gap Δ obtained by fitting Eq. (3.1) with χ_0 shown in Fig. 3.9 is shown in Fig. 3.7. With increasing x from $x = 0$, Δ diminishes and vanishes at $x_c \simeq 0.53$. Because both the excitation gap Δ and the ordering temperature T_N become zero at $x_c \simeq 0.53$, I can deduce that a quantum phase transition from the disordered state to the ordered state takes place at $x = x_c$. Therefore, $x_c \simeq 0.53$ should be the quantum critical point.

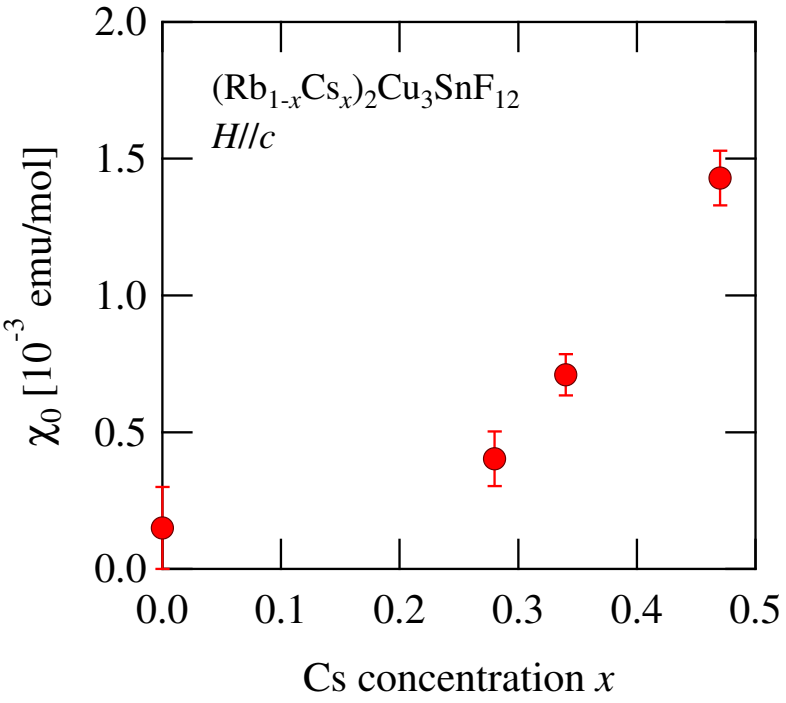

Figure 3.9: Residual susceptibility χ_0 for $H \parallel c$ in the disordered ground state for $0 \leq x \leq 0.47$.

3.2 μSR Measurement on Sample with $x_c = 0.53$

As mentioned above, I found that the quantum phase transition from a disordered state to an antiferromagnetic ordered state in $(Rb_{1-x}Cs_x)_2Cu_3SnF_{12}$ occurs at the critical concentration $x_c \simeq 0.53$. Physical properties near and at the quantum phase transition point are one of current subjects of condensed matter physics. I conducted μSR measurements on $(Rb_{1-x}Cs_x)_2Cu_3SnF_{12}$ with $x_c = 0.53$, which is at the quantum critical point, to investigate their ground state nature. In this section, I report the spin dynamics obtained by the zero- and longitudinal-field muon-spin-relaxation.

For $x_c = 0.53$, no magnetic order was observed in magnetic measurements down to 1.8 K, as shown in previous section. Figure 3.10 shows the zero field and longitudinal field μSR time spectra for $x = 0.53$ at 0.3 K. Since the sample is a fluoride, a rotational behavior in ZF time spectra was observed in absence of applied fields owing to a coupling via a dipole-dipole interaction between μ^+ spin and nuclear spin of F^- ions. To unveil the dynamics of Cu^{2+} spins from the time spectra, longitudinal magnetic fields (LF) above 200 G were applied to suppress the dipole-dipole interaction between μ^+ spin and nuclear spin of F^- ions. The rotational signal with low frequencies disappears, and a relaxation spectrum appears.

Figure 3.11(a) shows the temperature dependence of LF-μSR time spectra of $(Rb_{1-x}Cs_x)_2Cu_3SnF_{12}$ with $x = 0.53$. The spin polarization of the implanted muons appears to relax exponentially, which indicates that spins of the sample fluctuate with frequencies. Thus, I analyzed the LF-μSR time spectra using the following formula

$$A(t) = A_0 \exp(-\lambda t) \qquad (T \geq 4 \text{ K}), \tag{3.2}$$

$$A(t) = A_1 \exp(-\lambda_1 t) + A_2 \exp(-\lambda_2 t) \qquad (T < 4 \text{ K}). \tag{3.3}$$

where λ_1, λ_2 and λ are muon spin relaxation rates in each component. Below 4 K, the time spectra are bended, and a function with two components is necessary to reproduce the time spectra. It was found that the ratio A_1/A_2 is fixed to be $\simeq 1.4$. Above 4 K, spin polarization tends to display an exponential decay. All spectra in Fig. 3.11(a) are well fitted by the Eq. (3.2) and Eq. (3.3). Figure 3.11(b) shows temperature dependence of the deduced relaxation rates, λ_1, λ_2 and λ. With

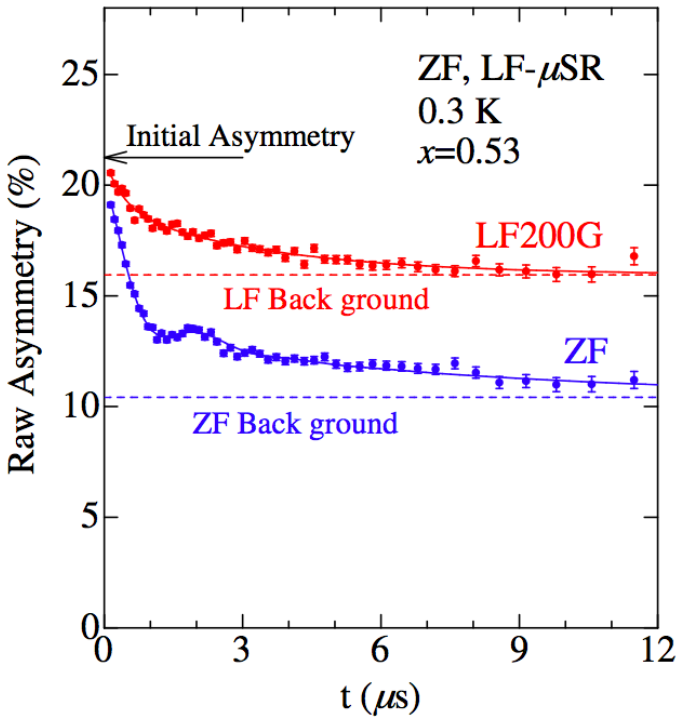

Figure 3.10: Typical μSR time spectra measured at zero magnetic field (ZF) and in a longitudinal magnetic field (LF) of 200 G. Time dependence of the raw asymmetry is plotted. Dashed lines denote the backgrounds in both cases.

decreasing temperature, the relaxation rates show a monotonous increase. This indicates an enhancement of spin fluctuation in low frequencies at lower temperature, because the relaxation rates are in inverse proportion to the spin fluctuation as long as the applied fields are relatively low.

To obtain further understanding of the spin dynamics, LF-dependence measurements are needed. In many cases of magnetic disordered states, magnetic moments in materials and implanted muon spins weakly interact with one another through the dipole-dipole interaction. With increasing the applied fields, the muon spins decoupled from the internal magnetic field caused by electron spins in magnetic materials, so that the relaxation rates of muon spins will decrease. Magnetic field dependence of the muon-spin-relaxation rate λ is described by the Redfield formula expressed as

$$\lambda(H_{\mathrm{LF}}) = \frac{2\gamma_\mu^2 H_{\mathrm{loc}}^2 \tau}{1 + \gamma_\mu^2 H_{\mathrm{LF}}^2 \tau^2}, \tag{3.4}$$

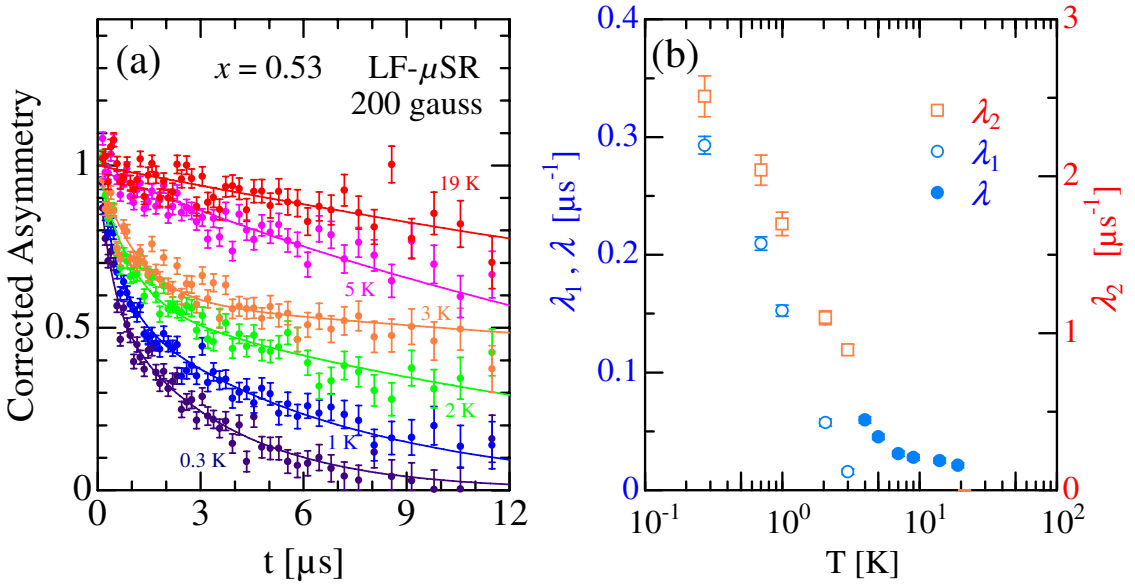

Figure 3.11: (a) LF-μSR time spectra of $(Rb_{1-x}Cs_x)_2Cu_3SnF_{12}$ with $x = 0.53$ measured at various temperature in $H_{LF} = 200$ gauss. Solid line are fitted results using the Eq. (3.2) and Eq. (3.3). (b) Temperature dependence of the muon spin relaxation rates.

where γ_μ is the gyromagnetic ratio of the muon spin ($2\pi \times 13.5534$ kHz/gauss), H_{LF} is the external longitudinal-field, H_{loc} is the internal local magnetic field at the muon sites, and τ is the correlation time of muon spins. When the fluctuating frequency of the internal field at the muon sites has a single component, the LF dependence of $\lambda(H_{LF})$ has a cutoff structure, and one can deduce the fluctuating frequency $f = 1/\tau$ using Eq. (3.4).

Figure 3.12 shows LF-μSR time spectra measured at 0.3, 2, and 4 K in various fields. Using Eqs. (3.3) and (3.2), I analyze LF-μSR spectra for 0.3 K and 2 K and for 4 K, respectively. All the spectra are well fitted. I fixed he ratio A_1/A_2 to the same value, when I analyze the temperature dependence of LF-μSR time spectra at 200 gauss. Figure 3.13 shows the longitudinal field dependence of muon-spin-relaxation rates λ_1, λ_2, and λ. Figure 3.13(a) shows the case of 0.3 K, and Fig. 3.13(b) shows the case of 0.3 K, 2 K, and 4 K for λ and λ_1.

I found that at 4 K, the LF dependence of the muon spin relaxation rate $\lambda(H_{LF})$ is almost constant below 4000 gauss as shown in Fig. 3.13 (b). With decreasing

temperature, the relaxation rates increase at lower fields $H_{\rm LF}$, although no cutoff structure is observed in each case. This infers that $\lambda(H_{\rm LF})$ can be described by the superposition of the Redfield formula with a widely spread distribution of the local magnetic fields $H_{\rm loc}$ and the fluctuating frequencies f at the muon sites, which is called the "white" spectrum. I infers that internal local magnetic fields fluctuate at frequencies lower than an order of MHz at least down to 0.3 K. From the LF-μSR measurements, I conclude that at the quantum critical point $x_{\rm c} = 0.53$, the Cu^{2+} spins in the kagome lattice fluctuate at lower frequencies at least down to 0.3 K.

The ground state of $(Rb_{1-x}Cs_x)_2Cu_3SnF_{12}$ with $x = 0.53$ has VBG state, as mentioned in the previous section. The VBG state with a finite magnetic susceptibility is characterized by long-range valence bond correlations and is not related to any magnetic ordering. The measurement results is not inconsistent with those theoretical predictions. I infer that the "white" spectrum is attributable to VBG state that emerges in tightly bound spin singlets, loosely bound spin singlets, and nearly free spins in random interaction network. However, in order to determine the magnetic ground state experimentally, measurements at lower temperatures are needed. LF-μSR measurements at the dilution refrigerator temperature region are now on progress.

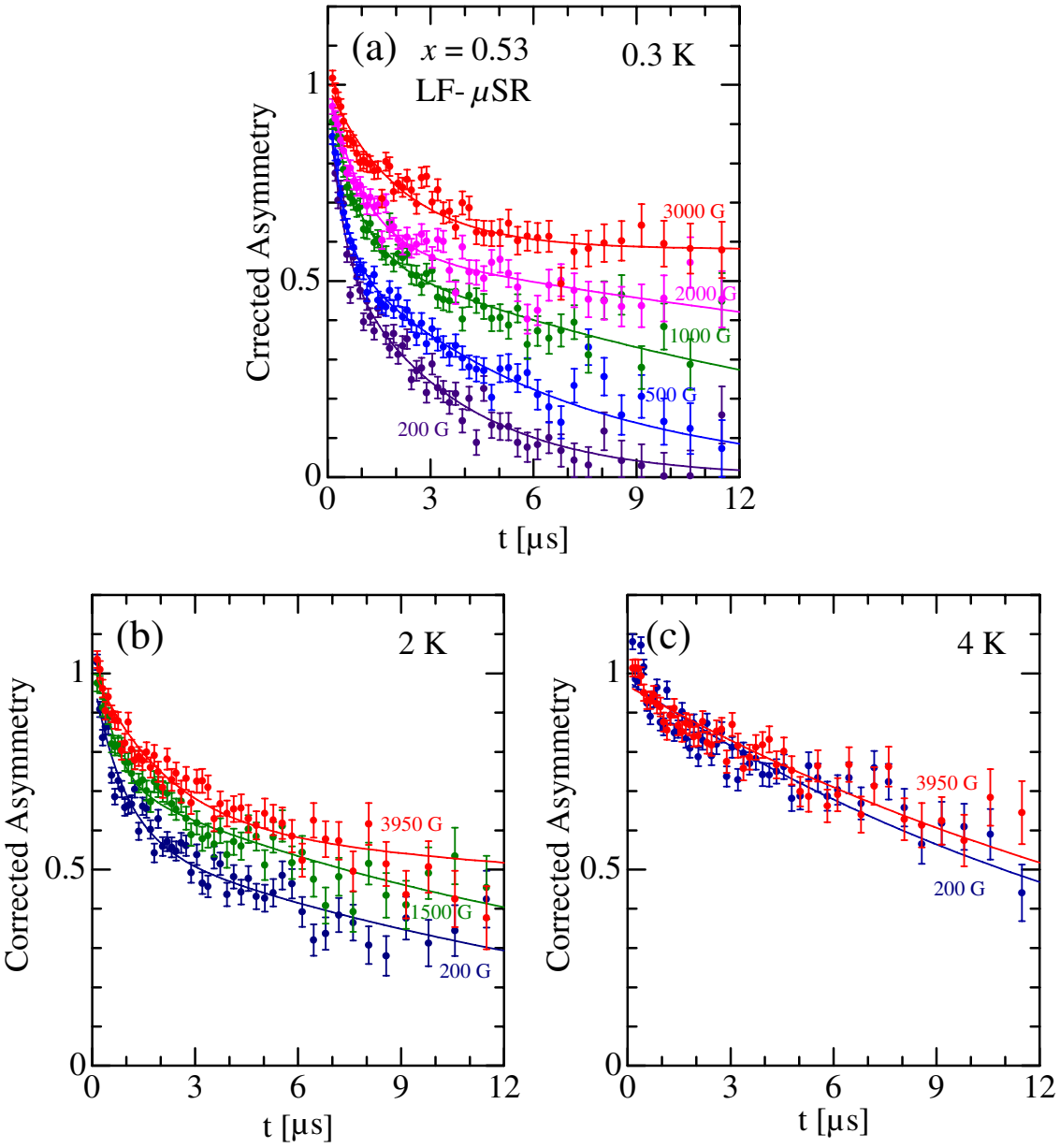

Figure 3.12: LF-μSR time spectra of $(Rb_{1-x}Cs_x)_2Cu_3SnF_{12}$ with $x = 0.53$ measured at (a) 0.3 K, (b) 2 K, and (c) 4 K. Solid lines are fitted results using the Eq. (3.3)

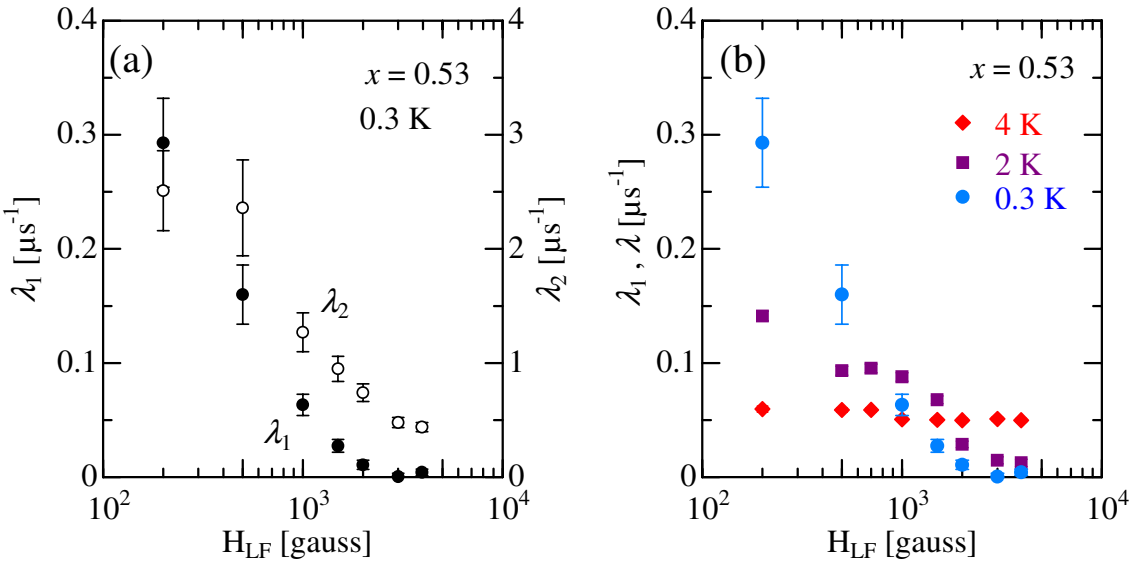

Figure 3.13: Longitudinal field dependence of muon spin relaxation rates of $(Rb_{1-x}Cs_x)_2Cu_3SnF_{12}$ with $x = 0.53$. (a) λ_1 and λ_2 at 0.3 K. (b) λ_1 at 0.3 K and 2 K, and λ at 4 K.

3.3 Discussion

From the magnetic susceptibility measurements, I observed that with increasing cesium concentration x, $(Rb_{1-x}Cs_x)_2Cu_3SnF_{12}$ undergoes the quantum phase transition from the disordered state to the ordered state at $x_c = 0.53$. I also found that the ground state for $0 < x \leq 0.53$ has a finite magnetic susceptibility, nevertheless the ground state exhibit no long-range magnetic ordering. The absence of the magnetic ordering was confirmed via the μSR measurements conducted on the sample with critical concentration $x_c = 0.53$. Thus, the ground state for $0 < x \leq 0.53$ is just like a gapless spin liquid. The substitution between rubidium and cesium ions will create exchange randomness. As shown in subsection 3.1.1, all the exchange interactions approach a uniform value for $x \to 1$. Therefore, the magnitude of exchange randomness increases with decreasing x from $x = 0$. Thus, it is natural to assume that the spin-liquid-like ground state arises from the randomness of the exchange interaction. In what follows, I discuss the nature of the "spin-liquid-like" ground.

As mentioned in Chap. 1, the ground states for the quantum triangular lattice antiferromagnet (TLAF) and quantum KLAF with bond randomness have been discussed theoretically [56–58]. It was predicted that when the randomness exceeds a critical value, the ground state changes from an ordered state with 120° structure to a gapless spin-liquid-like state for quantum TLAF, while for quantum KLAF, the ground state changes from a quantum disordered state to a gapless spin-liquid-like state. The gapless spin-liquid-like state was argued to be a "valence-bond-glass (VBG) state" or "random singlet state". The VBG state is a state in which tightly bound spin singlets are localized on stronger bonds, while loosely bound singlets are situated on weaker bonds, as shown in Fig. 1.9. Because there are many loosely bound singlets, in which the singlet-triplet excitations are gapless or close to be gapless, the magnetic susceptibility becomes finite. However, any long-range magnetic order is absent. To summarize, the VBG state has characteristics as follows [55–58, 70]:

- Magnetic excitation is gapless.
- There is no long-range order.
- Low-temperature specific heat is proportional to temperature.

The first two characteristics coincides with the ground state nature observed in $(Rb_{1-x}Cs_x)_2Cu_3SnF_{12}$ with $0 < x \leq 0.53$. The T-linear specific heat has not been clearly observed, because it is difficult to separate the magnetic and lattice contributions. When a pure parent system has a gapped singlet ground state, the mixed system creates numberless magnetic states inside the gap, which makes a gapless ground state. Consequently, the gap becomes a pseudo gap when the bond randomness is introduced [70]. Thus, I infer that the gap observed in $(Rb_{1-x}Cs_x)_2Cu_3SnF_{12}$, which is shown in Fig. 3.7, is the pseudo gap modified from the pure gap in $Rb_2Cu_3SnF_{12}$. From these experimental results and theoretical backgrounds, I can deduce that the ground state of $(Rb_{1-x}Cs_x)_2Cu_3SnF_{12}$ with $0 < x \leq 0.53$ is VBG state.

Theoretical magnetic susceptibility for $S = 1/2$ random bond Heisenberg KLAF exhibits fairly large Curie term in the gapless spin-liquid-like state, while the experimental magnetic susceptibility shown in Fig. 3.5 displays small Curie term. I consider that this discrepancy arises from the finite size effect in calculation. The theoretical magnetic susceptibility was calculated, using exact diagonalization for up to 30-site clusters. Therefore, unpaired spins created on the boundary cannot form spin singlet. These unpaired spins will form any singlet when the system size is increased, so that the Curie term decreases. It is considered that for this reason, the theoretical magnetic susceptibility exhibits large Curie term.

The VBG state is similar to the Bose glass (BG) state, which emerges in an interacting boson system with random potential [138, 139] and/or in a disordered dimerized quantum magnet in a magnetic field [140–143]. In the BG state, bosons are localized owing to random potential. However, the compressibility, which corresponds to magnetic susceptibility in magnetic system, is finite, because the depth of random potential distributes from zero.

It is noted that the temperature dependence of the magnetic susceptibility of $(Rb_{1-x}Cs_x)_2Cu_3SnF_{12}$ for $0 < x \leq 0.47$ is similar to that of the $S = 1/2$ kagome-lattice antiferromagnet herbertsmithite, $ZnCu_3(OH)_6Cl_2$, extracted from the Knight shift of NMR spectra shown in Fig. 1.12(b) [95, 97]. This will give insight into the ground state of herbertsmithite. In an actual sample of herbertsmithite, Cu^{2+} partially substitutes for 10% of Zn^{2+} [78]. Cu^{2+} in an octahedral environment is Jahn-Teller active. Consequently, the substituted Cu^{2+} pushes and pulls the

surrounding oxygen ions, which leads to disorder in the oxygen position. Because the oxygen mediates the superexchange interaction in the kagome layer and the superexchange interaction is sensitive to the bond angle of $Cu^{2+} - O^{2-} - Cu^{2+}$ as observed in $Rb_2Cu_3SnF_{12}$, the exchange interaction in the kagome layer is considered to be nonuniform, as in $(Rb_{1-x}Cs_x)_2Cu_3SnF_{12}$. For this reason, the ground state of the actual sample of herbertsmithite is a "spin-liquid-like", which is similar to the disordered state observed in $(Rb_{1-x}Cs_x)_2Cu_3SnF_{12}$.

Chapter 4

Magnetic Properties of $Cs_2LiMn_3F_{12}$

Mn^{3+} ions with $S = 2$ of $Cs_2LiMn_3F_{12}$ forms a uniform kagome lattice. To elucidate KLAF with classical spins, magnetic and thermodynamic measurements of $Cs_2LiMn_3F_{12}$ were conducted, using single crystal. It was found that $Cs_2LiMn_3F_{12}$ undergoes magnetic order at $T_N \simeq 2$ K. I also conducted neutron powder diffraction using high quality sample, and found that the spin structure in the ordered phase is characterized by a propagation vector $\boldsymbol{q} = (1/3, 0, 0)$.

4.1 Magnetic and Thermodynamic Properties

Owing to the improvement of sample preparation, I can obtained high quality single crystal of of $Cs_2LiMn_3F_{12}$ with several natural surfaces. To determine the crystallographic c-axis, I performed X-ray diffraction. Figure 4.1 shows an example of the X-ray diffraction pattern. The observed peaks are identified as $(0, 0, 3n)$ reflections, which indicates the plane to be the c-plane. After confirming the c-plane with X-ray diffraction, I conducted the magnetic and specific heat measurements.

To evaluate g-factor of $Cs_2LiMn_3F_{12}$, I operated electronic spin resonance (ESR) measurements. X-band ESR measurement at 9.44176 GHz has been performed. Figure 4.2 shows ESR spectra observed at room temperature. The ESR spectra for $H \parallel c$ is almost same as that for $H \perp c$. g-values for $H \parallel c$ and $H \perp c$ are obtained as $g_\parallel = 2.01$, and $g_\perp = 2.01$, respectively.

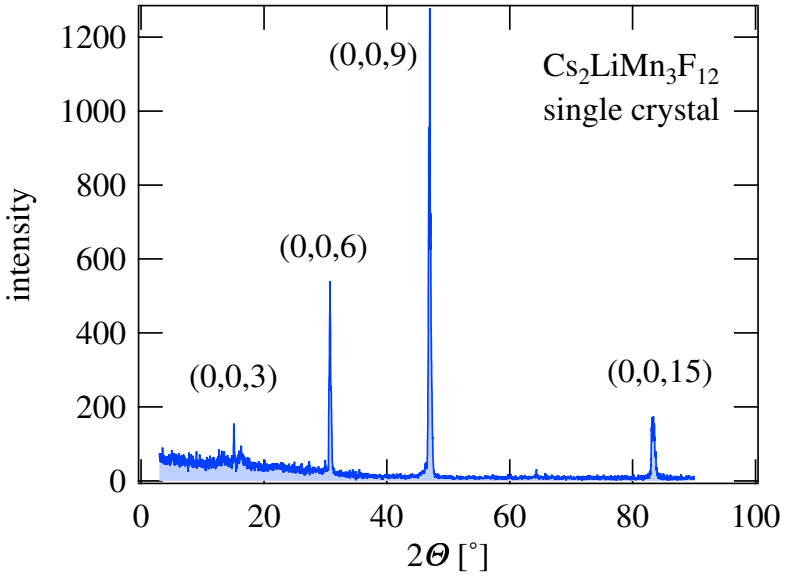

Figure 4.1: X-ray diffraction from the crystallographic c-plane of $Cs_2LiMn_3F_{12}$. Diffraction peaks are identified to be $(0, 0, 3l)$ with $l = 1, 2, 3, \cdots$.

4.1.1 Specific Heat

Figure 4.3 shows the temperature dependence of the specific heat measured for $H \parallel c$. The peak anomaly of the specific heat is observed at 2.1 K in the absence of the magnetic fields, Which is indicative of the magnetic phase transition at $T_N \simeq 2.1$ K. The magnetic ordering at $T_N \simeq 2.1$ K was confirmed by neutron powder diffraction experiment shown next section. The specific heat below 1 K is proportional to T^2 as shown in Fig. 4.4, which indicates that $Cs_2LiMn_3F_{12}$ is magnetically two-dimensional.

With increasing the external magnetic field, T_N increases and the anomaly at T_N is smeared above 3 T, and the temperature dependence of specific heat changes power law behavior (T^2) to exponential behavior ($\exp(-\Delta/k_BT)$) as shown in Fig. 4.4. This result suggests that an excitation gap opens when an external magnetic field is applied parallel to the c-axis. This magnetic-field-induced gap was observed in several $S = 1/2$ one-dimensional antiferromagnet with the staggered $\boldsymbol{g}$

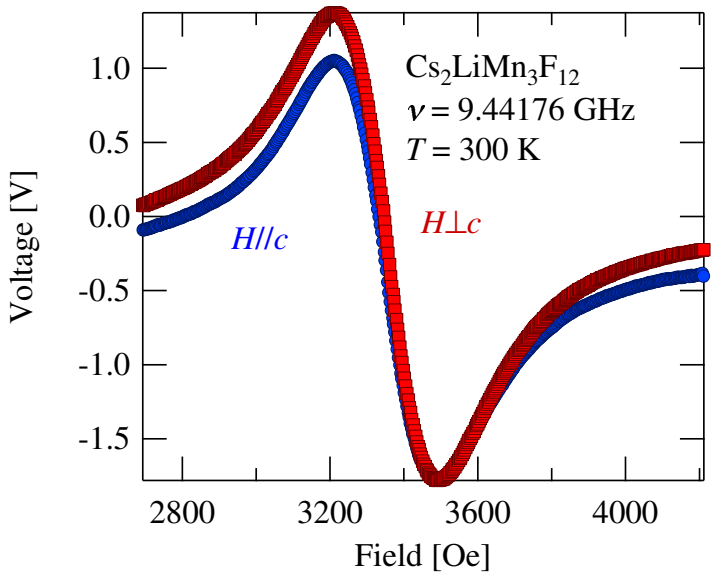

Figure 4.2: Electronic spin resonance spectra observed at room temperature using X band microwave with frequency $\nu = 9.44176$ GHz. The red and blue symbols indicate the ESR spectra for $H \parallel c$ and $H \perp c$, respectively.

tensor g_s and the DM interaction with the staggered $\boldsymbol{D}$ vector $\boldsymbol{D}_s$ [145,146]. In these systems, a staggered magnetic field is induced perpendicular to the external magnetic field $\boldsymbol{H}$ owing to g_s and $\boldsymbol{D}_s$. The staggered magnetic field acts as an effective anisotropy perpendicular to $\boldsymbol{H}$, which produces a finite gap in magnetic excitation. The magnetic-field-induced gap also gives rise to the smearing the magnetic phase transition. Thus, I infer that in $Cs_2LiMn_3F_{12}$, the staggered magnetic field that is conjugate to the ordered spin structure is induced in the external magnetic field.

4.1.2 Magnetic Susceptibility and Magnetization

The temperature dependence of the magnetic susceptibility is shown in Fig. 4.5. Using the Curie-Weiss fit, the Weiss temperatures Θ for $H \parallel c$ and $H \perp c$ are obtained as $\Theta = 40$ K and 32 K, respectively. To analyze the susceptibility data, I used the high temperature expansion of Ref. [147, 148]. I confirmed that the result obtained is the same as that obtained by Rosner *et. al.* for the $J_1 - J_2$ square lattice [149]

and that obtained by Bernu *et. al.* for the kagome lattice $J_1 - J_2 - J_d$−Heisenberg model. [150] The analysis reproduce well the experimental data. When I set the g-value as $g = 2.01$ obtained by the ESR spectra, the exchange constant is estimated as $J/k_{\rm B} = 4.4$ K, which is consistent with that obtained from Curie Weiss fitting. Solid line in Fig. 4.5(b) is a fit of calculated result to the experimental susceptibility with these parameter.

Figure 4.6 shows low-temperature magnetic susceptibilities measured for $H \parallel c$ and $H \perp c$. A bend anomaly is observed at $T_{\rm N} \simeq 2.1$ K for $H \parallel c$, which is attributed to the magnetic phase transition, because the temperature giving the anomaly coincides with $T_{\rm N}$ observed in specific heat measurement. Below 2 K, the magnetic susceptibility is independent of the temperature, which indicates that $Cs_2LiMn_3F_{12}$ exhibits the easy plane type order. For applied magnetic fields higher than 1 T, the susceptibility anomaly is smeared.

To elucidate the field dependence of the anomaly, I measured the magnetization as a function of magnetic field. The result is shown in Fig. 4.7. The observed weak moment is $M_{\rm wf} = 0.17\,\mu_{\rm B}$. Two peaks in the field derivative of magnetization dM/dH are observed at 1.2 T and 2.4 T, which is indicative of the spin flop transitions. I suspect that these transitions are related to the change in the umbrella spin structures between neighboring kagome layers due to the in-plane components of the $\boldsymbol{D}$ vector for the DM interaction, as reported for $KFe_3(OH)_6(SO)_4$ [84]. On the basis of the magnetic susceptibility and magnetization measurements for $H \parallel c$, I can assume that $tCs_2LiMn_3F_{12}$ has weak anisotropy of easy plane type and spins lie in the c-plane making triangular structure. Using a relation $J' = -M_{\rm wf}H/S^2$, I obtain the interlayer exchange constant $J_\perp$ of 0.08 K. The ratio of interlayer and intralayer exchange constants is estimated as $J'/J \simeq 0.02$, which attests $Cs_2LiMn_3F_{12}$ has good two dimensionality.

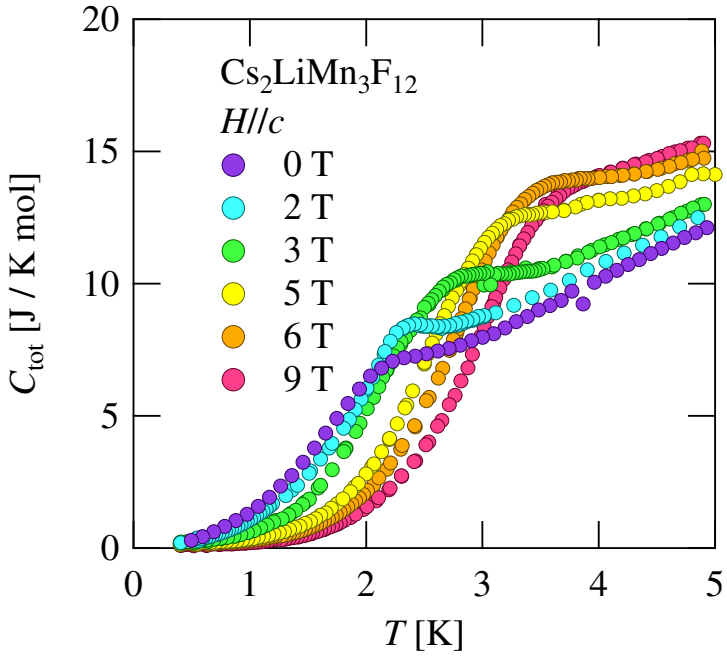

Figure 4.3: Low-temperature total specific heat of $Cs_2LiMn_3F_{12}$ measured at various magnetic fields for $H \parallel c$.

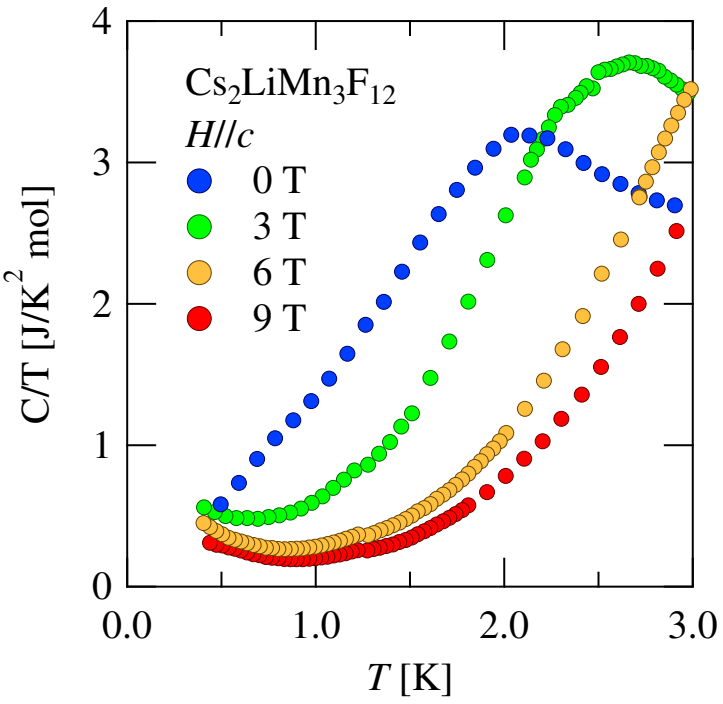

Figure 4.4: Low-temperature total specific heat of $Cs_2LiMn_3F_{12}$ divided by temperature (C/T) vs temperature measured at various magnetic fields for $H \parallel c$.

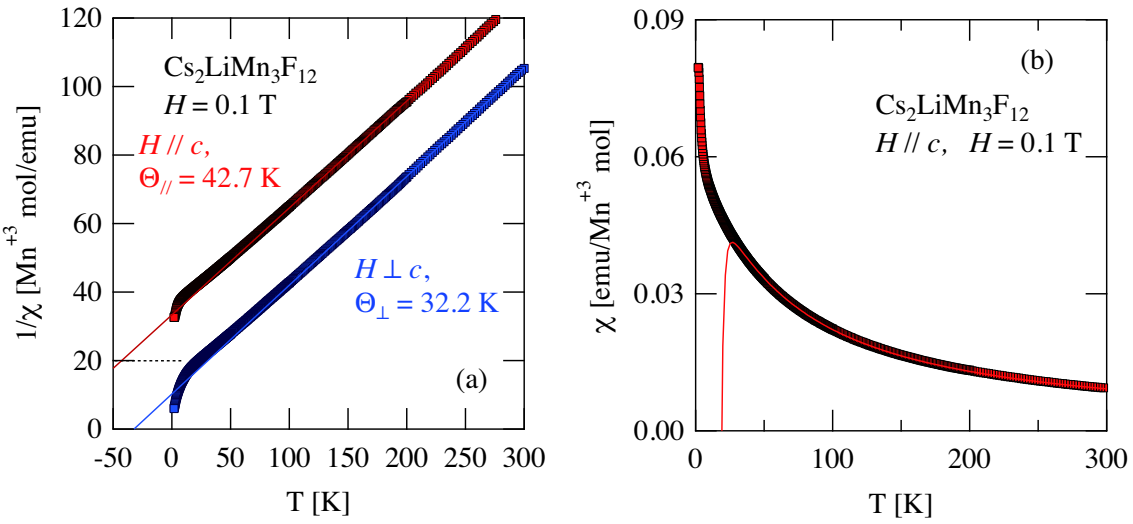

Figure 4.5: (a) Temperature dependence of inverse magnetic susceptibility of $Cs_2LiMn_3F_{12}$ for $H \parallel c$ and $H \perp c$. (b) A fit of calculated result using the high temperature expansion to the experimental susceptibility with $g = 2.01$ and $J/k_B = 4.4$ K.

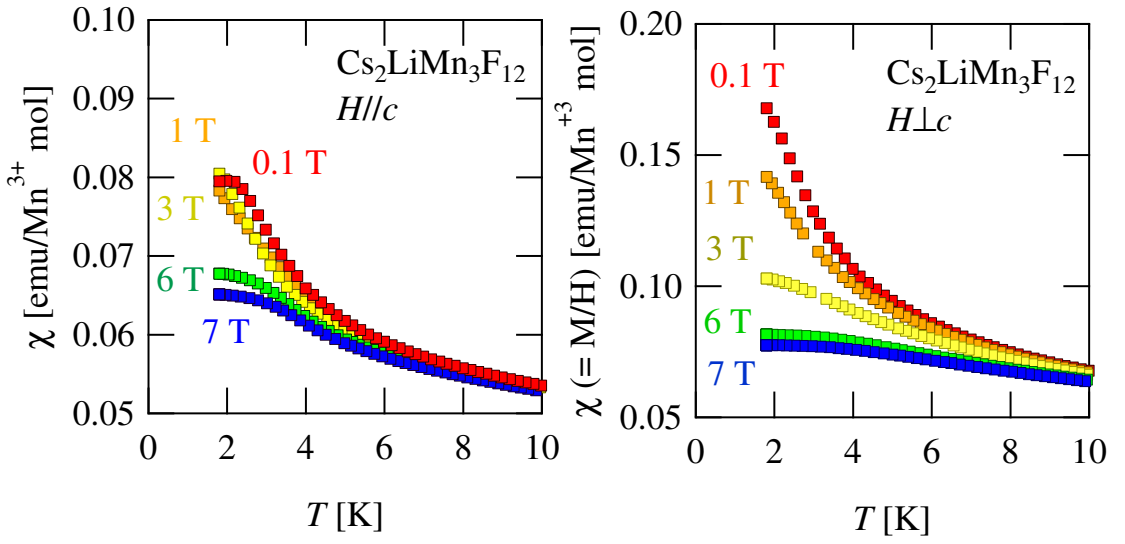

Figure 4.6: Low-temperature magnetic susceptibility of $Cs_2LiMn_3F_{12}$ measured at various fields (a) for $H \parallel c$, and (b) for $H \perp c$.

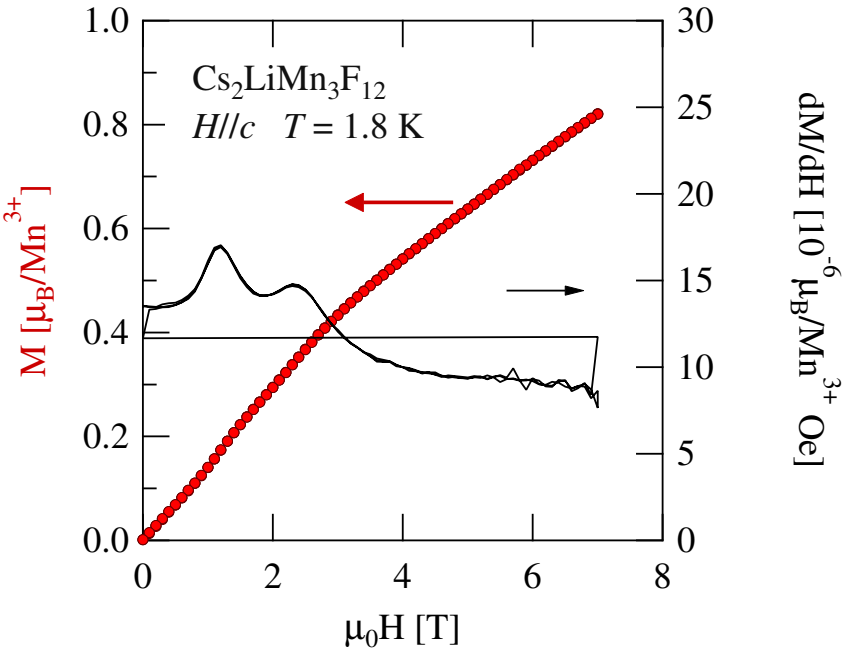

Figure 4.7: Magnetization curve and $\mathrm{d}M/\mathrm{d}H$ versus applied field of $Cs_2LiMn_3F_{12}$ measured at $T = 1.8$ K for $H \parallel c$.

4.2 Neutron Diffraction

In order to investigate the magnetic structure in the ordered phase in $Cs_2LiMn_3F_{12}$, I performed neutron powder diffraction with purified sample, in which the impurity phase is much smaller than the previous sample [118],using high-resolution powder diffractometer ECHIDNA installed at OPAL in ANSTO. The wavelength of the incident neutron was set at $\lambda = 2.43950\,\text{Å}$. The temperature of the sample was lowered down to 1.5 K.

Figure 4.8 shows neutron diffraction patterns of $Cs_2LiMn_3F_{12}$ measured at 1.5 and 4 K. Diffraction peaks observed at 4 K can be assigned by nuclear Bragg peaks with the atomic coordinates shown in Table 1.4. Additional weak peaks are observed at 1.5 K. From the specific heat and magnetic susceptibility measurements shown in the previous section, it was found that $Cs_2LiMn_3F_{12}$ exhibits the magnetic order in at 2 K. Thus, magnetic diffraction can be obtained by subtracting diffraction intensity measured at 4.0 K from that measured below $T_N \simeq 2.0$ K.

Figure 4.9 shows the intensity difference $I(1.5\,\text{K}) - I(4.0\,\text{K})$ as a function of diffraction angle 2θ. In Fig. 4.9, I also show the data of $I(1.5\,\text{K}) - I(4.0\,\text{K})$ collected in 2011 [118]. In the previous experiment in 2011 [118], magnetic diffractions were observed below $T_N \simeq 2.0$ K. However, it was difficult to judge whether observed magnetic peaks are intrinsic, because the sample used contains considerable amount of impurities as $CsMnF_4$ and Li_2MnF_5, which exhibit magnetic orderings at 18 and 11 K, respectively.

Two diffraction data obtained in the present experiment and in 2011 are consistent with each other. This confirms that diffraction peaks are intrinsic to $Cs_2LiMn_3F_{12}$. I can see several magnetic reflections, which occur below $T_N \simeq 2.0$ K. This result indicates that $Cs_2LiMn_3F_{12}$ undergoes magnetic ordering at $T_N \simeq 2.0$ K. The magnetic structure of the ground state reported to date is limited to the $q = 0$ structure [80, 81, 104]. The $\sqrt{3} \times \sqrt{3}$ structure is also known as a candidate of the ground state, which is stabilized by the quantum fluctuation (see Fig. 1.4) [30–33]. However, observed magnetic reflections can be explained in terms of neither $q = 0$ structure nor $\sqrt{3} \times \sqrt{3}$ structure. The best description of the magnetic structure is given by a propagation vector $\boldsymbol{q} = (1/3, 0, 0)$. Arrows in Fig. 4.9 indicate diffraction angles corresponding to $\boldsymbol{Q} = \boldsymbol{G} \pm \boldsymbol{q}$ with the reciprocal wave vector $\boldsymbol{G}$. At present, I

have not succeeded in solving the spin structure that produces the observed diffraction pattern.

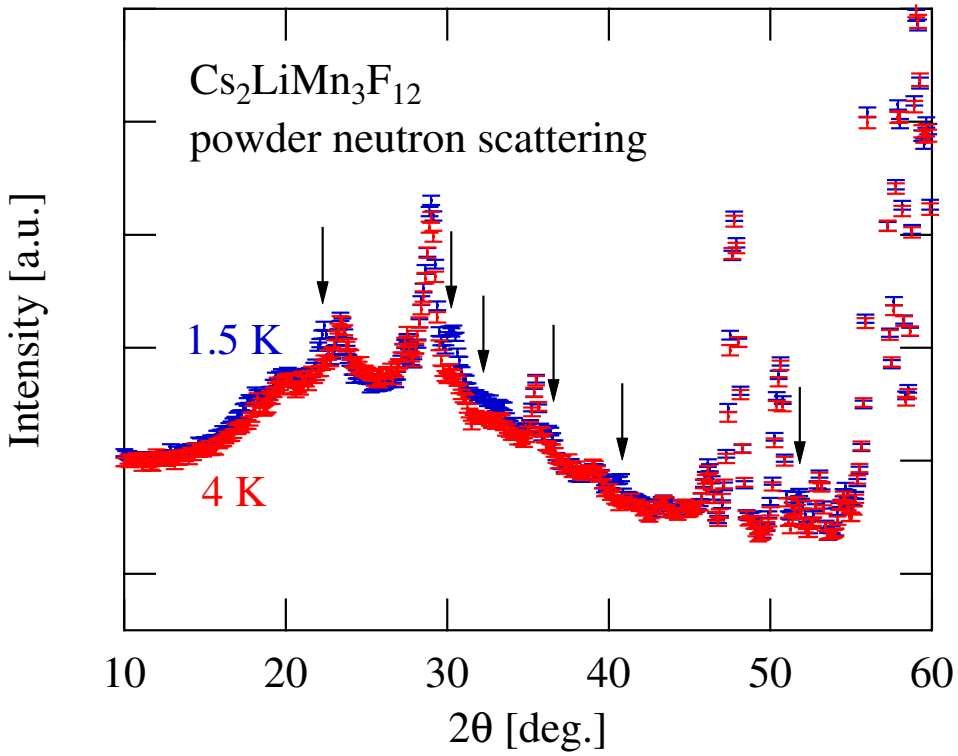

Figure 4.8: Neutron diffraction intensities of $Cs_2LiMn_3F_{12}$ measured at 1.5 K and 4 K. Small magnetic peaks indicated by arrows are observed.

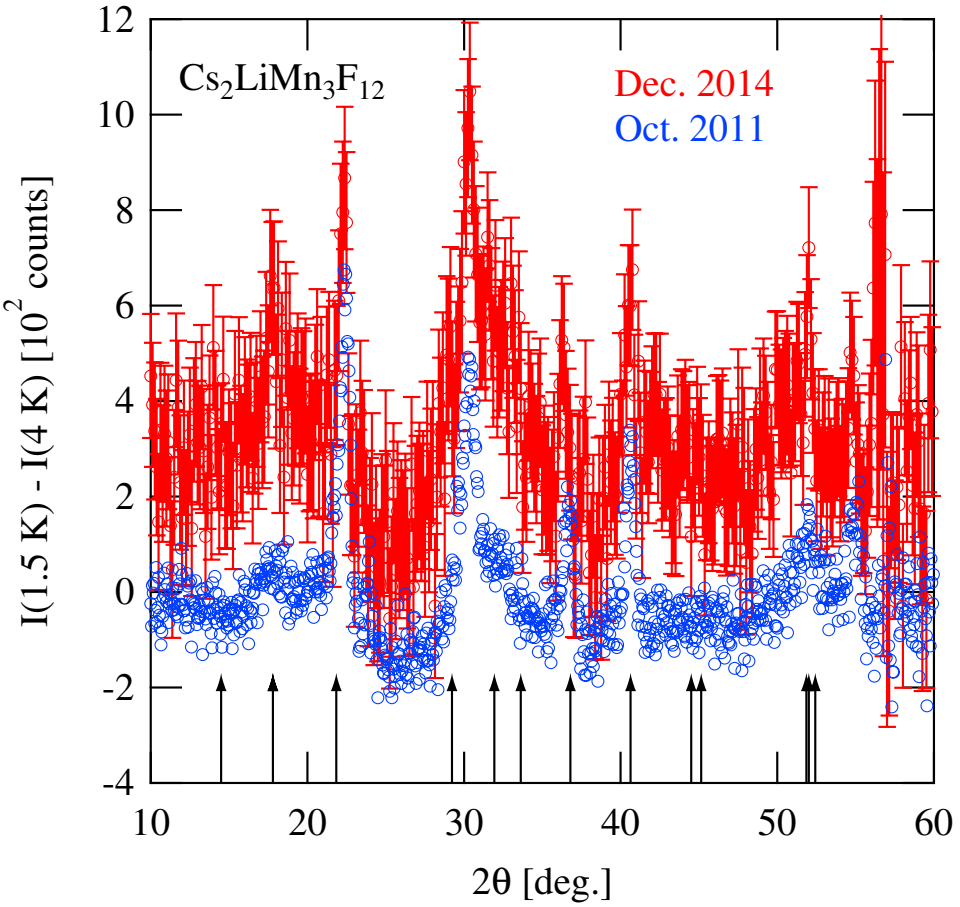

Figure 4.9: Diffraction intensity $I(1.5\,\mathrm{K}) - I(4.0\,\mathrm{K})$ vs diffraction angle 2θ. Blue and red symbols are diffraction data collected in the previous and present experiments, respectively. Data obtained in the present experiment are shifted upward by 200 counts. Arrows indicate diffraction angles corresponding to $\boldsymbol{Q} = \boldsymbol{G} \pm \boldsymbol{q}$ with $\boldsymbol{q} = (1/3, 0, 0)$.

Chapter 5

Conclusion and Outlook

Theoretical consensus on $S = 1/2$ Heisenberg kagome lattice antiferromagnet (KLAF) is that the ground state is disorder owing to the interplay of strong frustration and quantum fluctuation. However, the nature of the disordered ground state has been under debate. Recent theory on quantum KLAFs with bond randomness predicts that when the randomness exceeds a critical value, the ground state changes from the disordered state to a gapless spin-liquid-like state. Motivated by these theoretical debate and predictions, I investigate the magnetic properties of $(Rb_{1-x}Cs_x)_2Cu_3SnF_{12}$, which is a mixture of two $S = 1/2$ KLAFs: $Rb_2Cu_3SnF_{12}$ with gapped ground state and $Cs_2Cu_3SnF_{12}$ with ordered ground state.

The most important point to obtain reliable experimental results is to prepare high-quality single crystals. I first grow single crystals of two parent systems $Rb_2Cu_3SnF_{12}$ and $Cs_2Cu_3SnF_{12}$ from a melting method, using platinum tubes as crucibles. Mixing stoichiometric amount of these parent crystals, I prepare sizable single crystals of $(Rb_{1-x}Cs_x)_2Cu_3SnF_{12}$ with various cesium concentration x from the melting method. Details of the sample preparation is described in section 2.2. The homogeneity of crystals was confirmed by X-ray diffraction.

Using single crystals obtained, I have performed magnetization, thermodynamic and μSR measurements. The magnetic susceptibilities for $(Rb_{1-x}Cs_x)_2Cu_3SnF_{12}$ shows systematic change with x, i.e., the magnetic susceptibility is not given by the superposition of those for $Rb_2Cu_3SnF_{12}$ and $Cs_2Cu_3SnF_{12}$, which confirms the homogeneity of crystals. From high-temperature magnetic susceptibility data for $T \geq 60$ K, I evaluated the four kinds of exchange interaction J_i $(i = 1 - 4)$, using

the exact diagonalization for the 12-kagome cluster. It was found that all the exchange interactions approach a uniform value for $x \rightarrow 1$, as shown in subsection 3.1.1. The substitution between rubidium and cesium ions will also create exchange randomness. Therefore, it is considered that the magnitude of exchange randomness increases with decreasing x from $x = 0$.

From the low-temperature magnetic susceptibility measurements, I observed that with increasing cesium concentration x, $(Rb_{1-x}Cs_x)_2Cu_3SnF_{12}$ undergoes the quantum phase transition from the disordered state to the ordered state at $x_c = 0.53$. I also found that the ground state for $0 < x \leq 0.53$ has a finite magnetic susceptibility, nevertheless the ground state exhibits no long-range magnetic ordering. For $0 < x \leq 0.53$, the excitation gap decreases with increasing x, and vanishes at the critical point $x_c = 0.53$. The absence of the magnetic ordering was confirmed via the μSR measurements conducted down to 0.3 K on the sample with critical concentration $x_c = 0.53$. Thus, the ground state for $0 < x \leq 0.53$ is just like a spin liquid. I discussed this ground state nature according to recent theory that investigate the ground state for $S = 1/2$ Heisenberg KLAF with exchange randomness. The theory predicts that with increasing the magnitude of randomness, the ground state changes from quantum disordered state to a gapless spin-liquid-like state, which is described as valence-bond-glass (VBG). The VBG state is a state in which tightly bound spin singlets are localized on stronger bonds, while loosely bound singlets are situated on weaker bonds, as shown in Fig. 1.9. The characteristic properties associated to the VBG are as follows: (1) magnetic excitation is gapless, (2) long-range magnetic ordering is absent, and (3) low-temperature specific heat is in proportion to temperature. The first two theoretical results are consistent with our experimental results for the ground state for $0 < x \leq 0.53$, though I failed to observe the $T-$ linear specific heat at low temperature, because the exchange interaction is rather large. Therefore, I concluded that the ground state in $(Rb_{1-x}Cs_x)_2Cu_3SnF_{12}$ with $0 < x \leq 0.53$ is the VBG state. This is the first clear report on the ground state of VBG with random kagome lattice.

Experimental magnetic susceptibility for $0 < x \leq 0.53$ shown in Fig. 3.5 displays small Curie term, though theoretical magnetic susceptibility for $S = 1/2$ random bond Heisenberg KLAF exhibits fairly large Curie term in the gapless spin-liquid-like state. I consider that this discrepancy arises from the finite size effect in calculation.

The theoretical magnetic susceptibility was calculated, using exact diagonalization for up to 30-site clusters. Therefore, unpaired spins created on the boundary cannot form spin singlet, which leads to the Curie term in magnetic susceptibility. These unpaired spins will form any singlet when the system size is increased, so that the Curie term decreases.

In VBG, it has been proposed that the ω dependence of the dynamic structure factor $S(\boldsymbol{q}, \omega)$ at Γ point is fairly flat [57, 58]. Dynamic structure factor can be observed through inelastic neutron scattering (INS) experiments. Thus, INS experiments are necessary to elucidate the nature of the disordered ground state in $(Rb_{1-x}Cs_x)_2Cu_3SnF_{12}$. The INS results in our system will give insight into the ground state of herbertsmithite, which is well-known as an $S = 1/2$ Heisenberg KLAF, because the spin-liquid-like ground state observed in herbertsmithite is considered to be ascribed to the exchange randomness.

For $Cs_2LiMn_3F_{12}$, which is described as $S = 2$ KLAF, I have investigated the magnetic properties via the magnetic susceptibility, specific heat and neutron scattering. I succeeded in synthesizing purified and sizable single crystals of $Cs_2LiMn_3F_{12}$. I confirmed the crystallographic axis using x-ray diffractometer for the first time. I measured the magnetic measurements and specific heat for $H \parallel c$ and $H \perp c$ using single crystal sample. It was found that $Cs_2LiMn_3F_{12}$ exhibits the antiferromagnetic order at $T_N \simeq 2.1$ K in both susceptibility and heat capacity measurements. I analyzed the results of magnetic susceptibilities using the high temperature expansion to evaluate the exchange interaction of $J/k_B = 4.4$ K. It was observed that the low-temperature specific heat is proportional to T^2, which indicates that $Cs_2LiMn_3F_{12}$ has a good two-dimensional character. In addition, I observed that the excitation gap is induced by the applied magnetic field, which should be attributed to the alternating $\boldsymbol{D}$ vector of the DM interaction. I conducted the powder neutron diffraction to unveil a magnetic ground state. Several magnetic reflections were observed below $T_N \simeq 2.0$ K. However, observed magnetic reflections can be explained in terms of neither $q = 0$ structure nor $\sqrt{3} \times \sqrt{3}$ structure. It was found that the best description of the magnetic structure is given by a propagation vector $\boldsymbol{q} = (1/3, 0, 0)$. To the best of my knowledge, such an unusual magnetic ordering is the first observation in KLAFs. At present, I have no reasonable solution of the spin structure that produces the observed diffraction pattern. To solve the spin structure of the

ordered state in $Cs_2LiMn_3F_{12}$ is an important future problem. Because there is no theory on the magnetic excitations for classical and quantum KLAFs with a magnetic order characterized by a propagation vector $\boldsymbol{q} = (1/3, 0, 0)$, INS experiments on $Cs_2LiMn_3F_{12}$ are of great interest.

Acknowledgement

Over the years, the author has benefited from discussions and hospitality with Professor Hidekazu Tanaka of Tokyo Institute of Technology who has introduced the quantum spin physics to me. The author has profited greatly in doing this work from stimulating discussions and heartwarming assistance with colleagues in Tanaka-laboratory, particularly Dr. Nobuyuki Kurita, Dr. Toshio Ono, and Mr. Satoshi Hirata.

The author expresses my deepest appreciation to associate professor Takao Suzuki of Shibaura Institute of Technology, and Dr. Isao Watanabe of RIKEN for providing me with the opportunity to conduct the μSR measurements. The author expresses my profound gratitude to Dr. Maxim Avdeev, Professor Taku J. Sato and associate professor Yusuke Nambu of Tohoku University for their discussion and assistance on elastic neutron measurements at ECHIDNA diffractometer in Australian national nuclear research and development organisation. The author expresses my sincere thanks to Dr. Seiko Ohira-Kawamura, Dr. Kenji Nakajima, Dr. Keitaro Kuwahara, and Dr. Shinichi Ito for assistance on inelastic neutron measurements at J-PARC. The author would thank to Yoko Ohtsuka for assistance with ICP-MS analysis at the Center for Advanced Materials Analysis, Tokyo Institute of Technology.

The author acknowledges the financial support from the Center of Excellence Program by Ministry of Education, Culture, Sports, Science and Technology, Japan through the "Nanoscience and Quantum Physics" Project of Tokyo Institute of Technology.

Finally, the author would like to dedicate this thesis to my lovable parents.

Reference

[1] H. B. Callen, *Thermodynamics and an Introduction to Thermostatistics*, (John Wiley & Sons, 1985)

[2] P. W. Anderson, Phys. Rev. **86**, 694 (1952).

[3] J. Ziman, *Principles of the theory of solids*, (Cambridge, 1965).

[4] T. Oguchi, *Statistical Mechanics on Magnetism*, (Shokabo, 1970, in Japanese).

[5] K. Yoshida, *Theory of Magnetism*, (Springer, 2001).

[6] G. W. Pratt, Jr., Phys. Rev **122**, 489 (1961).

[7] W. Marshall, Proc. Roy. Soc. A **232**, 48 (1955).

[8] E. Lieb and D. Mattis, Phys. Rev **125**, 164 (1962).

[9] A. P. Ramirez, Annu. Rev. Mater. Sci **24**, 453 (1994).

[10] R. Moessner, Can. J. Phy. **79**, 1283 (2001).

[11] A. Harrison, J. Phys.: Condens. Matter **16**, S553 (2004).

[12] J. Chalker, *Introduction to Frustrated Magnetism* in Chap. 1, Edited by C. Lacroix, P. Mendels, and F. Mila (Springer, 2010).

[13] L. Balents, Nature (London) **464**, 199 (2010).

[14] P. W. Anderson, Mat. Res. Bull. **8**, 153 (1973).

[15] T. Jolicœur, and J. C. Le Guillou, Phys. Rev. B **40**, 2727 (1989).

[16] A. Chubukov and T. Jolicœur, Phys. Rev. B **46**, 11137 (1992).

[17] S. J. Miyake, J. Phys. Soc. Jpn. **61**, 983 (1992).

[18] S. R. White and A. L. Chernyshev, Phys. Rev. Lett. **99**, 127004 (2007).

[19] I. Syôzi, Prog. Theo. Phys, **6**, 306 (1951).

[20] M. Mekata, Phys. Today **56**, 12 (2003).

[21] P. A. Lee, Science, **321**, 1306 (2008).

[22] K. R. Poeppelmeier and M. Azuma, Nat. Chem. **3**, 758 (2011).

[23] G. André, R. Bidaux, J. -P. Carton ,and R. Conte, and L. de Seze, J. Phys. France **40**, 479 (1979).

[24] J. Villain, R. Bidaux, J. P. Carton, and R. J. Conte, J. Phys. Paris **41**, 1263 (1980).

[25] A. V. Chubukov and D. I. Golosov, J. Phys.: Condens. Matter **3**, 69 (1991).

[26] C. Lhullier, arXiv: cond-mat/0502464.

[27] G. Misguich and C. Lhullier, arXiv: cond-mat/0310405.

[28] M. Takigawa and F. Mila, *Introduction to Frustrated Magnetism* in Chap. 10, Edited by C. Lacroix, P. Mendels, and F. Mila (Springer, 2010).

[29] D. A. Huse and A. D. Rutenberg, Phys. Rev. B **45**, 7536 (1992).

[30] J. T. Chalker, P. C. W. Holdsworth, and E. F. Shender, Phys. Rev. Lett. **68**, 855 (1992).

[31] A. Chubukov, Phys. Rev. Lett. **69**, 832 (1992).

[32] S. Sachdev, Phys. Rev. B **45**, 12377 (1992).

[33] J. N. Reimers and A. J. Berlinsky, Phys. Rev. B **48**, 9539 (1993).

[34] A. B. Harris, C. Kallin, and A. J. Berlinsky, Phys. Rev. B **45**, 2899 (1992).

[35] T. Yildirim and A. B. Harris, Phys. Rev. B **73**, 214446 (2006).

[36] M. J. Lawler, L. Fritz, Y. B. Kim, and S. Sachdev, Phys. Rev. Lett. **100**, 187201 (2008).

[37] R. R. P. Singh and D. A. Huse, Phys. Rev. B **77**, 144415 (2008).

[38] E. S. Sørensen, M. J. Lawler, and Y. B. Kim, Phys. Rev. B **79**, 174403 (2009).

[39] G. Evenbly and G. Vidal, Phys. Rev. Lett. **104**, 187203 (2010).

[40] K. Hwang, Y. B. Kim, J. Yu, and K. Park: Phys. Rev. B **84**, 205133 (2011).

[41] M. B. Hastings, Phys. Rev. B **63**, 014413 (2000).

[42] F. Wang and A. Vishwanath, Phys. Rev. B **74**, 174423 (2006).

[43] M. Hermele, Y. Ran, P. A. Lee, and X.-G. Wen, Phys. Rev. B **77**, 224413 (2008).

[44] Ch. Waldtmann, H. U. Everts, B. Bernu, C. Lhuillier, P. Sindzingre, P. Lecheminant, and L. Pierre, Eur. Phys. J. B **2**, 501 (1998).

[45] S. Yan, D. A. Huse, and S. R. White, Science **332**, 1173 (2011).

[46] I. Dzyaloshinskii, J. Phys. Chem. Solids **4**, 241 (1958).

[47] T. Moriya, Phys. Rev. **120** 91 (1960).

[48] M. Elhajal, B. Canals, and C. Lacroix, Phys. Rev. B **66**, 014422 (2002).

[49] M. Rigol and R. R. P. Singh, Phys Rev. Lett. **98**, 207204 (2007).

[50] O. Cépas, C. M. Fong, P. W. Leung, and C. Lhuillier, Phys. Rev. B **78**, 140405(R) (2008).

[51] H. Nakano and T. Sakai, J. Phys. Soc. Jpn. **80**, 053704 (2011).

[52] S. Depenbrock, I. P. McCulloch, and U. Schollwöck, Phys. Rev. Lett. **109**, 067201 (2012).

[53] S. Nishimoto, N. Shibata, and C. Hotta, Nat. Commun. **4**, 2287 (2013).

[54] T. Picot, M. Ziegler, R. Orús, and D Poilblanc, arXiv cond-mat/1508.07189.

[55] R. R. P. Singh, Phys. Rev. Lett. **104**, 177203 (2010).

[56] K. Watanabe, H. Kawamura, H. Nakano, and T. Sakai, J. Phys. Soc. Jpn. **83**, 034714 (2014).

[57] H. Kawamura, K. Watanabe, and T. Shimokawa, J. Phys. Soc. Jpn. **83**, 103704 (2014).

[58] T. Shimokawa, K. Watanabe, and H. Kawamura, Phys. Rev. B **92**, 134407 (2015).

[59] R. N. Bhatt and P. A. Lee, Phys Rev. Lett. **48**, 344 (1982).

[60] D. S. Fisher, Phys. Rev. B **50**, 3799 (1994).

[61] M. Tovar, K. S. Raman, and K. Shtengel, Phys. Rev. B **79**, 024405 (2009).

[62] A. V. Chubukov and D. I. Golosov, J. Phys. Cond. matter **3**, 69 (1991).

[63] D. J. J. Farnell, R. Zinke, J. Schulenburg, and J. Richter, J. Phys.: Condens. Matter **21**, 406002 (2009).

[64] T. Sakai and H. Nakano, Phys. Rev. B **83**, 100405 (2011).

[65] C. Hotta, S. Nishimoto, and N. Shibata, Phys. Rev. B **87**, 115128 (2013).

[66] K. Hida, J. Phys. Soc. Jpn. **70** 3673 (2001).

[67] J. Schulenburg, A. Honecker, J. Schnack, J. Richter, and H. J. Schmidt, Phys. Rev. Lett. **88**, 167207 (2002).

[68] H. Nakano and T. Sakai, J. Phys. Soc. Jpn. **79** 053707 (2010).

[69] S. Capponi, O. Derzhko, A. Honecker, A. M. Läuchli, and J. Richter, Phys. Rev. B **88**, 144416 (2013).

[70] M. Tarzia and G. Biroli, Europhys. Lett. **82**, 67008 (2008).

[71] T. Ono, H. Tanaka, T. Nakagomi, O. Kolomiyets, H. Mitamura, F. Ishikawa, T. Goto, K. Nakajima, A. Oosawa, Y. Koike, K. Kakurai, J. Klenke, P. Smeibidle, M. Meisner, and H. A. Katori, J. Phys. Soc. Jpn. **74** (Suppl.), 135 (2005).

[72] H. Tominaga, T. Ono, K. Iwase, H. Yamaguchi, H. Ishibashi, N. Kurita, H. Tanaka, H. Nakano, H. Nojiri, and Y. Hosokoshi, presented at JPS 69th Annual Meeting, March 30, 2014, Tokai University, Shonan Campus.

[73] B. M. Bartlett and D. G. Nocera, J. Am. Chem. Soc. **127**, 8985 (2005).

[74] Z. Hiroi, M. Hanawa, N. Kobayashi, M. Nohara, H. Takagi, Y. Kato, and M. Takigawa, J. Phys. Soc. Jpn. **70**, 3377 (2001).

[75] M. P. Shores, E. A. Nytko, B. M. Bartlett, and D. G. Nocera, J. Am. Chem. Soc. **127**, 13462 (2005).

[76] H. Yoshida, J. Yamaura, M. Isobe, Y. Okamoto, G. J. Nilsen and Z. Hiroi, Nat. Commun. **3**, 860 (2012).

[77] O. Janson, J. Richter, P. Sindzingre, and H. Rosner, Phys. Rev. B **82**, 104434 (2010).

[78] F. Bert, S. Nakamae, F. Ladieu, D. L'Hôte, P. Bonville, F. Duc, J.-C. Trombe, and P. Mendels, Phys. Rev. B **76**, 132411 (2007).

[79] S. A. Reisinger, C. C. Tang, S. P. Thompson, F. D. Morrison, and P. Lightfoot, Chem. Mater. **23**, 4234 (2011).

[80] T. Inami, M. Nishiyama, S. Maegawa, and Y. Oka, Phys. Rev. B **61**, 12181 (2000).

[81] D. Grohol, D. G. Nocera, and D. Papoutsakis, Phys. Rev. B **67**, 064401(2003).

[82] K. Matan, D. Grohol, D. G. Nocera, T. Yildirim, A. B. Harris, S. H. Lee, S. E. Nagler, and Y. S. Lee, Phys. Rev. Lett. **96**, 247201 (2006).

[83] D. Grohol, K. Matan, J.-H. Cho, S.-H. Lee, J. W. Lynn, D. G. Nocera, and Y. S. Lee, Nat. Mater. **4**, 323 (2005).

[84] T. Fujita, H. Yamaguchi, S. Kimura, T. Kashiwagi, M. Hagiwara, K. Matan, D. Grohol, D.C. Nocera, and Y. S. Lee, Phys. Rev B **85**, 094409 (2012).

[85] F. Bert, D. Bono, P. Mendels, F. Ladieu, F. Duc, J.-C. Trombe, and P. Millet, Phys. Rev. Lett. **95**, 087203 (2005)

[86] S. Yamashita, T. Moriura, Y. Nakazawa, H. Yoshida, Y. Okamoto, and Z. Hiroi, J. Phys. Soc. Jpn. **79**, 083710 (2010).

[87] Y. Okamoto, M. Tokunaga, H. Yoshida, A. Matsuo, K. Kindo, and Z. Hiroi, Phys. Rev. B **83**, 180407(R) (2011).

[88] H. Ishikawa, M. Yoshida, K. Nawa, M. Jeong, S. Krämer, M. Horvatić, C. Berthier, M. Takigawa, M. Akaki, A. Miyake, M. Tokunaga, K. Kindo, J. Yamaura, Y. Okamoto, and Z. Hiroi, Phys. Rev. Lett. **114**, 227202 (2015).

[89] H. Ishikawa, J. Yamaura, Y. Okamoto, H. Yoshida, G. J. Nilsen, and Z. Hiroi, Acta Crystallogr. Sect. C **68**, i41 (2012).

[90] T. H. Han, J. S. Helton, S. Chu, A. Prodi, D. K. Singh, C. Mazzoli, P. Muller, D. G. Nocera, and Y. S. Lee, Phys. Rev. B **83** 100402(R) (2011).

[91] J. S. Helton, K. Matan, M. P. Shores, E. A. Nytko, B. M. Bartlett, Y. Yoshida, Y. Takano, A. Suslov, Y. Qiu, J. -H. Chung, D. G. Nocera, and Y. S. Lee, Phys. Rev. Lett. **98**, 107204 (2007).

[92] T. H. Han, J. S. Helton, S. Chu, D. G. Nocera, J. A. Rodriguez-Rivera, C. Broholm, and Y. S. Lee, Nature **492**, 406 (2012).

[93] P. Mendels, F. Bert, M. A. de Vries, A. Olariu, A. Harrison, F. Duc, J. C. Trombe, J. S. Lord, A. Amato, and C. Baines, Phys. Rev. Lett. **98**, 077204 (2007).

[94] M. A. de Vries, D. Wulferding, P. Lemmens, J. S. Lord, A. Harrison, P. Bonville, F. Bert, and P. Mendels, Phys. Rev. B **85**, 014422 (2012).

[95] T. Imai, E. A. Nytko, B. M. Bartlett, M. P. Shores, and D. G. Nocera, Phys Rev. Lett. **100**, 077203 (2008).

[96] T. Imai, M. Fu, T. H. Han, and Y. S. Lee, Phys. Rev. B **84**, 020411(R) (2011).

[97] A. Olariu, P. Mendels, F. Bert, F. Duc, J. C. Trombe, M. A. de Vries, and A. Harrison, Phys. Rev. Lett. **100**, 087202 (2008).

[98] M. Fu, T. Imai, T. H. Han, and Y. S. Lee, Science, **350**, 655 (2015).

[99] T. H. Han, M. R. Norman, J. J. Wen, J. A. Rodriguez-Rivera, J. S. Helton, C. Broholm, Y. S. Lee, arXiv:1512.06807.

[100] K. Morita, M. Yano, T. Ono, H. Tanaka, K. Fujii, H. Uekusa, Y. Narumi, and K. Kindo, J. Phys. Soc. Jpn. **77**, 043707 (2008).

[101] T. Ono, K. Morita, M. Yano, H. Tanaka, K. Fujii, H. Uekusa, Y. Narumi, and K. Kindo, Phys. Rev. B **79**, 174407 (2009).

[102] M. Müller and B. G. Müller, Z. Anorg. Allg. Chem. **621**, 993 (1995).

[103] L. J. Downie, C. Black, E. I. Ardashnikova, C. C. Tang, A. N. Vasiliev, A. N. Golovanov, P. S. Berdonosov, V. A. Dolgikh, and P. Lightfoot, CrystEngComm. **16**, 7419 (2014).

[104] T. Ono, K. Matan, Y. Nambu, T. J. Sato, K. Katayama, S. Hirata, and H. Tanaka, J. Phys. Soc. Jpn. **83**, 043701 (2014).

[105] K. Matan, T. Ono, Y. Fukumoto, T. J. Sato, J. Yamaura, M. Yano, K. Morita, and H. Tanaka, Nat. Phys. **6**, 865 (2010).

[106] K. Matan, Y. Nambu, Y. Zhao, T. J. Sato, Y. Fukumoto, T. Ono, H. Tanaka, C. Broholm, A. Podlesnyak, and G. Ehlers, Phys. Rev. B **89**, 024414 (2014).

[107] T. Ono, K. Matan, Y. Nambu, T. J. Sato, and H. Tanaka, Solid State Physics [in Japanese] **49**, 671 (2014).

[108] M. S. Grbić, S. Krämer, C. Berthier, F. Trousselet, O. Cépas, H. Tanaka, and M. Horvatić, Phys. Rev. Lett. **110**, 247203 (2013).

[109] B. J. Yang and Y. B. Kim, Phys. Rev. B **79**, 224417 (2009).

[110] E. Khatami, R. R. P. Singh, and M. Rigol, Phys. Rev. B **84**, 224411 (2011).

[111] J. des Cloizeaux and J. J. Pearson, Phys. Rev. **128**, 2131 (1962).

[112] Y. Endoh, G. Shirane, R. Birgeneau, P. Richards, and S. Holt, Phys. Rev. Lett. **32**, 170 (1974).

[113] J. Igarashi, Phys. Rev. B **46**, 10763 (1992).

[114] R. R. P. Singh, and M. P. Gelfand, Phys. Rev. B **52**, R15695 (1995).

[115] H. M. Rønnow, D. F. McMorrow, R. Coldea, A. Harrison, I. D. Youngson, T. G. Perring, G. Aeppli, O. Syljuåsen, K. Lefmann, and C. Rischel, Phys. Rev. Lett. **87**, 037202 (2001).

[116] U. Englich, C. Frommen, and W. Massa, J. Alloys and Comp. **246**, 155 (1997).

[117] G. Xu, B. Lian, and S.-C. Zhang, Phys. Rev. Lett. **115**, 186802 (2015).

[118] T. Usui, Master thesis, Tokyo Institute of Tech. (2012).

[119] K. Hwang, K. Park, and Y. B. Kim, Phys. Rev. B **86**, 214407 (2012).

[120] Quantum Design, *Magnetic Property Measurement System: MPMS XL Hardware Reference Manual*.

[121] A. Barone and G Paterno, *Physics and Applications of the Josephson Effect* (Wiley and Sons Inc. 1982), Chapter 13.

[122] S. Kobayashi, *Progress of measurements for condensed matter physics Vol. 2 - SQUID, SOR, and electron emission* - Edited by S. Kurihara, J. Sone, and E. Maruyama (Maru-Zen, 1996, in Japanese).

[123] Quantum Design, *Subtracting the Sample Holder Background from Dilute Samples*, MPMS Application Note 1014-213.

[124] R. Bachmann, F. J. DiSalvo, Jr. T. H. Geballe, R. L. Greene, R. E. Howard, C. N. King, H. C. Lee, R. E. Schwall, H.-U. Thomas, and R. B. Zubeck, Rev. Sci. Instrum. **43**, 205 (1972).

[125] J. P. Shepherd, Rev. Sci. Instrum. **56**, 273 (1985).

[126] J. R. Hook and H. E. Hall, *Solid State Physics, 2nd Edition* (Wiley, 1991).

[127] G. L. Squires, *Introduction to the theory of thermal neutron scattering*, (Cambridge).

[128] A. Furrer, J. Mesot, and T. Strässle, *Neutron scattering in condensed matter physics* (World Scientific).

[129] ANSTO, *Echidna Fact Sheet*

[130] P. W. Selwood, *Magnetochemistry* (Wiley-Interscience, New York, 1956) 2nd ed., Chap. 2, p. 78.

[131] K. Katayama, N. Kurita, and H. Tanaka, Phys. Rev. B **91**, 214429 (2015).

[132] N. Elstner and A. P. Young, Phys. Rev. B **50**, 6871 (1994).

[133] G. Misguich and P. Sindzingre, Eur. Phys. J. B **59**, 305 (2007).

[134] S. Sasaki, N. Narita, and I. Yamada, J. Phys. Soc. Jpn. **64**, 2701 (1995).

[135] M. Troyer, H. Tsunetsugu, and D. Würtz, Phys. Rev. B **50**, 13515 (1994).

[136] M. B. Stone, I. Zaliznyak, D. H. Reich, and C. Broholm, Phys. Rev. B **64**, 144405 (2001).

[137] K. Sasao, N. Kunisada, and Y. Fukumoto, unpublished result. K. Sasao, N. Kunisada, and Y. Fukumoto, Meeting Abst. Phys. Soc. Jpn. **65(2-3)**, 442 (2010). (in Japanese)

[138] T. Giamarchi and H. J. Schulz, Phys. Rev. B **37**, 325 (1988).

[139] M. P. A. Fisher, P. B. Weichman, G. Grinstein, and D. S. Fisher, Phys. Rev. B **40**, 546 (1989).

[140] A. Oosawa and H. Tanaka, Phys. Rev. B **65**, 184437 (2002).

[141] Y. Shindo and H. Tanaka, J. Phys. Soc. Jpn. **73**, 2642 (2004).

[142] F. Yamada, H. Tanaka, T. Ono, and H. Nojiri, Phys. Rev. B **83**, 020409(R) (2011).

[143] A. Zheludev and T. Roscilde, C. R. Phys. **14**, 740 (2013).

[144] T. Suzuki, K. Katayama, I. Kawasaki, I. Watanabe, and H. Tanaka, submitted to Phys. Rev. B.

[145] M. Oshikawa and I. Affleck, Phys. Rev. Lett. **79**, 2883 (1997).

[146] I. Umegaki, H. Tanaka, T. Ono, M. Oshikawa, and K Sakai, Phys. Rev. B **85** 144423 (2012)

[147] A. Lohmann, H.-J. Schmidt, and J. Richter, Phys. Rev. B **89**, 014415 (2014).

[148] http://www-e.uni-magdeburg.de/jschulen/HTE10/

[149] H. Rosner, R. R. P. Singh, W. H. Zheng, J. Oitmaa, and W. E. Pickett, Phys. Rev. B **67**, 014416 (2003).

[150] B. Bernu, C. Lhuillier, E. Kermarrec, F. Bert, P. Mendels, R. H. Colman, and A. S. Wills, Phys. Rev. B **87**, 014416 (2003).

Publication List

- T. Yokobori, M. Okawa, K. Konishi, R. Takei, K. Katayama, S. Oozono, T. Shinmura, T. Okuda, H. Wadati, E. Sakai, K. Ono, H. Kumigashira, M. Oshima, T. Sugiyama, E. Ikenaga, N. Hamada, and T. Saitoh:
  Electronic structure of the hole-doped delafossite oxides $CuCr_{1-x}Mg_xO_2$;
  Phys. Rev. B **87**, 195124 (2013).

- T. Ono, K. Matan, Y. Nambu, T. J. Sato, K. Katayama, S. Hirata, and H. Tanaka:
  Large Negative Quantum Renormalization of Excitation Energies in the Spin-1/2 Kagome Lattice Antiferromagnet $Cs_2Cu_3SnF_{12}$;
  J. Phys. Soc. Jpn. **83**, 043701 (2014).

- T. Suzuki, H. Guo, I. Kawasaki, I. Watanabe, T. Goto, K. Katayama, and H. Tanaka:
  Disappearance of Gapped Mott Insulating Phase Neighboring Bose Glass Phase in $Tl_{1-x}K_xCuCl_3$ Detected by Longitudinal-Field Muon Spin Relaxation;
  J. Phys. Soc. Jpn. **83** 084703 (2014).

- K. Katayama, N. Kurita, and H. Tanaka:
  Quantum phase transition between disordered and ordered states in the spin-1/2 kagome lattice antiferromagnet $(Rb_{1-x}Cs_x)_2Cu_3SnF_{12}$;
  Phys. Rev. B **91**, 214429 (2015).

- T Suzuki, K. Katayama, I. Kawasaki, I. Watanabe, and H. Tanaka:

Spin fluctuations in the spin-1/2 kagome lattice antiferromagnet $(Rb_{1-x}Cs_x)_2Cu_3SnF_{12}$ around the quantum critical point detected by muon spin relaxation technique; submitted to Phys. Rev. B.